Modeling and analysis of holographic micrograting for high-density recording

von

Diplom-Physikerin Daniela Grothe

aus Berlin

von der Fakultät II
Mathematik und Naturwissenschaften
der Technischen Universität Berlin

zur Erlangung des akademischen Grades
Doktorin der Naturwissenschaften
– Dr. rer. nat. –
genehmigte Dissertation

Promotionsausschuss:

Vorsitzender:	Prof. Dr. M. Dähne
Gutachter:	Prof. Dr. H.-W. Hübers
Gutachter:	Prof. Dr. P. Koppa, Budapest University of Technology and Economics, Hungary

Tag der wissenschaftlichen Aussprache: 15. Januar 2016

Berlin 2016

ZUSAMMENFASSUNG

Mikroholographie ist ein neuer Ansatz für die optische Datenspeicherung. Hierbei werden Daten in Form von holographischen Mikrogittern im lichtempfindlichen Volumen einer transparenten optischen Disc gespeichert. Die Datenbits in Form von Mikrogittern entstehen durch konfokale Überlagerung eines hin- und rücklaufenden, fokussierten Laserstrahls und werden mit dem gleichen Strahl ausgelesen. Im Rahmen dieser Arbeit wird mit einer effizienten Berechnungsmethode die Beugung von Licht an Mikrogittern in verschiedenen Speichermedien analysiert. Hierbei wird die Beugungseffizienz als Funktion der Position und Wellenlänge des Lesestrahls berechnet.

In dieser Arbeit geht es darum, i) den Einfluss der Sättigung des Speichermaterials auf die Beugungseigenschaften der Mikrogitter in linearen und quadratischen Medien zu ermitteln, und ii) die Auswirkung der begrenzten Materialressourcen auf die Beugungseffizienz bei der Speicherung mehrerer Datenebenen zu berechnen, um die Möglichkeiten für hohe Datendichten in diesen Materialtypen auszuloten.

Es werden zunächst die kleinstmöglichen (auflösungsbegrenzten) Mikrogitter untersucht. Das Auftreten von Sättigungseffekten bei der Holographie in Photopolymeren führt zu ausgedehnten Mikrogittern mit anderen Eigenschaften. Aufgrund der Wirkungsweise der Holographie ist die effektive Größe dieser Gitter, also die räumliche Ausdehnung, innerhalb derer die Gitter ein Beugungssignal liefern, deutlich geringer als ihre wirkliche Ausdehnung. Zum Beispiel haben Gitter mit einer Länge von 10 µm (FWHM) eine effektive Länge von unter 3 µm. Die Beugungseffizienz ist im Bereich 10^{-3} bei einem Brechungsindexkontrast von 0,001.

Die Analyse der spektralen Eigenschaften erlaubt auch einen Einblick in die auftretenden Beugungseffekte. Mit schwacher Sättigung entstehen kleinere Mikrogitter. Diese zeigen bei kleineren Wellenlängen Beugung unter einem seitlichen Austrittswinkel, der durch das breite Winkelspektrum des Lesestrahls und dieser Gitter abgedeckt wird. Bei größeren Gittern aufgrund stärkerer Sättigung lässt dieser Effekt nach; außerdem verringert sich die spektrale Breite auf wenige Prozent der Wellenlänge.

Die Methode für die Berechnung der Belichtungsreihen für gleiche Beugungseffizienzen in mehreren Datenebenen berücksichtigt den Teilüberlapp der einzelnen Ebenen.

Die Resultate bestätigen, dass sich lineare Medien nicht für hinreichend hohe Datendichten mit ausreichender Beugungseffizienz eignen. Hingegen ermöglichen quadratische Medien mit einem Zweiphotonen-Mechanismus prinzipiell hohe Datendichten, da der Materialverbrauch räumlich auf die einzelnen Datenebenen begrenzt ist. Allerdings liegen die Beugungseffizienzen mit 10^{-6} noch unter dem Niveau des Rauschens durch Materialinhomogenitäten. Unter diesen Bedingungen müssten größere Mikrogitter bei kleinerer numerischer Apertur geschrieben werden, um die Beugungseffizienz zu verbessern, wobei jedoch die erforderliche Materialdicke steigt.

ABSTRACT

Microholographic data storage uses the entire photosensitive volume in a transparent disc the size of a DVD. The data bits, microgratings, are recorded using a high-NA focused laser beam which is mirrored into itself. For readout, the mirrored part of this beam is blocked by a shutter. In this work, an efficient calculation method is devised to analyze the diffraction properties of microgratings in different recording media with and without saturation. This is done by calculating the diffraction efficiency (DE) as a function of the position and wavelength of the readout beam.

Two major tasks are addressed in this thesis: i) to analyze the influence of saturation of the recording material on the diffraction properties of microgratings in linear and quadratic recording media, and ii) to evaluate the implications of limited material resources for multilayer microholographic data storage and the prospects of the two material types for high data capacities.

In a linear medium with saturation, the gratings are localized during readout with much smaller dimensions compared to their real size, which is the benefit of holography. Gratings with a depth (FWHM) of 10 µm, for example, have an effective depth (FWHM) below 3 µm, enabled by Bragg diffraction. With a refractive index contrast of 0.001, the DE of these gratings is of the order of 10^{-3}.

The spectral analysis also provides an insight into the diffraction effects which take place. The smallest microgratings show a maximum of the diffraction at a larger radius if the readout wavelength is smaller. The results reveal a shift of the diffraction angle, which is supported by the broad angular spectrum of the high-NA beam and the small grating. For larger gratings due to stronger saturation of the recording material, this effect is weaker. These larger gratings also have a stronger spectral selectivity.

To compute recording schedules for equal diffraction efficiencies in multiple layers, an efficient method is devised which accounts for the partially overlapping gratings due to shift multiplexing. Due to the consumption of material resources by the first few layers, the achievable diffraction efficiencies are very small (10^{-5} to 10^{-6}). The results clearly confirm that linear recording media are not suitable for high-capacity microholographic data storage.

Square-law media with a two-photon recording mechanism enable multilayer data storage by constraining the index change to each layer. However, the microgratings are smaller than in a linear recording medium, which leads to a smaller DE. With an index contrast of 0.001 and moderate saturation, the DE is of the order of 10^{-6}, below the noise level of the recording material. To enhance the DE, the microgratings have to be enlarged by using a smaller NA, which requires an unfavorably large thickness of the recording material.

Contents

ZUSAMMENFASSUNG 2

ABSTRACT 4

1 Introduction 9

2 Optical storage technologies 13

2.1 Conventional optical disc systems 13

2.2 Multilayer and 3D optical data storage 15

2.3 Microholographic data storage 17

3 Volume holography and microgratings 21

3.1 Holographic volume gratings as plane-wave gratings 21

3.2 Localized gratings - microgratings 24

3.3 Methods for modeling the diffraction on holograms 25

4 Modeling the diffraction efficiency of holographic microgratings 29

4.1 The micrograting in a linear recording material 31

4.2 Readout of microgratings 40

4.3 Wavelength selectivity of microgratings 44

4.4 Conclusion 48

5 Effects of saturation on the selectivity of microgratings 49

5.1 Microgratings in saturating photopolymers 50

5.2 Modeling the diffraction efficiency of gratings with saturation 57

5.3 Readout of microgratings in a saturating medium 60

5.4 Wavelength selectivity of microgratings with saturation 65

5.5 Micrograting with depleted contrast near the focus 68
5.6 Conclusion 83

6 Multilayer holographic data storage in saturating photopolymers 85
6.1 Refractive index contrast in multilayer recording 89
6.2 Exposure schedules for multilayer data storage 94
6.3 Multilayer data storage from gratings to full layers 97
6.4 Conclusion 110

7 Square-law media for multilayer microholographic data storage 111
7.1 Micrograting in two-photon recording media 112
7.2 Multilayer data storage in quadratic media 116
7.3 Recommendations for multilayer data storage 118
7.4 Conclusion 120

8 Conclusion 121

9 Outlook 123

BIBLIOGRAPHY 127

ACKNOWLEDGEMENT 137

1 Introduction

Optical storage of information is at least as old as writing. Digital data storage and processing with the help of machines became useful as soon as the population of the US increased. At the time, it would have taken more than ten years to finish the statistics of the 63 million people. The invention of punched cards made of stiff paper and of the tabulating machines by Herman Hollerith vastly accelerated the evaluation of the US census in the year 1890, which was completed within 18 months [1]. The idea of using punched paper by machines was not entirely new, it had earlier been used in Jacquard looms, permitting the industrial production of fabric with arbitrary patterns. With the introduction of computers, punched cards were more and more replaced by magnetic tape [1].

Since then, much has changed. Digital technology has found its way into almost every sphere of our lives. Smartphones are permanently connected to the Internet. Cloud computing and software as a service offer new ways of computing but may entail new targets for cyber attacks. Data-centered economy becomes more and more important. With increasing amounts of data, the demand for high-capacity storage media will continue growing as well.

Astronomical amounts of data are not only produced by space observatory and large ground-based telescopes. Particle physics is another source of abundant data. Every second, 40 TB of experimental data are produced at the Large Hadron Collider at CERN [2]. Another plethora of data is produced by millions of customer transactions every hour in shops and banks, stored in libraries, and social networks are filled with an abundance of photos [3].

Back in the 19th century, the possibility of capturing sound was an innovation. With the invention of gramophone players, recorded music became affordable. Magnetic tapes

such as compact cassettes and VHS cassettes were common prior to the introduction of the CD and DVD. The success of optical data storage started at the beginning of the 1980s [4]. The music industry boosted the market for optical discs. Compact discs (CDs) found prevalence in the 90s and later for large-scale production in various kinds of storage tasks, for example computer software. The successors, DVD and Blu-ray discs (BD), provide the storage capacity for current storage tasks including HD video.

Among all current types of optical data storage volumes, the principle of recording the data is similar. Data is stored in a reflective layer made of thin metal within a disc made of polycarbonate. As larger data capacities were achieved with smaller spots of the laser and thinner protection layers in each new generation of optical discs, the limit of optical resolution is now within reach. In contrast, other storage devices with high capacity such as hard disks and solid state disks (SSD) are designed rather for frequent rewriting and fast access than for applications of frequent exchanging.

A cheap, lightweight, not rewritable disc for dissemination of high-definition video or for archiving applications is always appreciated. The next step in improving the storage capacity of optical discs, multilayer data storage, lead to the double-layer DVD format which provides a capacity of 8,5 GB. However, the production of an optical disc with many reflective layers is not only costly but also limited by physical constraints as transmission always competes with reflection. In principle, reflection is only needed at the point where the data is currently read, which can be achieved by localized reflective bit patterns in a transparent disc.

Microholographic data storage, proposed by Eichler and Orlic in 1998 [5], is a promising technology for optical data storage. It offers an elegant solution which is compatible with the established optical disc technology, allowing for one optical drive which can read all the prevalent types of discs.

The new storage method utilizes the entire volume of a transparent storage disc which consists of a photopolymer sandwiched between two substrates. The data bits are recorded as volumetrically localized reflection gratings, which are stored in multiple layers within the photopolymer [6]. The microholographic disc has the same diameter as a DVD and it is handled much like the common optical discs [7].

Initial experiments were far from reaching the theoretically high data density. With many advances of the experimental setups, the spot size, which dictates the dimensions of the microgratings, was reduced towards the resolution limit [7]. These small microgratings offer the potential to store 500 GB on one disc. However, improvements concerning the photosensitive materials are still required. This involves an optimization of the photochemical processes in the storage materials, which play a key role in holographic data storage.

To advance the characterization of photopolymer materials, a dynamic disc system was implemented by S. Frohmann. With length-coded data storage in a disc drive, the dynamic processes during recording were analyzed [8]. The findings show that using linear storage media, only a small number of layers filled with data can be stored. Clearly, nonlinear media are required to achieve multiple layers with a sufficient refractive index contrast and diffraction efficiency.

As the characteristics of photopolymer materials are closely related, they cannot be directly measured or adjusted. On top of that, inhomogeneities of the photosensitive medium yield variations of the photochemical and optical effects [8]. To explain and confirm the experimental results, the diffraction effects during the readout of the microgratings should be analyzed in detail by mathematical modeling. In this way, parameters such as saturation can be investigated separately.

A major contribution to this task is given in this thesis. To analyze the diffraction of focused laser light by microgratings during readout, a suitable mathematical tool has been devised. In the first step, it has been used successfully to describe the diffraction of light by resolution-limited microgratings, which are recorded in a linear medium.

With this method, the effective size of the microgratings is determined, which describes the spatial selectivity during readout. To assess the prospects of wavelength multiplexing for higher data capacity, the spectral selectivity of microgratings is directly analyzed using mathematical modeling. Advantageously, this provides additional insight to the diffraction effects which take place.

The influence of saturation of the recording material on the microgratings is analyzed as well and the results are compared to the resolution-limited microgratings. For mul-

tilayer data storage, appropriate recording schedules are derived, which account for the material consumption by partially overlapping layers. This leads to an assessment of the prospects of multilayer microholographic data storage in photosensitive media.

The thesis starts with a short introduction of the common optical data storage technology. Possible ways of increasing the capacity of conventional optical discs are outlined, and approaches to data storage in multiple layers are summarized. After that, the principle of microholographic data storage and of the recording process in the storage medium is introduced.

Chapter 3 gives an overview of holographic gratings from plane-wave gratings to localized gratings. Possible ways for mathematical modeling of the diffraction of light by these gratings are described. Chapter 4 is focused on the analysis of resolution-limited microgratings in a linear recording medium. First the mathematical tool which is used to calculate the diffraction of a focused beam by such gratings is introduced. With this method, the effective width and depth of these gratings are determined. Spectral characteristics of such gratings are investigated as well.

Saturation of the photosensitive material leads to larger gratings with a different structure, which is described in Chapter 5. The changed diffraction effects during readout of these gratings with saturation are modeled, which lead to a comparatively small effective size of extended microgratings based on their three-dimensional structure. The chapter includes an analysis of the wavelength selectivity of these gratings.

Holographic data storage with many layers in the whole volume of a disc requires nonlinear recording media, which is demonstrated in Chapter 6. In a first step, the consumption of material dynamics by stored data tracks and layers is analyzed. Data storage in multiple layers in a saturating recording medium involves partially overlapping gratings. A procedure to calculate recording schedules for equal diffraction efficiencies of all layers is devised, which accounts for this partial overlap.

Finally, the prospects of nonlinear photosensitive media with a two-photon recording mechanism are investigated in Chapter 7. The findings pave the way for further improvements which are required for volumetric data storage in two-photon media.

2 Optical storage technologies

This chapter gives an introduction and an overview of the current optical storage technology and the prospects of further developments. It is outlined that high-capacity discs for future archiving tasks can only be achieved by storing data in multiple layers.

Section 2.1 reviews the conventional optical data storage solutions from CD to Blu-ray discs (BD). The principle of the storage technology is described using the example of the CD. Beginning by double-layer discs, Section 2.2 describes the challenges and the prospects of multilayer data storage for higher capacities. To complete the section, a collection of other approaches towards data storage in the volume of a disc is given.

Due to the fundamental limits of multiple reflective layers, data should be stored as localized reflective bit patterns in the volume of a transparent disc. With this concept, one way to achieve high-capacity multilayer data storage is microholographic recording. The microholographic data storage system is designed similar to the standard optical drive. An introduction to the storage system developed by Orlic et. al. and to holographic recording is given in Section 2.3.

2.1 Conventional optical disc systems

Throughout the development of conventional optical data storage, including CD, DVD and BD, the principle of this technology stayed the same, with smaller laser spots for higher capacities. Figure 2.1 shows a cross section of a CD with a thickness of 1.2 mm. Data is stored as pits and lands along a spiral track. This structure is first imprinted on a disc which is made of polycarbonate. After that, the disc is covered with a reflective layer and protective lacquer and finally finished with a label imprint.

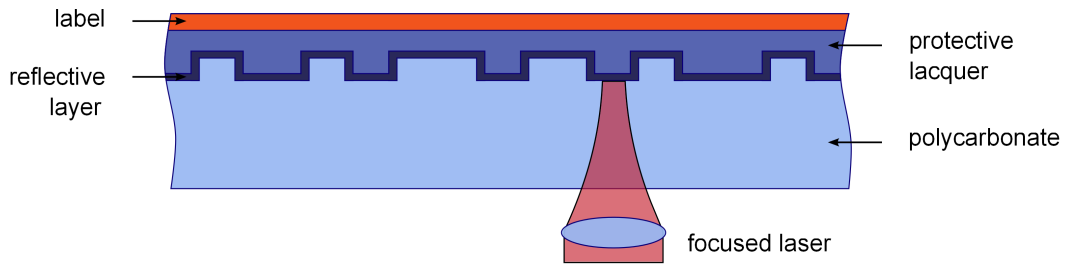

Figure 2.1: Cross sectional view of a CD with a laser beam for readout.

For data retrieval, an infrared laser (780 nm) with a numerical aperture of 0.45 is focused on the reflective layer of the disc. In the data track, the step height between pits and lands equals a quarter of the used wavelength [10]. Each time the laser moves across such a step, destructive interference lets the reflected signal drop to a value close to zero. Basically, each step from pit to land or vice versa has the meaning of a logical one. For further information, a typical optical pickup head system, which consists of lenses to focus the beam and a photodetector to read the signal, is described in [9]. Many details on technical aspects of optical data storage such as automatic focusing and tracking, access time and error correction can be found in [10].

In contrast to the read-only format (CD-ROM), recordable discs (CD-R) contain a spiral groove to guide the laser, covered with a thin layer of organic dye. When the writing laser is focused on the dye layer, the optical properties of the dye are permanently changed. In rewritable discs (CD-RW), the writing laser changes the crystal forms of an amorphous recording surface [1]. During readout, the modulation of the intensity of the reflected laser is the signal which contains the digital data.

For stable counting of the bits and to optimize the data density, the data is encoded so that pits and lands are balanced appropriately. An introduction to the coding scheme in optical discs is given in [7]. In summary, the data is encoded using EFM (Eight-to-fourteen modulation), which always produces at least two zeroes between any two ones. On the CD track, bits are written with NRZI encoding (Non return to zero, inverted) to guarantee that each pit and land extends over at least three bit clock cycles.

Optical disc	CD	DVD	BD
Laser wavelength	780 nm	650 nm	405 nm
Numerical aperture (NA)	0.45	0.60	0.85
Track pitch (µm)	1.60	0.74	0.32
Typical capacity	700 MB	4.7 GB	25 GB
Substrate/cover thickness	1.2 mm	0.6 mm	0.1 mm

Table 2.1: Figures and dimensions of optical discs [11]

Following the path beginning at the CD with 700 MB, data capacities of optical discs were increased using smaller and smaller spot sizes and grooves. This was achieved basically by lasers with shorter wavelengths and by increasing the numerical aperture of the focused laser beam, as summarized in Table 2.1. Some additional amount of increase of the storage capacity was achieved by coding techniques.

The Blu-ray disc [12, 13] with a capacity of 25 GB now marks the third generation of optical disc technology, using a blue-emitting (405 nm) GaN laser diode [14]. The optical pickup of the Blu-ray disc system has a numerical aperture of 0.85 and focuses the laser beam through a protective layer with a thickness of only 0.1 mm [15].

Finally, further increase of the data densities per layer is hardly feasible because of the physical limits imposed by diffraction of light. Increasing the numerical aperture and decreasing the optical wavelength, the spots could only be slightly smaller, at the cost of even lower system tolerances.

2.2 Multilayer and 3D optical data storage

The next logical step to increase data storage capacities in an optical disc is multilayer data storage by adding more layers to one disc. The double-layer DVD [16] with 8.5 GB was a step in that direction. However, the costly production of discs with multiple reflective layers, including requirements such as high precision and low tilt tolerances, restricts this development. More importantly, there is a general limit, as the physi-

cal trade-off between layer reflection and transmission offers only limited potential to enhance the storage capacity [6].

Recently however, Sony Corporation and Panasonic Corporation announced a new standard for optical discs intended for professional use [21]. The new *archival disc* is a double-sided disc with three layers on each side. It is an advancement of the Blu-ray technology, using a 405 nm laser and a numerical aperture of 0.85. Starting with 300 GB per disc, they aim to reach 1 TB per disc using signal processing techniques and multi-level recording [21].

Transparent discs, such as a four-layer optical disc with transparent optical switching layers [17] and inorganic discs [18–20] are also considered. Multilayer recording in the volume of a disc basically requires a transparent and homogeneous recording material with low absorption. In addition to layered media, techniques which use the entire volume of a storage medium have been investigated. Some of them involve fluorescent dyes or nanoparticles, for example three-dimensional data storage in a photopolymer with a fluorescent dye [22] and rewritable polarization-encoded recording [23].

Another approach is based on metal nanoparticles or nanostructures which induce surface plasmon effects during readout. Zijlstra et. al. [24] demonstrated multiplexed optical recording in a multilayered stack with thin spin-coated layers containing gold nanorods. Data was stored in this medium by photothermal reshaping of the nanoparticles and read out with two-photon luminescence [24]. A similar technique using metallic nanoparticles and a different design with nanoslits in a thin metallic film [25] were also studied.

Reducing the spot size by superresolution was also proposed [26–28]. Recently, two-photon induced optical data storage with a high-NA annular objective was experimentally demonstrated [29]. A similar concept is two-photon 3D data storage with an extremely high numerical aperture using a liquid immersion objective and fluorescent data bits [30, 31]. However, the use of an immersion lens requires even higher precision and stability of the position of the optical pick-up on the rotating disc, especially in connection with mechanical requirements of daily use.

2.3 Microholographic data storage

Microholographic recording [32–35] offers a new storage solution which will be compatible with the established optical disc technology. Data is stored in the entire photosensitive volume of a transparent disc. The disc has the same diameter as a DVD and consists of a photopolymer sandwiched between two substrates. In the photopolymer, the data bits are recorded as volumetrically localized holographic reflection gratings in multiple layers [6].

Within each layer, the data is written bit-wise in tracks similar to those of a conventional optical disc. Capitalizing on the strong volume localization of microgratings, this multilayer approach aims for capacities of the order of a Terabyte, while maintaining the drive system cost-effective and downward compatible with a standard optical disc drive [35]. Similar to combined CD/DVD drives, this offers the appreciated possibility to include all of the known optical disc technologies in one drive.

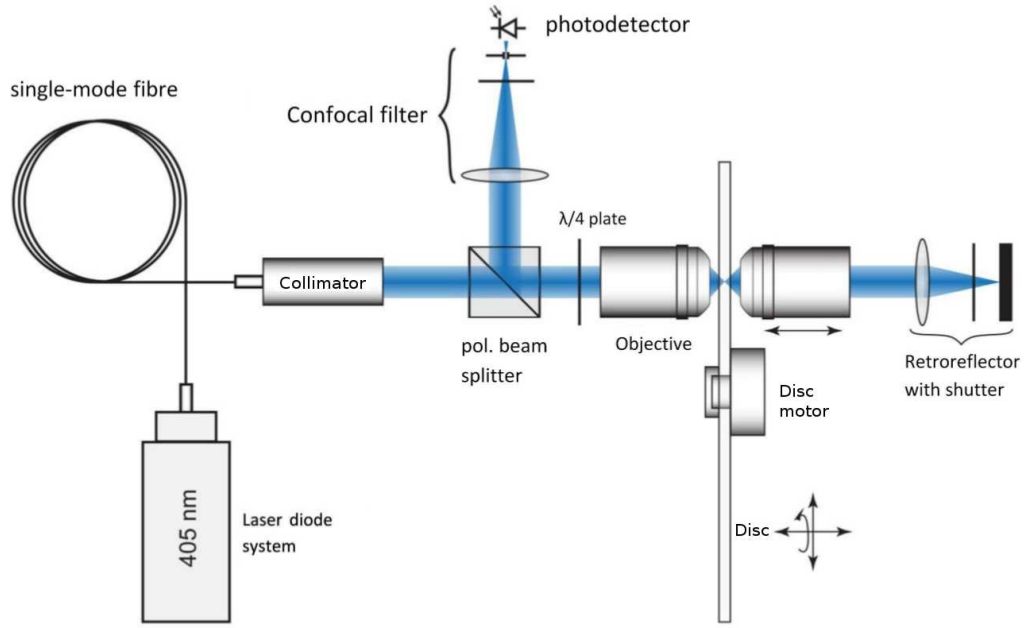

Figure 2.2: The optical data storage system [7] with two identical objectives (NA 0.75 or 0.6).

A microholographic data-storage system using a single-sided optical pickup was proposed by Saito and Kobayashi [34]. In contrast, the system developed by Orlic et. al. uses a standard optical pickup with an additional reflecting unit on the other side of the transparent disc [6, 7]. Figure 2.2 shows the optical system, which is described in

detail in [7]. An objective with a high numerical aperture focuses the reference beam onto a point in the storage medium. The reflecting unit, which consists of a second identical objective and a retroreflector unit, mirrors the beam into its counterpropagating part. Behind the $\lambda/4$ plate, the beam is circularly polarized. The retroreflector consists of a lens which focuses the beam on a plane mirror, which greatly improves the stability of the focus.

As shown in Figure 2.3, the two spots overlap exactly inside the disc, creating an interference pattern which induces a local change of the refractive index of the recording medium. The processes in the photopolymer layer, which induce this index change, are described on the next pages.

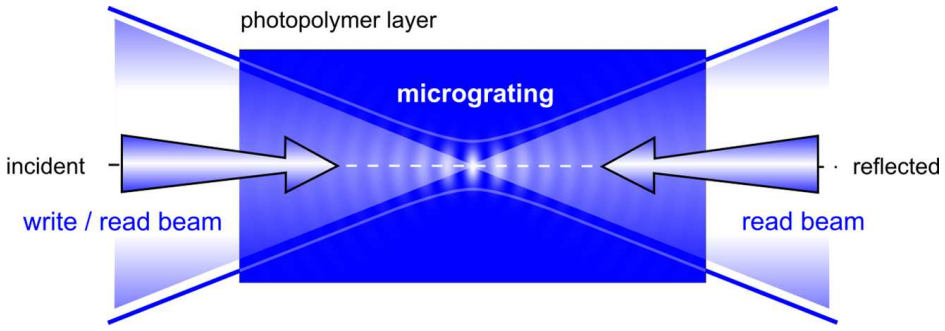

Figure 2.3: Illustration of a micrograting created by two focused laser beams [36].

The recorded pattern is a reflection grating with a diameter as small as the wavelength and a depth of a few micrometers. It is called a micrograting because of this small size. When the laser focus is placed on this structure during readout, the signal is reproduced by diffraction. Reflection gratings and in particular the three-dimensional structure of microgratings are described in full detail in the subsequent chapters.

During readout, the reflector unit is blocked by a shutter. When the focus is moved along a data track, the microgratings diffract the reference beam and reconstruct the modulated signal beam which is then directed to a photodetector. To improve the signal, a confocal filter with a pinhole is placed at the optical image of the focused signal beam. It obstructs scattered light and signals from adjacent data layers, which widely lowers interlayer crosstalk.

2.3.1 Photopolymerization

As recording media, two different photopolymers are used with peak absorption at 532 nm and 405 nm, respectively. Photopolymer films usually contain photoinitiators, a sensitizing dye, some monomers, and a binder to stabilize the material. Several different material types are available, including acrylamide-based free-radical systems and epoxy resin photopolymers [37].

When the material is exposed, light is absorbed by the dye, which is selected for a narrow range of wavelengths. Via initiator molecules, monomers are activated, and the polymerization starts. The active monomers continue to build chains as long as monomers are available until this process is terminated. The dominant termination mechanism depends on the material. Polymer chains can be finished by free monomer radicals [38], by other polymer chains with an active tip or with other added substances such as chain transfer agents [39, 40].

Polymerization induces a change of the refractive index so that the exposed intensity pattern is stored in the material as a phase hologram. This index change is induced by the varying concentrations of both polymers and monomers and by a difference of the refractive indices of these [41]. The monomer concentration gradient induces diffusion of monomers from the darker areas into the fringe areas with higher intensity of light, which enhances the index modulation. On the other hand, diffusion of short polymer chains and radicals from bright to dark areas may decrease the index modulation [42].

When the monomers polymerize, the material usually suffers shrinkage [37, 39]. This may shift the hologram to a smaller wavelength, compensated partly by a global index change. Besides, the polymer may develop a thickness variation [43] and it may bend or even peel off the substrate. To prevent these issues, the shrinkage of the recording material should be below 1 % [7].

For the best diffraction efficiency in all data layers, a high dynamic range and low absorption and scattering of light by the material are important. Some materials need prior exposure or fixation of the recorded gratings by uniform exposure or by heating. More requirements and the properties of various types of recording materials are summarized in [8].

2.3.2 Aprilis cationic ring-opening (CROP) photopolymerizable material

Aprilis CROP materials contain a type of monomers with a ring which opens during polymerization. When the material is exposed, the photoinitiator releases an acid [7]. A H^+ ion of this acid is bound by a monomer, which becomes a cation and starts the polymerization. When a monomer is bound to the end of a growing polymer chain, the positive charge propagates to it.

For a high spatial resolution of the recording material, the polymerization has to be stopped. There are two ways to stop the growth of polymer chains. Either both ends connect to a ring or an acid residue anion released by the photoinitiator is attached to the end of the chain [7]. The finished polymer chains or rings have to be smaller than the grating period of the hologram, which is half a wavelength for reflection gratings.

Advantageously, Aprilis CROP materials show low shrinkage compared to free-radical polymerizable materials [6, 44]. However, microgratings in currently available blue-sensitive media still need floodlight fixing [7].

While the technology described here aims at permanently stored microgratings, other recent research is focused on rewritable microholographic recording which may be realized using polarization-sensitive (photoanisotropic) materials. These include compounds which work similarly to liquid crystals, orienting themselves according to the electrical field as proposed in [45]. Another way is multilayer polarization-encoded data storage using photoisomerization, which is enabled by azo dyes [23, 46]. These compounds switch between two different molecule structures when they are exposed by light of a certain wavelength and polarization. This induces a reversible change of the refractive index [8].

In this chapter, optical storage technologies from CDs to BDs have been explained. Possible ways of increasing the capacity of optical discs have been specified. Finally, microholographic data storage, which is a promising technique to store data in the volume of a disc, has been introduced. The special structure of microgratings and their properties are explained in the subsequent chapters. As a foundation for the study of localized gratings, the next chapter begins with a concise review of different types of holographic gratings.

3 Volume holography and microgratings

The data bits in microholographic data storage are stored as microgratings. These volumetrically localized holograms, which are produced by focused laser beams, are introduced in this chapter. In Section 3.1, a short introduction to holographic volume gratings is given. Various types of these can be constructed by means of plane waves. Without delving into the field of photonic crystals, the basic ideas of diffraction of light by plane-wave gratings are summarized.

Due to their small size compared to plane-wave gratings, microgratings have special characteristics which are described in Section 3.2. To calculate the diffraction of focused light by these gratings, a suitable method must be chosen. For this, the chapter ends with a collection of available mathematical tools, focused on their properties and drawbacks.

3.1 Holographic volume gratings as plane-wave gratings

The optical interference of two or more coherent plane waves constitutes a periodic pattern. After having been recorded in a suitable optically sensitive medium, for example a photopolymer, this pattern can be described as a spatial modulation of the absorption constant or the refractive index of this material. The hologram is called an amplitude hologram or a phase hologram, respectively. In this work, only phase holograms are considered. The absorption of photopolymers used for volume holography is typically small and does not contribute to the diffraction process.

The orientation and the number of plane waves which are applied decide the structure of the volume grating. There are three different grating types, which are illustrated in Figure 3.1. Two plane waves always produce a one-dimensional grating, which means

that it is built up of parallel planes, shown on the left. Using at least three plane waves, two-dimensional gratings as in the middle of Figure 3.1 are produced. To record a three-dimensional grating, as shown on the right, it takes at least four plane waves.

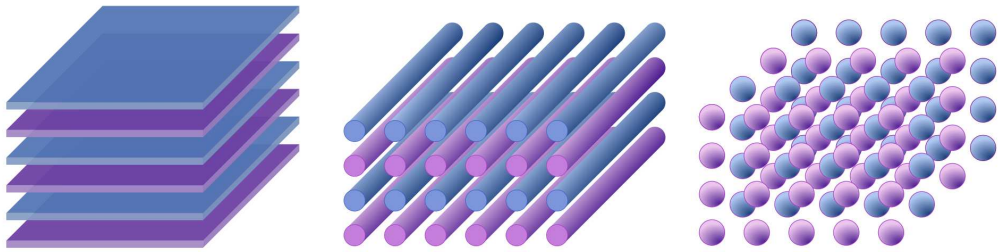

Figure 3.1: One-dimensional, two- and three-dimensional grating structures (from left to right).

One-dimensional plane-wave gratings can be further classified into transmission gratings and reflection gratings. Both types differ in the way the diffraction efficiency depends on the thickness of the material. The propagation directions of the recording waves determine the structure of a plane-wave grating as illustrated in Figure 3.2. When the two plane waves come from the same side of the material, a transmission grating is recorded. By contrast, a reflection grating is produced when the waves travel in opposite directions.

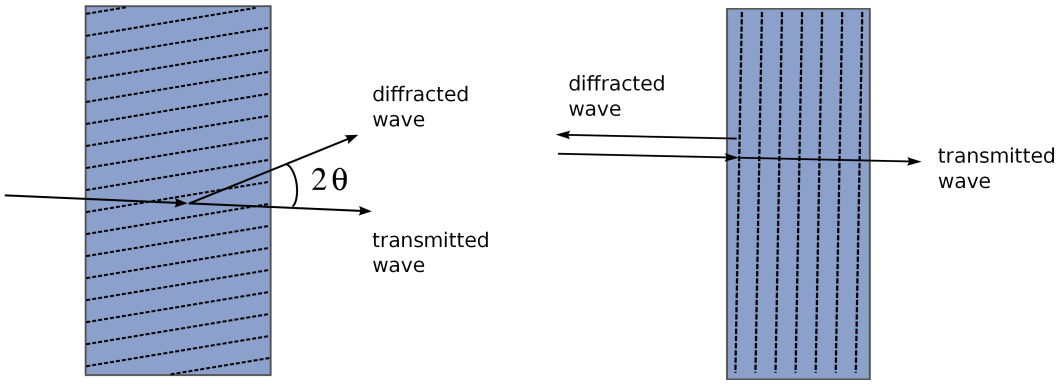

Figure 3.2: A transmission grating (on the left) compared with a reflection grating (on the right), with arrows indicating the propagation of plane waves.

The grating fringes of 1D gratings can be imagined working like partial mirrors which

reflect the incident light waves. The periodicity of the grating limits the specular reflection to particular wave vectors. As for diffraction of X-rays by crystals, the diffraction of light by holographic volume gratings basically can be described by Bragg's law

$$2\Lambda \sin\theta = m\lambda \ , \tag{3.1}$$

where Λ is the grating period, $m = 1, 2, 3, \ldots$ the order of diffraction, λ is the wavelength and θ is the angle of incidence of the plane wave. It is defined as shown in Figure 3.2. Volume-type holographic gratings are highly selective, so that the diffraction efficiency decreases rapidly at off-Bragg incidence or mismatch of the wavelength.

The early theories which describe holographic volume gratings are the so-called *kinematic theories*. They assume that no depletion of the incoming wave occurs when the wave is diffracted by the grating. These methods are not suitable for gratings which produce high diffraction efficiency and were soon replaced by dynamic theories [47].

Herwig Kogelnik [48] developed a mathematical theory for thick holographic gratings, the coupled-wave theory. It starts with an ansatz to solve the Helmholtz equation. A detailed description of this theory and more can be found for example in the book by R. R. A. Syms [47]. The coupled-wave theory assumes a plane wave incident on a sinusoidal plane-wave grating at or near the Bragg angle. Most importantly, only two significant light waves are taken into consideration: the reference wave incident on the grating and the diffracted plane wave which leaves the grating.

In contrast to the coupled-wave theory by Kogelnik, the rigorous coupled-wave theory (RCWA) by T. Gaylord and M. Moharam [49] includes all the relevant coupled waves as well as the boundaries of plane-wave gratings. It yields a system of coupled linear differential equations and can also be used to describe more complex periodic volume grating structures like photonic crystals [50]. This method basically applies only to thick and laterally extended plane-wave holographic gratings. Nevertheless, coupled-wave theory can be used to estimate the diffraction efficiency of localized holograms as a simple approximation.

3.2 Localized gratings - microgratings

The central topic of the thesis is diffraction of light by microgratings. Unlike the plane-wave gratings described above, which are recorded using extended and collimated beams, microgratings are produced using beams with high NA which are focused to small spots. These gratings typically extend over a few micrometers in each of the three dimensions. Produced by two counterpropagating beams as in Figure 3.3, the gratings in this work are reflection-type microgratings, with a grating period of half a wavelength. The smallest diameter of such a micrograting is about one wavelength.

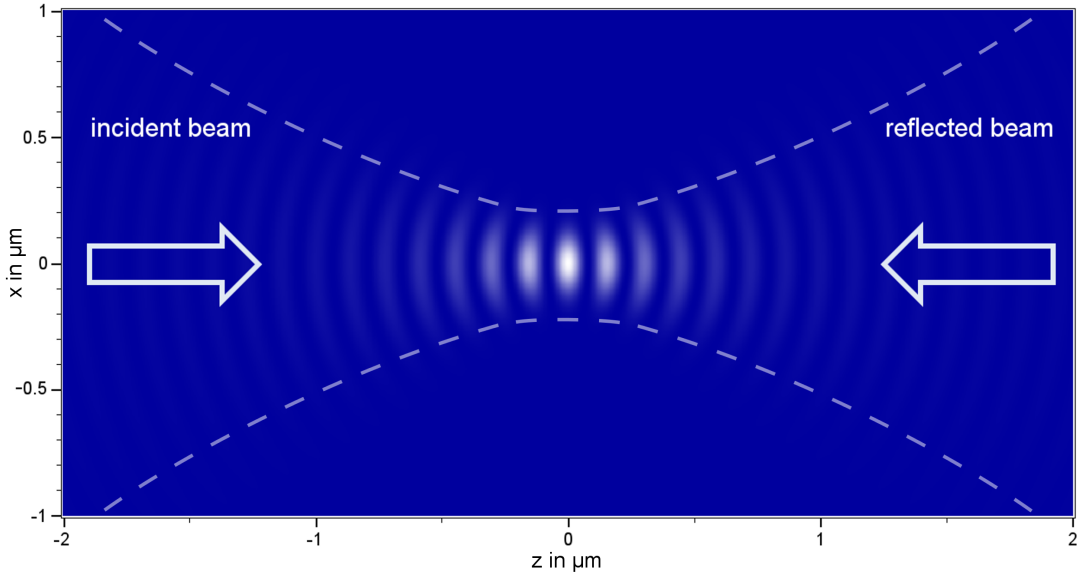

Figure 3.3: A micrograting in a linear recording material with a refractive index of $n_0 = 1.5$, recorded with a wavelength of 405 nm and $NA = 0.75$.

Figure 3.3 shows a calculated resolution-limited micrograting written with two Gaussian beams at a wavelength of 405 nm with $NA = 0.75$ in a recording material with a refractive index of $n_0 = 1.5$. This type of grating is analyzed in Chapter 4. The refractive index contrast of the grating varies gradually. Due to the interfering phase fronts of the focused beams, the grating consists of curved grating fringes.

The specific structure of a micrograting depends on the recording material and on aberrations of the light waves. A resolution-limited grating may exist only in a linear recording material and without any aberrations. If the exposure is high enough to saturate the material, the microgratings get larger, as analyzed in Chapters 5 and 6.

The small size of microgratings changes the way that light is diffracted. As following Huygens' principle [51], the waves emerging from each point in the grating can be thought of as spherical waves which add up coherently to form the diffracted field. Due to the limited size of microgratings and the curved grating fringes, these waves do not form an extended plane wave as in a plane-wave grating.

3.3 Methods for modeling the diffraction on holograms

3.3.1 Solving the Helmholtz equation

Calculating the diffraction on a micrograting in the best way would require solving the Helmholtz equation for the electric field in the presence of the grating:

$$\nabla^2 E(\vec{r}) + k_0^2 \, \varepsilon(\vec{r}) E(\vec{r}) = 0 \, . \tag{3.2}$$

As the dielectric constant $\varepsilon(\vec{r})$ includes the volumetrically localized, sub-wavelength grating structure, this equation can only be solved with approximations.

The whole micrograting structure cannot be solved with Kogelnik theory [47, 48], but still this theory can be used in order to estimate the diffraction efficiency. This was done by S. Orlic [52]. Maintaining the calculation feasible, some approximations were required. Basically, she let the refractive index be constant along the optical axis, and the thickness of the hologram was limited to about twice the Rayleigh length. Hence, the index modulation along the longitudinal axis and the curvature of the structure were not included. The focal region of the micrograting, where it resembles a plane reflection grating, is the only part which can be described that way.

A full analysis of the mechanisms of diffraction at a micrograting however should take account of its entire structure. The interference pattern with its curvature is of particular importance when Bragg diffraction and wavelength selectivity are concerned. The whole structure including the modulation of the grating index in three dimensions requires a calculation method which goes beyond the coupled-wave theory. This method should be suited for current desktop computers.

Numerical methods for calculation of the diffracted light which emanates from a diffracting structure have been considered in the literature. Generally, there are different ways

to solve the Helmholtz equation with computational electrodynamics. One of these, the Beam Propagation Method (BPM), has been applied to reflective gratings, but this involves solving a large system of linear equations [53]. Two other commonly used numerical methods for solving the Helmholtz equation are the finite-difference time-domain (FDTD) [54, 55] and finite element methods (FEM) [56].

In FDTD, the volume to be analyzed is discretized as a Yee mesh [55], composed of cubic unit cells and corresponding time steps. FDTD requires sufficiently fine meshes, not least because of the 3D grating region, and this can exceed the memory of current desktop computers, which is not intended in this work. An estimation enlightens this: The 3D mesh with the micrograting requires at least 10 points per half-wavelength. This yields a grid-cell size of at most 13.5 nm in each dimension, so that a volume with dimensions like $(13\ \mu\mathrm{m})^3$ will require at least a billion grid points to be stored and computed. A volume with 10^8 grid cells already needs roughly 10 GB of memory (100 Bytes per grid cell) [57, 58].

Besides, refinement of the FDTD grid implicates an equivalent refinement in the time domain to avoid numerical dispersion effects, which will further increase the computation time. Another issue is that in reflection-type microgratings with low index contrast, the weak diffracted field propagates in the same region as the incident field. In FDTD, the counterpropagating field must be separated from the incident field which may produce errors.

FEM has completely different, highly adaptive grid patterns with polygons or polyhedrons [59], which may need fewer samples than FDTD to reach a sufficient accuracy. To analyze whether and how this can be applied to microgratings is beyond the scope of this work. However, regarding computation time, memory and separation of the weak field, FEM may show some of the drawbacks of FDTD as well. The system of linear equations might become large. Altogether these methods to solve the Helmholtz equation are not practical for calculating the diffraction of light by microgratings.

3.3.2 Diffraction integrals for microgratings

The diffraction of light by holographic microgratings can be computed with diffraction integrals. This has the advantage that the diffracted field is computed directly, following Huygens' principle. To analyze the spectral properties of microgratings and Bragg dephasing effects, the phase structure of the grating and of the incident light has to be included. McLeod *et. al.* [33] calculated the diffraction efficiency of microgratings for optical data storage using an overlapping integral with Gaussian beams which did not include the phases of the beams. With this restriction, larger microgratings due to saturation of the recording material would yield incorrect results.

As for the Gaussian beams, the paraxial approximation is known to be of limited validity for high-NA beams. The propagation of the beam through a high-NA lens can cause some modifications of the wavefront. Corrections for Gaussian beams can be found in [60–63]. Non-Gaussian corrections are usually expressed in terms of Bessel and Hankel functions or other functions with cylindrical symmetry [63, 64]. When the readout beam is shifted laterally, the resulting 3D integrals can only be solved numerically. Additionally, non-Gaussian corrections can be expected to be smaller than aberration effects which are induced by the thickness of the storage material. Therefore, the analysis in this work is carried out based on Gaussian beams without corrections.

A different approach for calculating the distribution of strongly focused light involves Fourier transformations [65]. Propagating waves are described as a superposition of plane-wave components, the coefficients of which result from the Fourier decomposition of the incoming wavefront [66, 67]. Without any approximations, the propagation of the waves in near-field regions can only be computed numerically.

Fourier treatment of microgratings begins by calculating the propagation of the waves which produce the grating. After the material function (for example a saturation function) has been applied, the Fourier decomposition of the grating at any z position is derived, which is a function of the wave-vector components k_x, k_y and the on-axis position z. Based on this decomposition, the diffracted field is computed. To correctly resolve the details of the micrograting in position space, the Fourier decomposition requires about as many samples to be stored as in FDTD, which does not provide an advantage.

Consequently, the diffraction integrals in this work are done completely in the position space. As the index contrast of the micrograting is weak, the diffracted electric field can be calculated using perturbation theory [68]. The method, which is prevalent also in quantum mechanics, is known as the first-order Born approximation.

The resulting diffraction integral can be understood as a mathematical representation of Huygens' principle of diffraction. An electromagnetic wave can be described as a summation of spherical waves, each of which emerge from a point in the wavefront [7, 51]. The Born approximation can be applied to any diffracting structure, subject to the following requirements and conditions:

- The refractive index contrast of the grating is weak and the grating is small so that the diffracted field is small compared to the incident field.
- The incident field remains unchanged without any attenuation as it propagates through the grating.
- Multiple scattering is neglected. Due to the weak index contrast, the scattered light is assumed to leave the micrograting without being diffracted by the grating a second time.

In the photopolymers considered here, the index contrast usually is of the order of 10^{-3}, and the grating is only some micrometers large in each dimension. Even for the larger gratings due to saturation, the diffracted field is much weaker than the incident field, so that the above requirements are met.

This approach has been carried out and shown to yield suitable results. It yields an integral in three dimensions [68] which, in its original form, can only be computed numerically. This implies that for every set of parameters, namely the readout wavelength or focal position, a full 3D numerical integral must be computed. Especially for extended gratings due to saturation of the recording material, which are described in Chapter 5, the calculation of the full 3D integral is very time-consuming and induces serious computational errors. To avoid these issues, an appropriate far-field approximation is devised in Chapter 4, which leaves only one dimension for numeric integration and gives accurate results.

4 Modeling the diffraction efficiency of holographic microgratings

High-density three-dimensional optical data storage is one application of microholographic reflection gratings. Representing data bits in a photosensitive material, the gratings may have various further applications. Data storage is the application considered in this work. During readout, the signal is modulated by the stored gratings according to their structure and index modulation. The goal of this work is to investigate the diffraction of focused laser light by such volumetrically localized gratings.

This chapter is focused on mathematical modeling of the diffraction of light by microgratings which are stored in a linear recording material. In such a material, the refractive index contrast of the recorded microgratings depends linearly on the intensity of the counterpropagating beams used for recording.

Saturation of the material due to the high local exposure can modify the index contrast and the structure of microgratings. Spherical aberration of the focused light which propagates through the disc modifies the grating structure as well. Both effects may influence the readout efficiency and the localization of the bits in a data track, which in turn dictates the data density. Experimental work [7, 8] is not yet directly able to reveal the real structure and size of gratings which are written in the photosensitive material. These experiments return the accumulated diffracted light as a whole.

The apparent size of a hologram shown by readout is determined by two effects. Firstly it is limited by the overlap of the intensity of the readout beam with the index contrast of the grating. Diffraction efficiency (DE) is further limited by Bragg diffraction as a result of the phase structure. If the focus of the readout beam is moved away from the focus of the grating, the DE is reduced because of the off-Bragg incidence. Consequently,

large gratings can still be well localized. However, measurements with recording and readout at several different interlayer spacings [8] indicate that the gratings are larger due to saturation of the photosensitive material response. Such gratings are studied in the subsequent chapters.

Propagation of focused light through a material implicates spherical aberration. Hence, the structure of the diffraction grating changes, basically it becomes more complex and larger. The aberration can be corrected so that it is zero in the center of the disc. The effects of aberration on recording and readout of microgratings ought to be understood on a theoretical basis as well in future calculations.

Calculation of diffraction induced by microgratings necessarily implicates some approximations. However, the structure of the grating as described in the integral should match the real structure as much as possible. The interference pattern with its curvature is of particular importance for Bragg diffraction and wavelength selectivity. The whole structure including the modulation of the grating index in three dimensions requires a calculation method which goes beyond the coupled-wave theory.

As the index contrast of the micrograting is small, the diffracted electric field can be calculated using the first-order Born approximation, which has been shown to yield suitable results. It yields an integral in three dimensions [68] which, in its original form, can only be computed numerically. Varying the parameters would require a full 3D numerical integral for each parameter set.

An efficient calculation tool for modeling of the diffraction effects has been developed. Diffraction of light by microgratings is modeled using a far-field approximation of the volume integral, which reduces the computational effort from a 3D to a 1D numerical integration.

Using this tool, which is introduced in Figure 4.1, the influence of several parameters on the diffraction efficiency (DE) can be studied. The impact of the numerical aperture on the diffraction efficiency is analyzed in order to check the estimation based on Kogelnik coupled-wave theory [48]. Next, the DE is calculated spatially resolved as a function of both lateral and longitudinal scan position. The results are compared with preceding experimental results and compared to intensity-based integrals.

Advantageously compared to the limitations of experimental work, the spectral characteristics of microgratings can be analyzed with this tool. The potential of wavelength multiplexing as a further technique to increase the data density is investigated. By shifting the readout wavelength, DE is calculated spectrally resolved to determine the wavelength selectivity of microgratings. These calculations also provide some insight into the diffraction effects which occur in microgratings.

4.1 The micrograting in a linear recording material

In a linear recording material, the local change of the refractive index is proportional to the intensity of the light during recording, provided that non-local material effects or saturation are of little account. The interference structure results in a strongly localized reflection grating. The grating period equals half a wavelength. Figure 4.1 shows such a micrograting written with two Gaussian beams at a wavelength of 405 nm with $NA = 0.75$. The recording material has a refractive index of $n_0 = 1.5$. Cross sections along the axes are shown in Figures 4.2a and 4.2b.

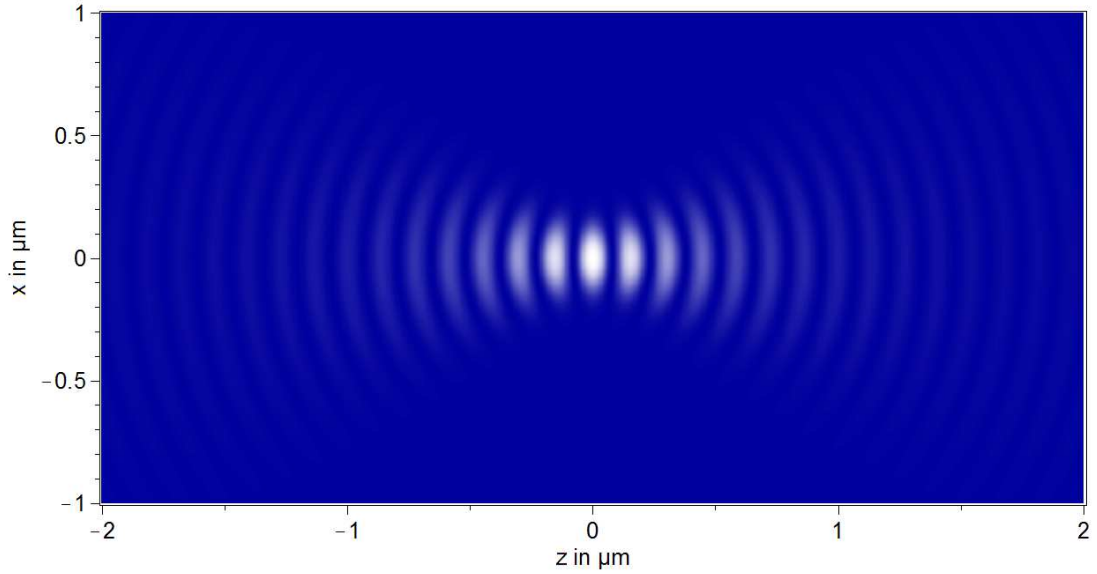

Figure 4.1: A micrograting in a linear recording material with a refractive index of $n_0 = 1.5$, recorded with a wavelength of 405 nm and $NA = 0.75$.

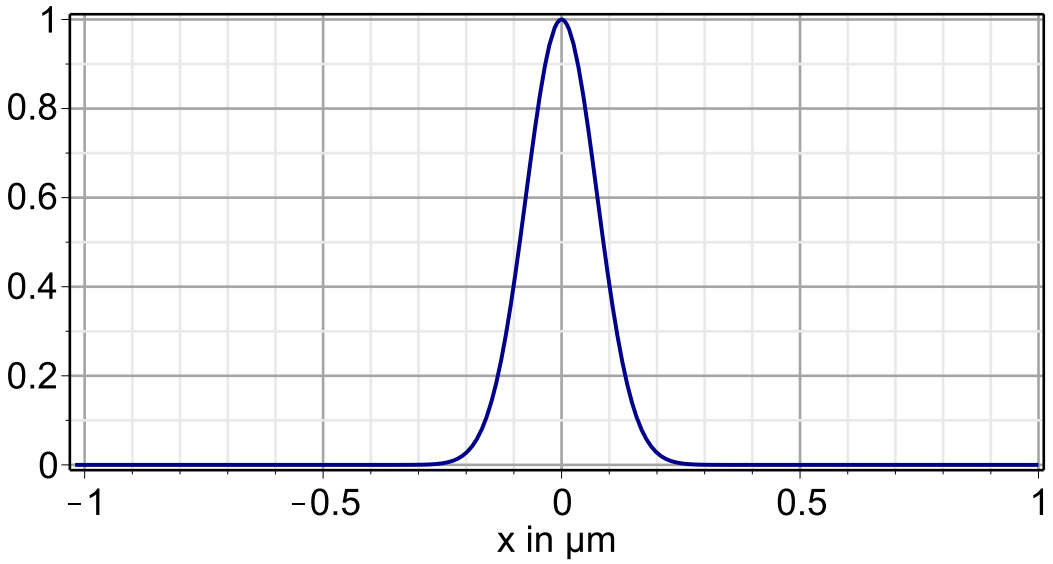

(a) Lateral cross section: normalized refractive index contrast

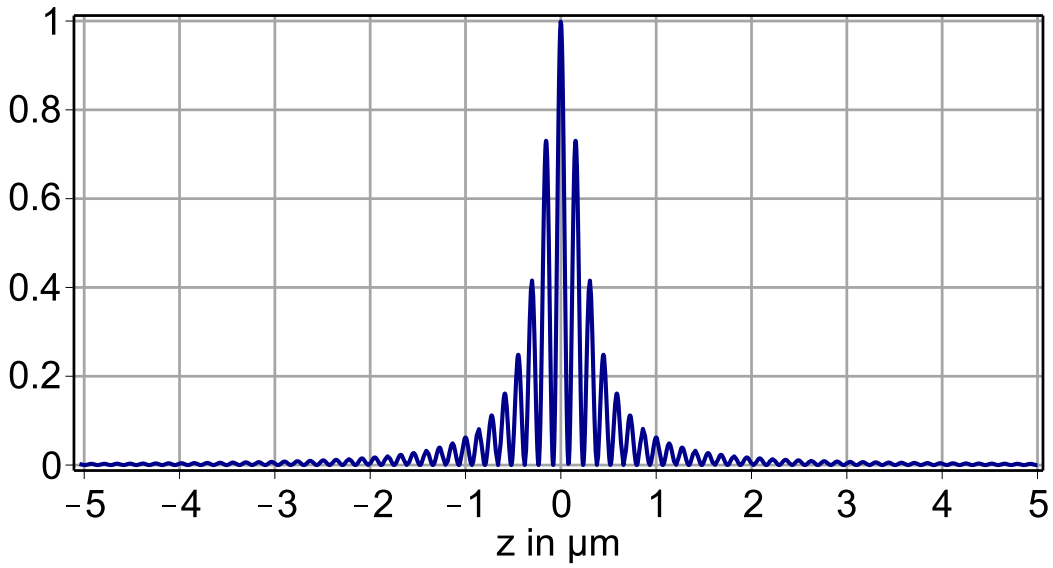

(b) Longitudinal cross section: normalized refractive index contrast

Figure 4.2: Cross sections of the micrograting.

For modeling the diffracted electric field induced by the volumetrically localized micrograting, a simplified method is introduced. The integral is based on the first-order Born approximation. Using Taylor expansion, the Green function is simplified and the integral is solved analytically in both lateral directions of the micrograting. By limiting the numerical effort to the longitudinal direction, computation time is substantially shorter compared to the 3D numerical integration.

The method is flexible when it comes to include other grating forms as long as only Gaussian functions are used in the lateral dimensions. This spans saturation effects on the shape and size of recorded gratings as well, so that the main features of these gratings are included and a variety of gratings are analyzed. The readout of microgratings with saturation and with spherical aberration and high NA has only been studied in experimental work yet, however, the real shape of the gratings can only be inferred to some extent from the measurements.

For recording of the microgratings, two counter-propagating beams are focused on a point in the photosensitive material, typically a holographic recording photopolymer. In the common focal area the intensity modulation induces changes in the refractive index of the material. The resulting modulation of the refractive index is assumed to be proportional to the intensity. This well applies to cationic ring opening polymerization (CROP) material systems used in the related experimental work [33, 35, 36].

For reading the data, a focused beam is applied. The total electrical field in the presence of a micrograting, including the incident and the diffracted part, is described by the scalar Helmholtz equation

$$\nabla^2 E(\vec{r}) + k_0^2\, \varepsilon(\vec{r}) E(\vec{r}) = 0\,. \tag{4.1}$$

The dielectric constant $\varepsilon(\vec{r})$ describes the structure of the micrograting. Dispensing with any vector field calculus greatly simplifies the calculation. Vector diffraction calculus with a Green's tensor was useful in [69] for high-density data storage with differently shaped pits and a solid immersion lens. More general articles on vector diffraction theory include [70–72]. With circularly polarized light, polarization of the electic field is irrelevant for the formation of the interference structure. For the used photosensitive materials, the change of the material due to recording does not depend on the

polarization of the incoming light. Consequently it is safe to stick to scalar equations completely.

In this chapter, the change in the refractive index is assumed to be proportional to the intensity of the incoming light. The modulated refractive index itself is described by

$$n(\vec{r}) = n_0 + \Delta n \, \frac{I(\vec{r})}{I_{max}} \, , \tag{4.2}$$

where Δn denotes the maximum index contrast. Neglecting Δn^2 as it is small, the dielectric constant is described by

$$\varepsilon(\vec{r}) = n_0^2 + 2\, n_0\, \Delta n \, \frac{I(\vec{r})}{I_{max}} = n_0^2 \left(1 + 2 \, \frac{\Delta n}{n_0} \frac{I(\vec{r})}{I_{max}} \right) \, , \tag{4.3}$$

where n_0 is the refractive index of the material before recording, and $I(\vec{r})$ is the intensity of the light during recording at a position $\vec{r}$ in the interference pattern (the grating). The electric fields corresponding to the reference and signal beam are denoted as E_r and E_s, respectively. In detail, this yields four terms

$$\begin{aligned} \frac{I(\vec{r})}{I_{max}} &= \frac{\pi w_0^2}{8} \, |E_r + E_s|^2 \\ &= \frac{\pi w_0^2}{8} \left(|E_r|^2 + |E_s|^2 + E_r E_s^* + E_r^* E_s \right) \, . \end{aligned} \tag{4.4}$$

Writing $h(\vec{r})$ for the amplitude and $\Phi(\vec{r})$ for the phase of the beam, the reference beam is described by

$$E_r(x, y, z) = h(\vec{r}) e^{i\Phi(\vec{r})} \, . \tag{4.5}$$

The signal beam propagates in the opposite direction, which is indicated by a minus sign in the z argument, so $E_s(x, y, z) = E_r(x, y, -z)$.

These four terms in (4.4) can be described as follows. In order to explain them, the expression in brackets is multiplied by E_r, to construct the situation during readout.

$$E_r \left(|E_r|^2 + |E_s|^2 \right) + E_r^2 E_s^* + |E_r|^2 \, E_s \tag{4.6}$$

The first two terms describe an attenuated form of the reference beam. The third term $E_r^2 E_s^*$, in holography usually called the conjugate image [47], carries the phase $\exp(3i\Phi(\vec{r}))$ and does not construct any physically realistic signal. In most practical

situations, it can be neglected. The fourth term is the relevant part of the micrograting, which creates the reflected beam during readout. It is given by

$$\frac{\pi w_0^2}{8} E_r^*(\vec{r}) E_s(\vec{r}) \ . \tag{4.7}$$

The beams are described as Gaussian beams as proposed by Nagy et. al. [68]. The amplitude and phase are denoted as $h(\vec{r})$ and $\phi(\vec{r})$, respectively, with

$$h(\vec{r}) = \sqrt{\frac{2}{\pi}} \frac{1}{w(z)} \exp\left(-\frac{x^2+y^2}{w(z)^2}\right) , \tag{4.8}$$

$$\Phi(\vec{r}) = k\frac{x^2+y^2}{2R(z)} + kz - \arctan\left(\frac{z}{z_R}\right) . \tag{4.9}$$

The Gaussian beam radius is

$$w(z) = w_0 \sqrt{1 + \left(\frac{z}{z_R}\right)^2} , \tag{4.10}$$

the radius of the wavefront is $R(z) = z + z_R^2/z,\ k = k_0 n_0,\ k_0 = 2\pi/\lambda_0$ is the length of the wave vector in vacuum, and the Rayleigh length is $z_R = k_0 n_0 w_0^2/2$. The beam waist w_0 is related to the numerical aperture as

$$w_0 = \frac{\lambda_0/n_0}{\pi \tan\left(\arcsin\left(\frac{NA}{n_0}\right)\right)} . \tag{4.11}$$

To keep the calculation simple, no boundaries of the recording material are accounted for. In practice a few hundred microns thick photopolymer layer is typically sandwiched between two glass substrates, each one millimeter thick. The difference of the refractive index between glass and polymer is small, which leads to very low reflection at the boundaries.

The air-glass plate boundary will cause reflections which are substantially filtered out by the confocal filter. To include the boundary in the model is not straightforward. Therefore, in order to keep the calculation simple enough, it is not taken into account. Moreover, adding the confocal filter in the model is not readily done.

In typical photosensitive materials the maximum index contrast of microgratings is small (10^{-3}). Hence, the diffraction can be described as a single scattering process using perturbation theory, which is commonly done [68]. Accordingly, the diffracted wave which is generated by the micrograting can be calculated using the first-order Born approximation [73].

The integral is given by Nagy et. al. [68] as

$$E_d(\vec{r}_1, \Delta\vec{r}) = \frac{k^2 w_0^2}{16} \iiint \mathrm{d}^3 r \frac{\Delta n}{n_0} E_r^*(\vec{r}) E_s(\vec{r}) E_r(\vec{r} + \Delta\vec{r}) \frac{\exp\left(ik\,|\vec{r}_1 - \vec{r}|\right)}{|\vec{r}_1 - \vec{r}|} \quad (4.12)$$

$$= \frac{k^2 w_0^2}{16} \iiint \mathrm{d}^3 r \frac{\Delta n}{n_0} h^2(\vec{r})\, h(\vec{r} + \Delta\vec{r}) \frac{\exp\left(ik\,|\vec{r}_1 - \vec{r}|\right)}{|\vec{r}_1 - \vec{r}|} \times \quad (4.13)$$
$$\times \exp\left(-2i\Phi(\vec{r})\right) \exp\left(i\Phi(\vec{r} + \Delta\vec{r})\right) \ .$$

The shift of the focus position of the reference beam with respect to the center of the micrograting is $\Delta\vec{r}$. This three-dimensional integral can only be solved numerically, which takes plenty of computation time and may induce numerical errors. Therefore, it is convenient and favorable to replace the Green's function with its square-root term by a simpler expression.

Because of the large distance of the output plane compared to the effective volume of the micrograting, far-field approximation is applicable. The distance of any considered point in the output plane from the center of the micrograting, r_1, is of the order of millimeters. The lateral and longitudinal dimensions of the micrograting itself are a few microns only.

Fraunhofer and Fresnel approximation however, which refer to z_1 only, are not suitable for high numerical apertures. The approximation has to account for the lateral dimensions x_1, y_1, which reach the same order as z_1. So a suitable approach has been developed. As $r \ll r_1$, the integral can be approximated as follows. The Green function is replaced using the first-order Taylor approximation of the square-root expression in the phase and leaving r_1 in the denominator. This yields

$$\frac{e^{ik|\vec{r}_1 - \vec{r}|}}{|\vec{r}_1 - \vec{r}|} \approx \frac{\exp\left(ikr_1\right)}{r_1} \exp\left[-ik\frac{(\vec{r} \cdot \vec{r}_1)}{r_1}\right] \ . \quad (4.14)$$

Now the integral (4.13) is rewritten using (4.14). Finally, the integral for the diffracted wave field is

$$E_d(\vec{r_1}, \Delta\vec{r}) \approx \frac{k^2 w_0^2}{16} \frac{\Delta n}{n_0} \frac{e^{ikr_1}}{r_1} \iiint \mathrm{d}^3 r\, h^2(\vec{r})\, h(\vec{r} + \Delta\vec{r}) \exp\left[-ik\frac{(\vec{r} \cdot \vec{r}_1)}{r_1}\right] \times \quad (4.15)$$
$$\times \exp\left[-2i\Phi(\vec{r}) + i\Phi(\vec{r} + \Delta\vec{r})\right] \ .$$

This integral can now be solved analytically in both x and y, leaving only the z direction for numerical integration.

In the following, modeling of the diffraction efficiency is performed using the integral (4.15). The parameters for the simulation are chosen according to the experimental values. The refractive index of the photopolymer is set to $n_0 = 1.5$. The index contrast is $\Delta n = 0.001$, which is a typical value for photopolymer systems used in practical demonstrations of microholographic data storage [44, 74, 75].

The write and readout beams have the parameters $NA = 0.75$ ($w_0 = 0.1489\,\mu\mathrm{m}$) and a wavelength of $\lambda = 405\,\mathrm{nm}$ for the blue laser. The green laser has $\lambda = 532\,\mathrm{nm}$ and $NA = 0.6$ ($w_0 = 0.2587\,\mu\mathrm{m}$). These values correspond to the experimental conditions, as reported in [35]. The parameters are summarized in Table 4.1.

By taking different values for Δx and Δz, the readout beam is translated in the transversal or longitudinal direction, respectively. The output plane used for the calculations is placed at $z = -5\,\mathrm{mm}$.

Laser wavelength	**405 nm**	**532 nm**
Refractive index	$n_0 = 1.5$	$n_0 = 1.5$
Index contrast	$\Delta n = 0.001$	$\Delta n = 0.001$
Numerical aperture	0.75	0.6
Gaussian beam radius w_0	$0.1489\,\mu\mathrm{m}$	$0.2587\,\mu\mathrm{m}$

Table 4.1: Parameters used for modeling of the gratings

In order to estimate the accuracy of the above method, an example of the results of the Taylor approximation (4.15) compared to the full Kirchhoff integral (4.13) is shown in Figure 4.3. It displays the intensity of the diffracted field over x at the output plane, normalized by the input power P_0, and the difference of the results produced with both methods. The difference is four to six orders smaller than the intensity, which justifies the use of the method.

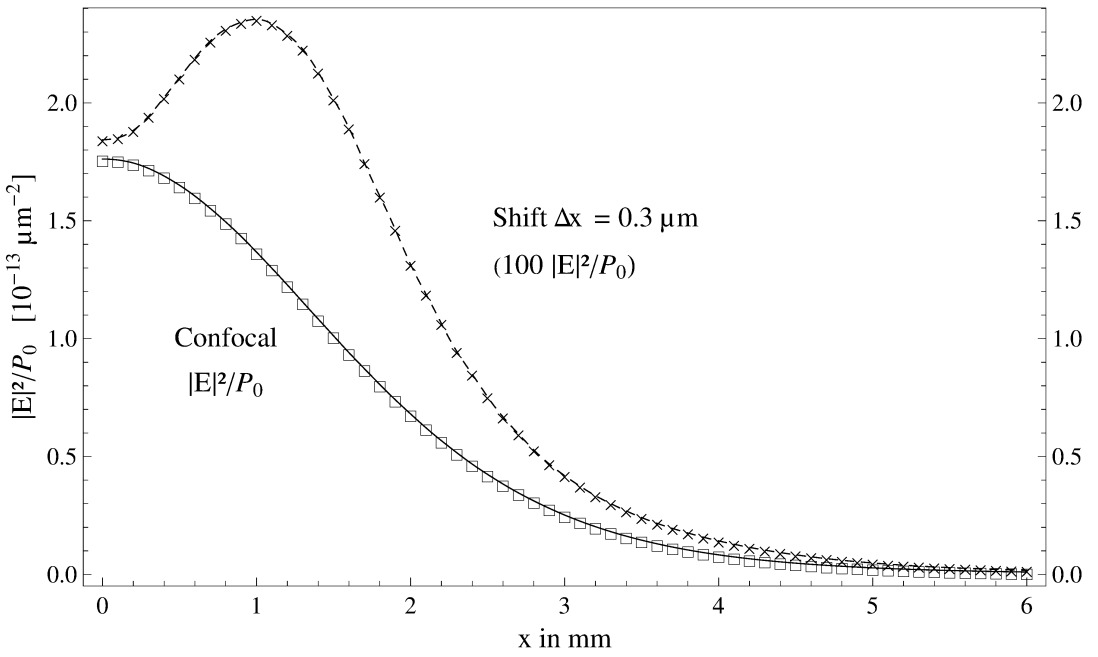

(a) Intensity at the output plane (normalized by input power P_0), with probe beam at confocal position (solid) and with probe beam shifted laterally by 0.3 µm (dashed, scaled by 100), each calculated with Taylor approximation (lines) and full integral (□, ×).

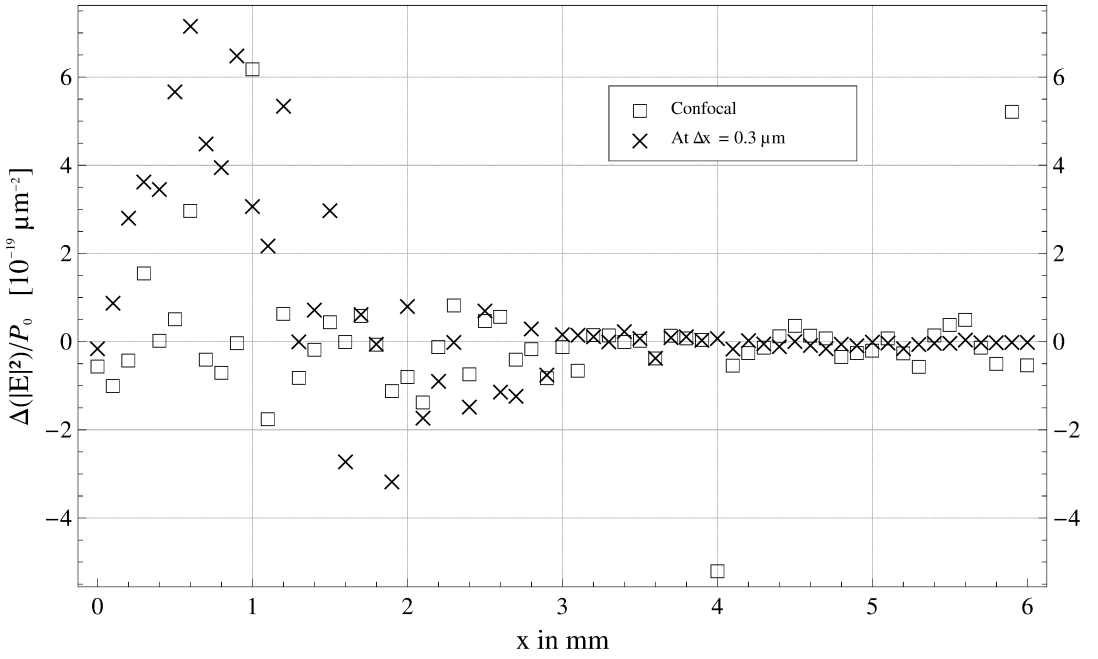

(b) Difference between Taylor approximation and full integral

Figure 4.3: Accuracy of the approximation for the integral. Parameters: $NA = 0.75$ and wavelength $405\,\mathrm{nm}$; refractive index $n_0 = 1.5$ and index contrast $\Delta n = 0.001$.

Impact of the numerical aperture

Increasing the numerical aperture (NA) of the focusing objective is a straightforward path to smaller spot sizes and higher data densities. However, as the spot size and the focal depth get smaller, the diffraction efficiency of the gratings decreases accordingly. So the benefit of NA to storage density in microholographic recording is clearly limited by losses in diffraction efficiency (DE) and signal-to-noise ratio. The diffraction efficiency of microgratings largely depends on the numerical aperture of the beams used for both recording and readout.

The grating depth can be estimated by the Rayleigh length $z_R = k_0 n_0 w_0^2/2$, which is approximately proportional to $1/NA^2$. As coupled-wave theory for reflection gratings suggests [47], the diffraction efficiency follows the square of the depth, giving NA^{-4} [6]. This estimate can now be approved. DE in Figure 4.4 is calculated with the integral method (points) and shows good agreement with this simple estimate (dashed line). An even better estimate for DE is w_0^4 by using (4.11), shown by the solid line.

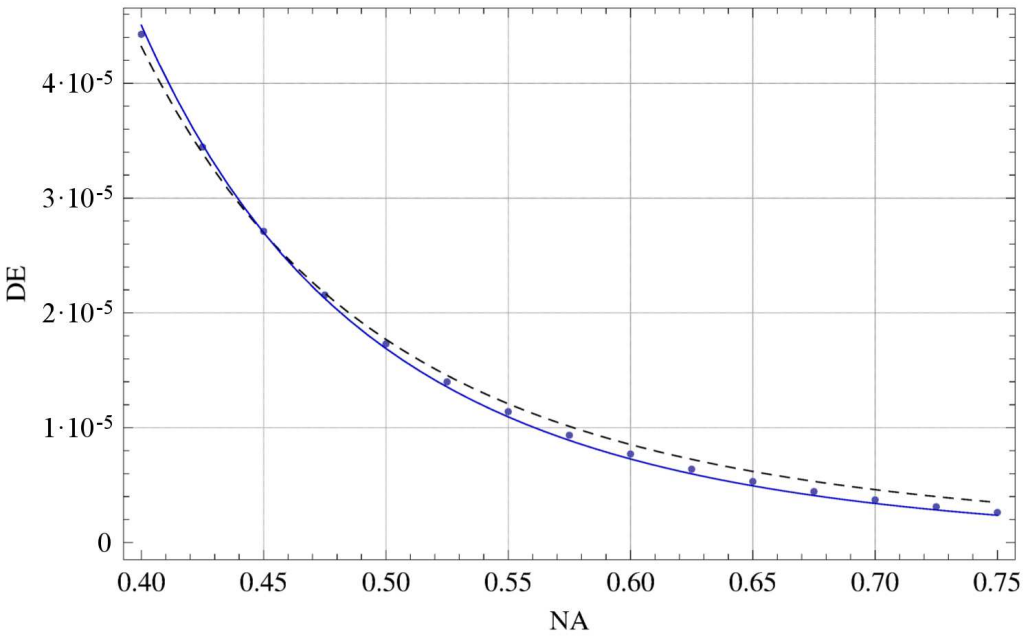

Figure 4.4: DE over NA at write and read wavelength $\lambda = 405\,\mathrm{nm}$. Refractive index is $n_0 = 1.5$ and index contrast is $\Delta n = 0.001$. Estimates: NA^{-4} (dashed) and w_0^4 (solid).

4.2 Readout of microgratings

Readout of microgratings stored in an optical disc is performed by scanning the recorded volumetric gratings with a probe beam identical to the write beam. When the read beam exactly overlaps with the grating fringes of a micrograting, Bragg diffraction yields a reflected beam propagating in the opposite direction. Diffraction efficiency (DE) is obtained by relating the reflected beam power to the incident read beam power.

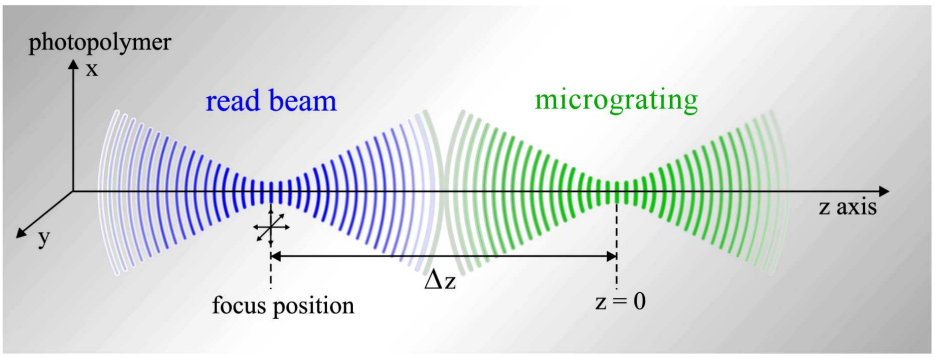

Figure 4.5: Scanning of a micrograting, placed with focus position at $\vec{0}$, with a probe beam incident from the left. The probe beam is moved longitudinally or transversally over the micrograting. Focus position of read beam is $\Delta\vec{r}$ as in (4.15), example for longitudinal scanning.

Figure 4.5 illustrates the scanning: Translating the focal position of the read beam in the lateral and longitudinal directions away from the volumetric center of a micrograting is indicated by the small arrows. As the focus is moved, the diffraction efficiency drops with the off-Bragg distance and due to the reduced overlap between the beam intensity profile and the micrograting. Spatially resolved DE corresponds to the spatial distribution of the index modulation of a micrograting and is a fundamental parameter for the achievable data density.

4.2.1 Transversally resolved diffraction efficiency

To determine the effective width of a micrograting, the diffraction efficiency is calculated when the focus of the beam is moved through the micrograting in x direction. For comparison of the integral method, a simple calculation based on the envelope of the grating structure and the intensity is carried out. The intensity of a Gaussian beam at the focus is

$$I(x,y,0) \quad = \quad \frac{2}{\pi}\frac{1}{w_0^2}\exp\left(-2\frac{x^2+y^2}{w_0^2}\right) , \tag{4.16}$$

with a full width at half maximum (FWHM) of $\sqrt{2\ln 2}\,w_0$. The transversal modulation of the diffraction efficiency can be estimated except for an empirical factor by overlapping intensity and transversal index modulation in the focal region:

$$\text{DE} \quad \propto \quad \iint \frac{2}{\pi w_0^2}\exp\left(-2\frac{(x+\Delta x)^2+y^2}{w_0^2}\right)\exp\left(-2\frac{x^2+y^2}{w_0^2}\right)\mathrm{d}x\mathrm{d}y \tag{4.17}$$

$$= \quad \frac{1}{2}\exp\left(-\frac{\Delta x^2}{w_0^2}\right) . \tag{4.18}$$

This yields FWHM $= 2\sqrt{\ln 2}\,w_0$. As the results of the diffraction integral (4.15) show, the grating readout signal and therefore its resolution is delimited basically by the overlap of the probe beam intensity with the grating index modulation.

Bragg dephasing does not induce additional significant effects in this case. The explanation is that the grating has zero curvature in the focal region, and the index contrast decreases rapidly so that the curved regions contribute little to the diffracted signal. In other words, the grating is so small that the laser is only diffracted by the central part of the grating.

Calculation of the diffraction efficiency using the diffraction integral yields a maximum DE of $2.64\cdot 10^{-6}$ for the blue laser beam with $NA = 0.75$, and $7.71\cdot 10^{-6}$ for the green beam with $NA = 0.6$, both with $\Delta n = 0.001$. The low diffraction efficiency follows from the small dimensions of the microgratings. Recorded in green, gratings are slightly larger in each dimension.

Figure 4.6 shows the diffraction efficiency, normalized (divided by its maximum value), over Δx for both laser wavelengths. The curves can be described by $\exp(-\Delta x^2/x_{\text{eff}}^2)$.

The blue wavelength yields $x_{\text{eff}} = 0.149\,\mu\text{m}$, the FWHM is 247 nm. For the green laser, the result is $x_{\text{eff}} = 0.259\,\mu\text{m}$, with a FWHM of 430 nm.

Experiments reported in [35] showed a FWHM of 197 nm (blue) and 306 nm (green). They use a confocal filter with a relatively large pinhole to block out scattered light from other layers. This pinhole does not trim the diffracted beam. The results of the calculation are in good agreement with the experimental data. Besides, x_{eff} is close to the estimate given above, $w_0 = 0.1489\,\mu\text{m}$ (blue) and $w_0 = 0.2587\,\mu\text{m}$ (green).

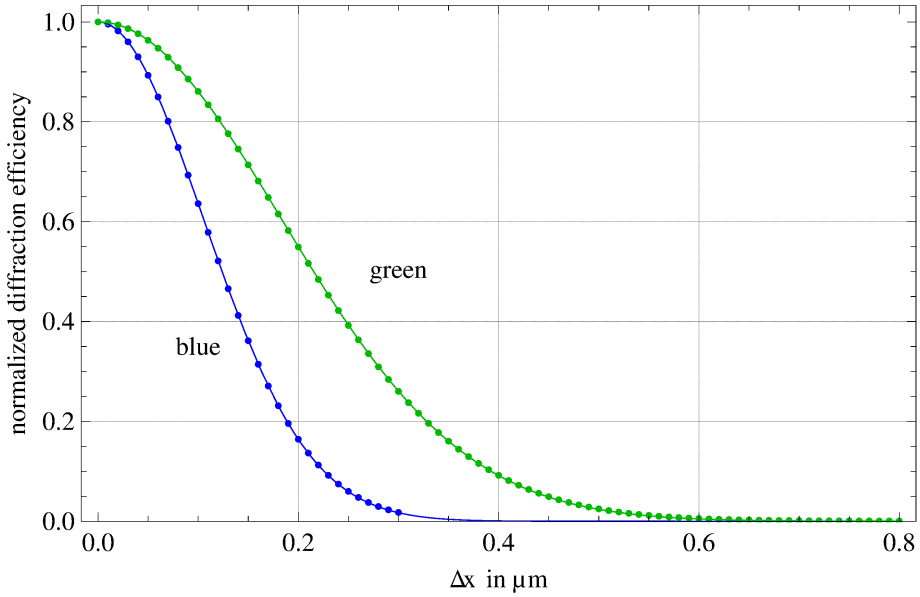

Figure 4.6: Normalized diffraction efficiency over the transversal position of the readout beam. Beam parameters: $NA = 0.75$, write and read wavelength $\lambda = 405\,\text{nm}$ (blue), $NA = 0.6$ and $\lambda = 532\,\text{nm}$ (green). Refractive index is $n_0 = 1.5$ and index contrast is $\Delta n = 0.001$.

4.2.2 Diffraction efficiency by longitudinal scanning

The diffraction efficiency depending on the focus position along the optical axis can be estimated by an intensity-based integral as well. On the z axis, the intensity of the Gaussian beam is

$$I(0,0,z) \quad = \quad \frac{2}{\pi}\frac{1}{w(z)^2} \tag{4.19}$$

with FWHM of $2z_R$. The longitudinal modulation of the DE is estimated by taking the overlap of intensity and index modulation along the optical axis:

$$\mathrm{DE} \;\propto\; \int \frac{2}{\pi w(z+\Delta z)^2}\,\frac{2}{\pi w(z)^2}\,\frac{\pi w_0^2}{2}\,\mathrm{d}z = \frac{z_R}{w_0^2}\,\frac{1}{1+\Delta z^2/(4\,z_R^2)}\,, \tag{4.20}$$

which yields FWHM $= 4\,z_R$. Calculation of diffraction efficiency using the diffraction integral is shown in Figure 4.7. The curves follow

$$\frac{1}{1+\Delta z^2/z_{\mathrm{eff}}^2}\,,$$

with the parameters $z_{\mathrm{eff}} = 0.511\,\mu\mathrm{m}$ and $z_{\mathrm{eff}} = 1.165\,\mu\mathrm{m}$ for the blue and green laser, respectively. This agrees well with the estimate given in (4.20): $2\,z_R = 0.516\,\mu\mathrm{m}$ (blue) and $2\,z_R = 1.19\,\mu\mathrm{m}$ (green).

The FWHM is 1.0 µm for the blue laser. The FWHM of 2.33 µm for the green laser matches the experimental results which yielded a micrograting depth of 2.5 µm [6]. The diffracted waves mainly emerge from the focal region of the grating where the index contrast is highest.

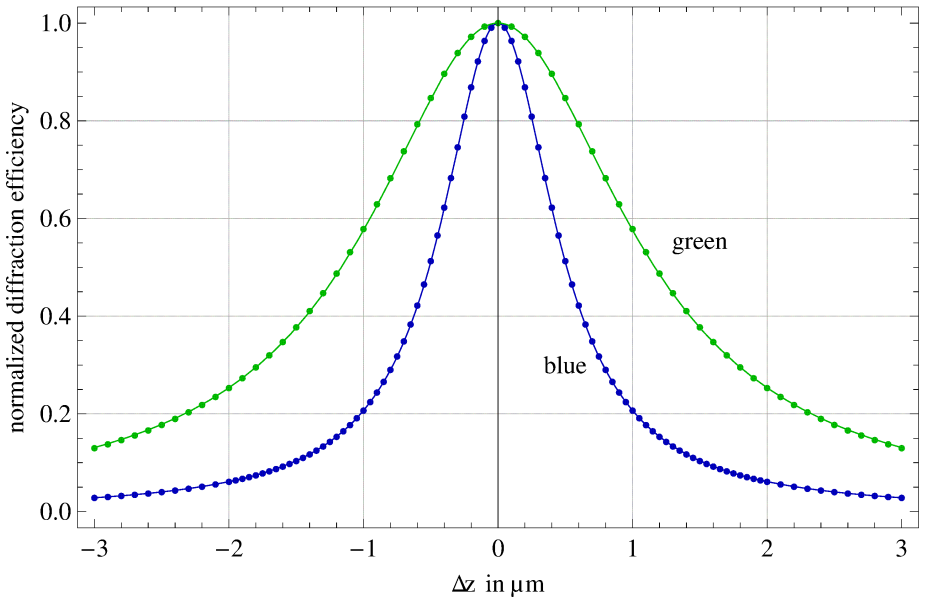

Figure 4.7: Diffraction efficiency over longitudinal position of readout beam. Beam parameters are: $NA = 0.75$, write and read wavelength $\lambda = 405\,\mathrm{nm}$ (blue), $NA = 0.6$ and $\lambda = 532\,\mathrm{nm}$ (green). Refractive index is $n_0 = 1.5$ and index contrast is $\Delta n = 0.001$.

4.3 Wavelength selectivity of micrograting

Wavelength multiplexing is one potential method for enhancing the capacity of a holographic data storage system. Enabled by the wavelength selectivity of thick holograms, several spectral channels can be used for parallel recording and readout. The potential of wavelength multiplexing for microholographic data storage was preliminary investigated in [32], using plane-wave approximation and micrograting with moderate NA.

With strongly localized micrograting as described here, the situation is different. In contrast to thick Bragg holograms, the spectral selectivity of micrograting recorded with high NA can be significantly reduced due to their limited depth and effective number of grating fringes. The useful spectral range is limited by the emission spectrum of blue emitting GaN (Gallium nitride) based laser diodes [14] and also by the sensitivity range of the recording material.

Experimental investigations on the wavelength selectivity of micrograting are challenging and require a highly sensitive spectrometer. Calculation of the diffraction efficiency as a function of the readout wavelength with the method described in this paper offers an easy way to study the wavelength selectivity of micrograting. Some related diffraction effects can be studied as well.

This calculation starts from micrograting written at the wavelength $\lambda_0 = 415\,\mathrm{nm}$, which is at the center of the range 400 to 430 nm. The results are equivalent when a different recording wavelength such as 405 nm is used.

Evaluation reveals how the diffraction efficiency changes with a shift in the readout wavelength λ. The diffraction efficiency, calculated as a function of the wavelength, is displayed in Figure 4.8. As before, the output plane is at $z = -5\ \mathrm{mm}$. Due to a change of the Bragg angle, the observed diffraction efficiency depends on the size of the area in the output plane which is accounted for. For example, this could be the entrance pupil of the objective. From the lowest to the topmost curve, the radius of the considered area is increased. The lowest curve is the result of calculating the DE by summation of the intensity within the aperture $NA = n_0 \sin\theta = 0.75$, or in the circle in the output plane described by $\rho = \sqrt{x^2 + y^2} \leq 2.89\,\mathrm{mm}$.

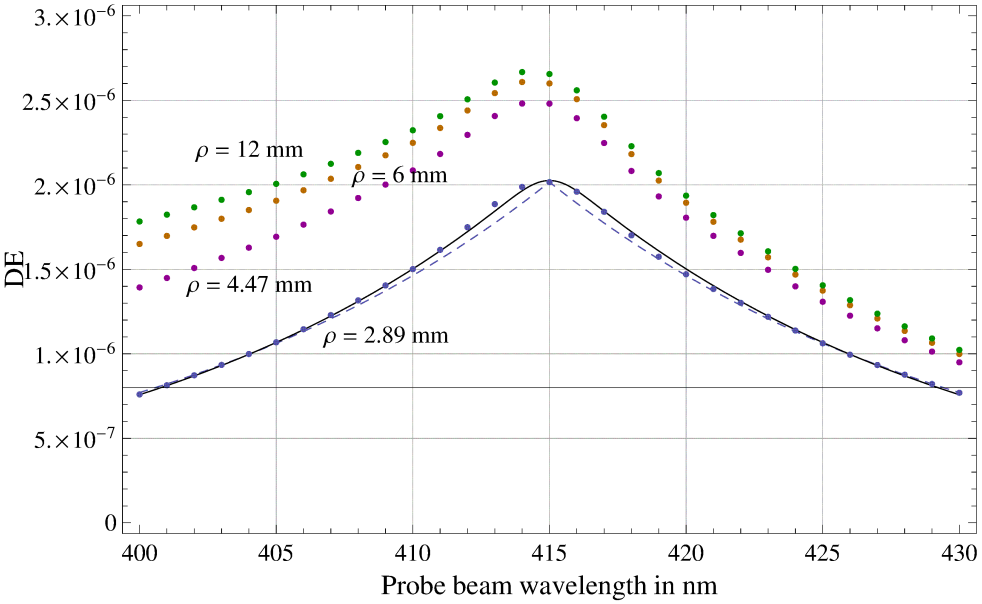

Figure 4.8: Calculated diffraction efficiency over readout wavelength, for different radii ρ of the aperture in the output plane, from bottom to top: $\rho = 2.89$, 4.47, 6, and 12 mm. Parameters: $NA = 0.75$, write wavelength $\lambda = 415\,\mathrm{nm}$; refractive index $n_0 = 1.5$ and index contrast $\Delta n = 0.001$.

The FWHM of this curve is 22 nm. An estimation confirms this: A uniform diffraction grating of N periods yields its first zero for destructive interference if the wavelength is shifted away from resonance by $\Delta\lambda = \lambda/N$. The Fourier transform of the $1/(1+u^2)$ profile of the micrograting (with $u = z/z_R$) has a FWHM of $\ln(2)$, so $\Delta\lambda = (\ln(2)/\pi)\lambda/N$. The micrograting has a FWHM of $N = 2z_R/\Lambda = 3.8$ grating periods, which yields a FWHM of 24 nm. This agrees well with the above result.

To describe the line shape and to understand the spectral characteristics of the grating, two curves are fitted. The dashed curve is given by

$$\mathrm{DE}(\lambda) = 2.02 \cdot 10^{-6} \exp\left(-\frac{|\lambda - \lambda_0|}{15.6}\right) . \tag{4.21}$$

The solid curve is given by the convolution of $\exp(-|\lambda-\lambda_0|/v)$ with a narrow Gaussian $\exp(-(\lambda-\lambda_0)^2/w_G^2)$, where v and w_G are fitting parameters, which yields

$$\begin{aligned} DE(\lambda) = a \exp\left(\frac{w_G^2}{4v^2} - \frac{(\lambda-\lambda_0)}{v}\right) \mathrm{erfc}\left[\frac{w_G}{2v} - \frac{\lambda-\lambda_0}{w_G}\right] \\ + a \exp\left(\frac{w_G^2}{4v^2} + \frac{(\lambda-\lambda_0)}{v}\right) \mathrm{erfc}\left[\frac{w_G}{2v} + \frac{\lambda-\lambda_0}{w_G}\right] , \end{aligned} \tag{4.22}$$

where $a = 1.056 \cdot 10^{-6}$, $v = 14.62$, $w_G = 1.098$ and $\mathrm{erfc}(z) = 1 - \mathrm{erf}(z)$. It includes the influence of the Gaussian shape of the hologram in the lateral dimensions. A larger aperture, for $\rho \leq 4.47\,\mathrm{mm}$, gives the second curve. This radius corresponds to the critical angle (41.8°) of total reflection at the boundary between air and the material ($n_0 = 1.5$). The third curve is for $\rho = 6\,\mathrm{mm}$, whereas the topmost curve is the result of integrating the intensity over the circle $\rho \leq 12\,\mathrm{mm}$.

At wavelengths below 415 nm, the observed diffraction efficiency largely depends on the size of the aperture in the output plane, while for $\lambda > \lambda_0$ there is smaller change. To explain this result, Figure 4.9 shows the intensity over x in the output plane at shorter (a) and larger wavelengths (b). At larger wavelengths, the output is basically a depleted Gaussian beam of the same size. At shorter wavelengths, the maximum of the intensity occurs at a larger radius. Consequently, a substantial part of the intensity is blocked by the confined radius of the aperture in the output plane.

This effect can be explained by a change of the Bragg angle. At correct replay wavelength $\lambda = \lambda_0$, the diffraction process can be imagined as perpendicularly incident waves on a reflection grating, which are reflected in the opposite direction. At a different replay wavelength, consider a part of the microholographic grating where the incident wave hits the grating in the perpendicular direction.

Bragg's law is $2\Lambda \sin\alpha = \lambda/n_0$, where $\Lambda = \lambda_0/(2n_0)$ is the grating period, which yields $\sin\alpha = \lambda/\lambda_0$. Now, if the readout wavelength is below λ_0, Bragg diffraction is allowed for some $\alpha < 90°$. This new Bragg angle is included in the spread of the high-NA beam in wavevector space, and the angular selectivity of a resolution-limited micrograting is broad because of its small size. In contrast, with larger gratings due to saturation of the material, which are described in the next chapter, this effect is much weaker.

As a result, part of the diffracted light propagates in direction $90° - \alpha$, leading to a maximum of the intensity at some larger radius. For larger wavelengths, the situation is different because there is no allowed Bragg angle ($\sin\alpha \leq 1$). Consequently, the deviation from the Bragg condition leads to a depleted diffracted beam which maintains its Gaussian shape.

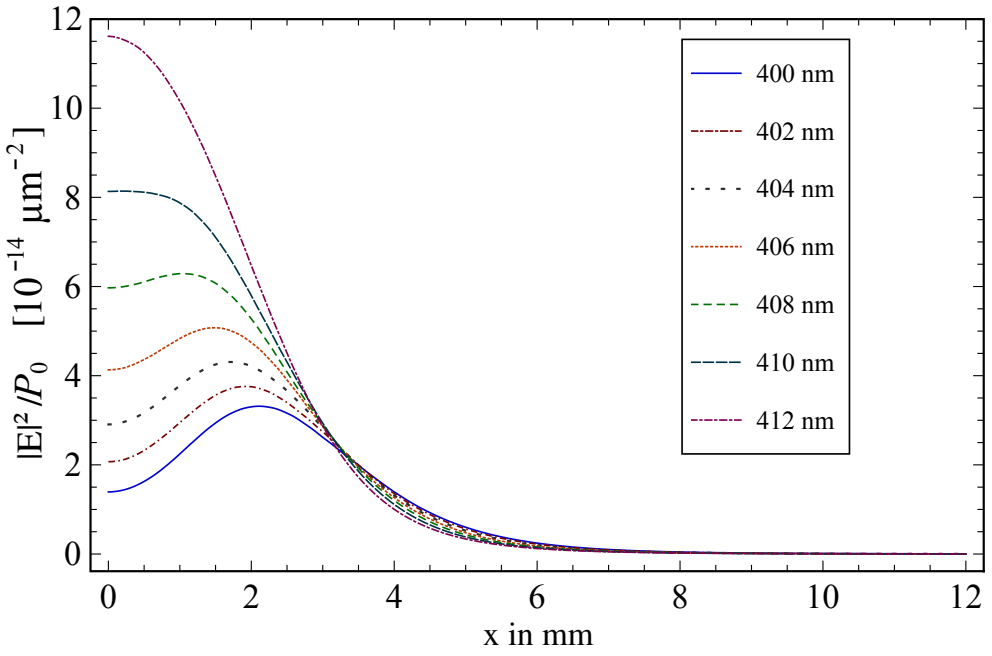

(a) Wavelength below 415 nm

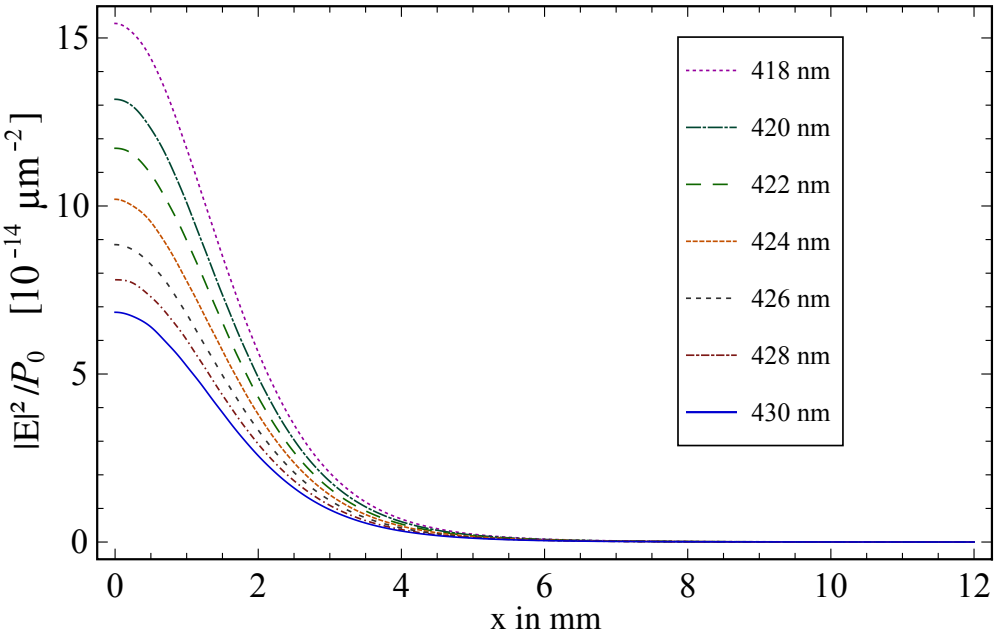

(b) Wavelength above 415 nm

Figure 4.9: Intensity over x in the output plane at $z = -5\,\mathrm{mm}$ (rotation symmetric), normalized by the input power P_0, at different readout wavelengths. Beam parameters: write wavelength $\lambda = 415\,\mathrm{nm}$ and $NA = 0.75$. Refractive index is $n_0 = 1.5$ and index contrast is $\Delta n = 0.001$.

4.4 Conclusion

In this chapter, a simplified method for modeling the diffraction efficiency (DE) of microgratings was introduced. It uses a Taylor expansion of the Green function in the diffraction integral. With this method, microgratings written in a linear recording medium with a blue laser at 405 nm and NA of 0.75 and with a green laser at 532 nm and NA of 0.6 were modeled.

The diffraction efficiency of microgratings as a function of both lateral and longitudinal scan position was analyzed. The lateral FWHM is 247 nm and 430 nm for the blue and green wavelength, respectively. This is consistent with experimental data. The longitudinal FWHM is 1.0 µm for the blue and 2.33 µm for the green laser. With an index contrast of $\Delta n = 0.001$, the DE of such a grating is of the order of 10^{-6}.

In order to evaluate the impact of the numerical aperture of the focusing objective, the DE of microgratings with different NA was modeled and shown to agree with the estimate NA^{-4}.

To assess the potential of wavelength multiplexing, the DE of the strongly localized microgratings in dependence on the readout wavelength was calculated. This also provides an insight into the diffraction effects which take place. For smaller wavelengths, the broad angular selectivity of the small micrograting supports a diffraction angle below 90°, which leads to a slightly larger DE.

Results show a FWHM of 22 nm for recording with a 400-nm-band laser. According to this and considering the practically usable spectral range of blue-sensitive media (400 to 430 nm), wavelength multiplexing is hardly feasible with resolution-limited microgratings.

Saturation of the response of the recording material changes the shape and dimensions of the microgratings and also their structure. The resulting gratings are much larger. This changes the way they diffract the focused light, including the spacial and spectral selectivity, which is analyzed in the next chapter.

5 Effects of saturation on the selectivity of microgratings

Resolution-limited microgratings in linear recording media, as in Chapter 4, can only be produced without saturation of the material. Confocal recording of microgratings by using highly focused beams however yields a strongly localized region of exposure. In the focal region, the exposure fluence reaches a maximum value of the order of $1\,\mathrm{J/cm^2}$ [35]. This has some consequences for the photopolymer which is used as a storage material. The micrograting will be broader, larger and the structure may disappear in the central part of the grating.

The influence of saturation on the grating structure and thus on the diffraction efficiency at readout and on the localization of the gratings ought to be understood on a theoretical basis which accompanies and explains the experimental results. In this chapter, the effects of saturation on microgratings and their diffraction properties are analyzed. A key question is the performance of microgratings when Bragg mismatch plays the most important role in the diffraction process.

The chapter begins with an introduction on saturation in photopolymers and the effects on microgratings. Subsequently, the method for mathematical modeling of the diffraction by these gratings is described. With this method, the effective width and depth of the enlarged gratings, which is enabled by the Bragg selectivity of the volumetric grating structure, is determined. With some simplifications, different effects on microgratings are analyzed, including a depleted contrast at the focus. The diffraction efficiency of the gratings with varied readout beam position (scanning) is evaluated. The aim is to determine the effective size of gratings at typical exposure densities. Spectral properties and wavelength selectivity of the gratings are examined as well.

5.1 Micrograting in saturating photopolymers

5.1.1 Saturation of a photopolymer

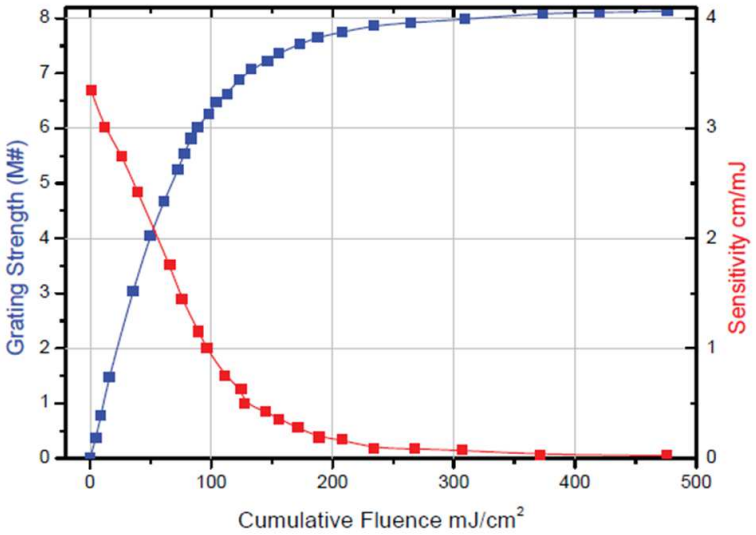

Figure 5.1: Saturation in a blue-sensitive STX Aprilis E-Type photopolymer (with a thickness of 300 µm), source: STX Aprilis - data sheet

The reaction of the holographic recording material on exposure fluence is known mostly for extended, volume-type plane-wave gratings [8]. In Figure 5.1 the saturation characteristic of a photosensitive material is displayed. The $M/\#$ (M number) was introduced by Mok et. al. in [76]. It is a parameter which describes the dynamic range performance of a holographic memory system. If the number of the recorded holograms, M, is sufficiently large, the equalized diffraction efficiency (DE) of each of these gratings is given by

$$DE = \left(\frac{M/\#}{M}\right)^2 . \tag{5.1}$$

This characteristic is useful for multiplexing. Exposure time schedules which enable equalized DE of a sequence of gratings can be derived as described in [76]. Multilayer optical data storage and exposure schedules are covered in Chapter 6.

The processes in the material during holographic recording depend on a set of parameters including the grating period, the size and the shape of the interaction volume. The DE, determined by the $M/\#$ as in (5.1), is a quantity resulting from the whole

grating. However, the spatial variation of the index contrast of a hologram in such a material can be expected to follow a similar characteristic. At typical fluences of the order of $1\mathrm{J/cm^2}$ the grating strength has clearly reached a saturation level.

A comprehensive analysis of photopolymer systems for microholographic data storage can be found in [36]. To characterize various photosensitive materials and to record gratings at a broad range of exposure energies, a media tester system was built. The objective lenses have a lower numerical aperture than for microholographic data storage in order to get comparable results for different material types. The recording beams have a diameter of 6 µm and a Rayleigh length of 200 µm [8], producing larger reflection gratings than the high-NA gratings for data storage at the resolution limit, which are described in this work and in [77] and were recorded in experiments [35]. Saturation effects are shown by the results, as the gratings get larger in their diameter when the exposure energy density is increased. The results obtained in microholographic data storage at high NA may be different as the dynamic processes in the material depend on the size of the interaction volume.

The real effects which occur along with the recording of such localized microholographic gratings are not known in detail. The parameters of each material change with each developed version and they are influenced by the temperature conditions during shipment which may cause unwanted material effects [8, ch. 3]. However, some conclusions can be drawn from measured results which show the interaction of the readout beam with the grating structure in several different recording procedures.

Saturation of the material can change the shape, the size and the structure of microgratings. The intensity of the light used for recording extends over a broad range, reaching high values near the center compared to low values a few hundred nanometers away from it. In the center of each microgratings, the counterpropagating beams are expected to exploit the local concentration of monomers. Altogether, the index contrast depends nonlinearly on the intensity of the recording beams. As a result, the grating contrast can approach an upper limit, which is reached within a larger volume.

Due to saturation, the grating structure becomes much larger than the resolution-limited size of the exposed region. In the central region of the grating, where the

index contrast is the highest, the amplitude of the $\lambda/2$-periodic component of the grating is expected to be reduced. Thermal effects near the focus due to the absorption of light can cause chain transfer. This stops the polymerization process of some of the molecules and leads to shorter polymer chains. Chain transfer leads to shorter polymer chains [37, 40]. Their greater mobility leads to local dissolving of the grating [7, p. 118]. The central part of the grating may lose its structure.

Experimental work [7, 8] so far has not been able to reveal the real structure and the dimensions of microholographic gratings written in a photosensitive material as at any time the whole grating contributes to the readout signal. The apparent size of a hologram shown by readout is basically determined by two effects. Obviously it is limited by the overlap of the intensity with the index contrast. Bragg diffraction contributes to the resolution as a result of the phase structure of the grating and the readout beam. When the focus of the beam is shifted, the DE is depleted due to a phase mismatch. During readout, gratings with saturation appear much smaller than they actually are, which is the benefit of holography.

The actual size of the gratings is critical for the achievable storage capacity in microholographic data storage. If a track of data is recorded, the in-track spacing must be sufficiently large. Orlic et. al. recorded gratings in stop-and-go mode, which means that the photopolymer sample is moved to a position and stopped for the duration of exposure [35]. When the gratings are recorded with a lateral pitch of 350 nm instead of 500 nm, the exposed regions overlap and the polymerization is not constrained to each storage location. Adjacent gratings consume the monomers, which reduces the index contrast. This leads to a drop in the readout efficiency. Having a slightly larger spot size and a larger depth, gratings with saturation overlap whereas resolution-limited gratings should not.

When stored in multiple layers, gratings with saturation can overlap as well. As S. Frohmann has shown in his thesis [8], tracks of microgratings recorded in subsequent layers share the photochemical resources of the material even if they are separated by an interlayer spacing of about ten micrometers. This indicates that the gratings might really be that large in depth.

5.1.2 Mathematical model of saturation

In order to investigate gratings in a saturating photopolymer, an appropriate mathematical model for local saturation effects is needed which correctly describes the recorded gratings. Holographic gratings are stored by polymerization which changes the refractive index locally. Polymerization typically is a second-order chemical reaction in which two monomers or short chains are involved [78]. In this case, the consumption of monomers can be described by

$$-\frac{\partial[M]}{\partial t} = \kappa[M]^2 \,, \tag{5.2}$$

and the part of the monomers which have polymerized until some time t is found by integration of (5.2):

$$\frac{[M](0) - [M](t)}{[M](0)} = \frac{\kappa t[M](0)}{1 + \kappa t[M](0)} \,. \tag{5.3}$$

This general model for polymerization describes the concept of saturation. As time passes, polymerization slows down and finally reaches an upper limit. In a photosensitive polymer material, several processes occur during recording and grating formation. Polymerization can be subdivided into three main steps [38]. The first one is initiation, namely the production of free radicals which bind to monomers. It is followed by chain growth, referred to as propagation, and finally stopped by termination.

Kelly et. al. [38] developed a nonlocal diffusion model under nonideal kinetic conditions in photosensitive polymer materials for holographic recording. A quadratic relationship between the rate of polymerization and the monomer concentration accurately explained the results of their experiments. This is based on a primary termination mechanism, in which a polymer chain with an active tip reacts with a free radical, which stops the chain growth. This mechanism is expected to dominate in dry polymer materials when the movement of polymer chains is constrained. The polymerization rate is derived from the diffusion equation [38, 79] as

$$-\frac{\partial[M]}{\partial t} = D\,\frac{\partial^2[M]}{\partial x^2} + Q\,[1 + V\cos(Kx)]^{\gamma}\,[M]^{\beta} \,, \tag{5.4}$$

where $D(x,t)$ is the diffusion constant, V is the visibility of the holographic grating, and Q is a parameter combining material properties and the intensity of light during recording. The exponent γ has a value between 0.5 and 1.5. The parameter β can

have a range of values, the particular cases $\beta = 1$ (bimolecular termination) and $\beta = 2$ (primary termination) are compared in [38]. The results of the material model show a saturation function over exposure energy which is akin to (5.3).

For analysis of the diffraction of gratings by far-field integrals a simple model is needed which describes the gratings. If the increase of the grating index contrast over time follows a saturation function as in [38], the index contrast in terms of the intensity during recording can be expected to follow a similar function. The normalized saturation function f used in this thesis is

$$f_\alpha(\gamma(\vec{r})) = \frac{(1+\alpha)\gamma(\vec{r})}{1+\alpha\,\gamma(\vec{r})}\,, \tag{5.5}$$

where $\gamma(\vec{r}) = I(\vec{r})/I_{\max}$ is the normalized intensity of the light used for recording, namely the interference structure. The saturation can be adjusted by varying the parameter $\alpha > 0$. When $\alpha = 0$, the saturation is turned off. Figure 5.2 shows the function at various saturation parameters. The function has two fixed points $f_\alpha(0) = 0$ and $f_\alpha(1) = 1$, whereas $f_\alpha(\gamma) > \gamma$ if both $0 < \gamma < 1$ and $\alpha > 0$.

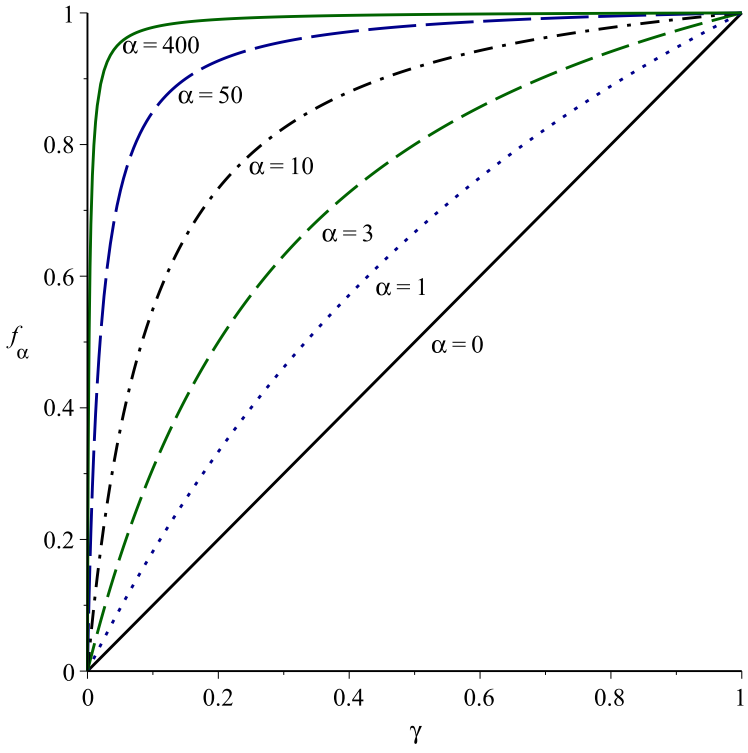

Figure 5.2: The saturation function, for several values of the saturation parameter α.

The saturation function in (5.5) changes the profile of the micrograting. The longitudinal form of the micrograting stays the same but its full width at half maximum along the z axis is increased by a factor $\sqrt{1+\alpha}$ which is easily shown using

$$\frac{I(0,0,z)}{I_{\max}} = \frac{1}{1+z^2/z_R^2} \ . \tag{5.6}$$

5.1.3 Characteristics of micrograting in a saturating recording medium

The structure and the index contrast of a micrograting change when saturation of the photopolymer takes place. In linear recording, gratings have a cosine-squared pattern with zeroes and maxima. Saturation of the material modifies the gratings, which affects the index contrast as well as the grating structure. The gratings are larger than the resolution-limited gratings in Chapter 4. By just applying the saturation function on the envelope together with the cosine-squared pattern, the index contrast will stay near its maximum over an extended region. As in this mathematical model zeroes remain zeroes, the grating index contrast itself can be described by the envelope.

The normalized index contrast of a grating with saturation is shown in Figure 5.3. The picture at the top displays the lateral cross section on a line through the focus if the saturation parameter is $\alpha = 400$ (FWHM of 10.3 µm along z). The Gaussian is broadened to a flat-top profile.

Not only the index contrast is saturated, but the cosine-squared pattern is modified as well. This is shown in the longitudinal cross section at the bottom of Figure 5.3. Theoretically the zeroes remain zeroes, but the grooves become narrow. Components with grating periods $\lambda/(2m)$ with $m = 2,3,\ldots$ appear, which share the index contrast. They are expected not to contribute to diffraction but the first harmonic with grating period $\lambda/2$ is depleted. This effect is the strongest in the focal region where the intensity is the highest.

These grooves would require a finer resolution than a linearly recorded reflection grating, which the material usually does not provide. Most likely they will be washed away, as in any illuminated area polymer chains start to grow and may extend into the darker areas. The nonlocal response induces a cut-off of higher spatial frequencies in the grating [80], which reduces the grating contrast in the focal region.

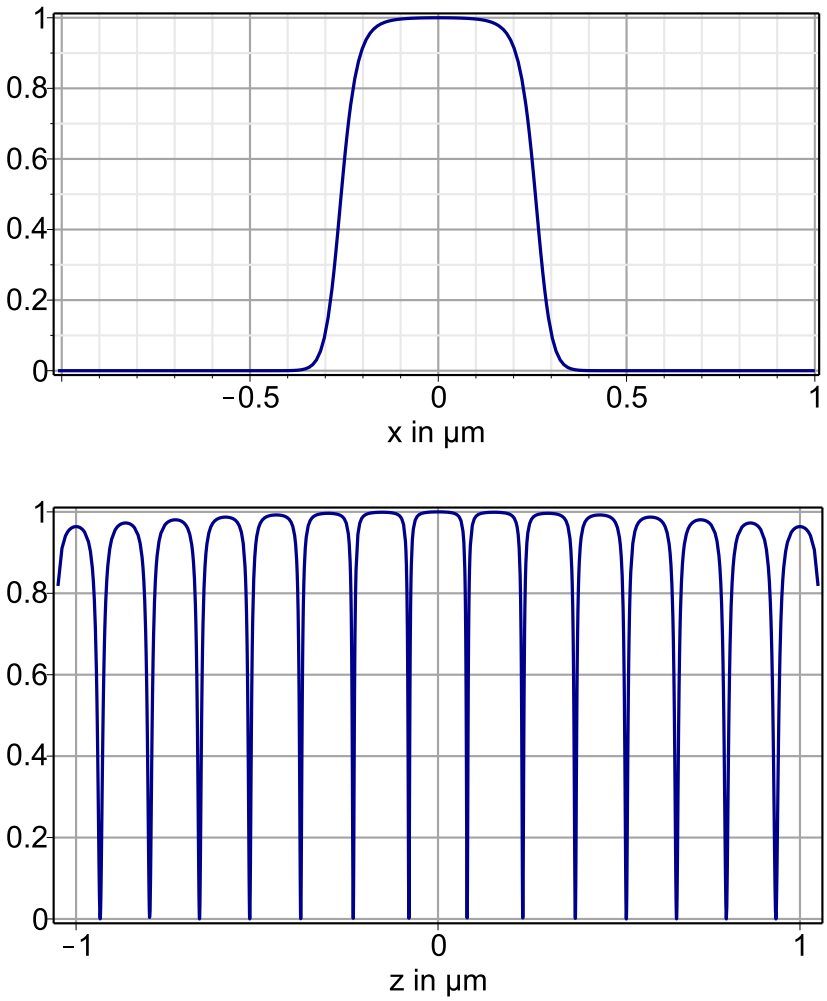

Figure 5.3: Normalized index contrast of a grating with saturation in lateral direction (top) and along the optical axis (bottom), with $NA = 0.75$ and wavelength 405 nm. The saturation parameter is $\alpha = 400$, which yields a FWHM of 10.3 µm along z.

To correctly describe the modification of the grating structure due to saturation, the nonlocal-response diffusion model by Sheridan et. al. [80] would be necessary, which describes the processes in the material. It includes a diffusion constant and a nonlocal response function which describes the nonlocal effect of the monomer concentration and requires more information about material properties, which are not available. A full material model is beyond the scope of this thesis which describes the diffraction effects of micrograting. An estimation of the modified grating structure is given in Section 5.5 in the context of micrograting with depleted contrast at the focus.

5.2 Modeling the diffraction efficiency of gratings with saturation

Resolution-limited microgratings recorded in a linear medium are the size of a high-NA laser spot. Bragg diffraction of these volumetrically localized gratings does not play a role as the reconstructed signal is a result of the intensity overlap. With NA of 0.75 and a wavelength of 405 nm, the diffraction efficiency (DE) has a FWHM of 0.1486 µm in the lateral dimension and a depth of 1 µm, as found in Chapter 4. Due to saturation, gratings are much larger than resolution-limited gratings and Bragg diffraction becomes an essential part of the diffraction process.

The purpose of this section is to calculate the DE of largely extended gratings due to saturation. The full profile of the gratings cannot be integrated symbolically. However, the characteristics of these gratings can be explored with similar grating profiles, so that the integrals can be solved in the lateral dimensions. The most relevant characteristics of gratings with saturation are included. The longitudinal profile of the gratings is retained, but the lateral profile is simplified so as to keep the calculation feasible. The resulting integrals can be computed in the way described in Chapter 4.

On the longitudinal axis, the grating index contrast exactly follows the saturation function f. Saturation using (5.5) extends the grating in the longitudinal dimension. On the z axis, the local index contrast is

$$\Delta n \left(1 + \frac{z^2}{z_R^2(1+\alpha)}\right)^{-1} . \tag{5.7}$$

As the solid line in Figure 5.4a shows, the part of the grating near the focus is broader than the spot size and has a flat-top profile. Farther away, this profile gradually turns into a Gaussian, as in the cross section at $z = 3\,\mu\text{m}$ of a grating with $\alpha = 400$ and a depth (FWHM) of 10.3 µm (Figure 5.4b). A few Rayleigh lengths beyond the focus, if $|z| \gtrsim 2\,z_R\sqrt{1+\alpha}$, the grating approaches the Gaussian shape of the laser spot.

For the purpose of a comparative and profound analysis of the diffraction characteristics of gratings with saturation, three different functions are used for the lateral profile. The first is the broadest profile, which puts the most emphasis on the curved grating structure. It is followed by a profile as narrow as the incident beams (dot-dashed

in Figure 5.4), which is narrower in the focal region than the grating with saturation. The third profile (dashed line in Figure 5.4) has the same FWHM as the grating with saturation, which is between the other two profiles.

With a variation of index profiles, the influence of the grating dimensions on the diffraction effects can be modeled considering a range of grating properties. The calculated results describing the diffraction efficiency in terms of the focus position of the readout beam and the wavelength selectivity also give answers on intermediate grating profiles which may exist in reality.

The first index contrast profile has a constant value along the lateral dimensions. The grating is as wide as possible, highly emphasizing the curved structure of the grating. The refractive index contrast yields

$$n_1(\vec{r}) = \Delta n \left(1 + \frac{z^2}{z_R^2(1+\alpha)}\right)^{-1} . \tag{5.8}$$

In the second version, the grating index contrast takes the same Gaussian form as the resolution-limited grating. Near the focus, this grating is as narrow as the resolution-limited grating. A few Rayleigh lengths away from the focus, it gradually approaches the profile of the grating with saturation. It is described by

$$n_2(\vec{r}) = \Delta n \left(1 + \frac{z^2}{z_R^2(1+\alpha)}\right)^{-1} \exp\left(-2\frac{x^2+y^2}{w(z)^2}\right) . \tag{5.9}$$

This grating profile is the narrowest of the three, while the first version is the broadest. The third profile is a Gaussian which has the same FWHM as the grating with saturation. This is the best way found to imitate the grating by a simpler function. The index contrast yields

$$n_3(\vec{r}) = \Delta n \left(1 + \frac{z^2}{z_R^2(1+\alpha)}\right)^{-1} \exp\left(-2\frac{x^2+y^2}{w(z)^2}\,\frac{\ln(2)}{\ln(2+\alpha w_0^2/w(z)^2)}\right) . \tag{5.10}$$

These two grating profiles are shown in Figure 5.4. The dash-dot line describes the grating with n_2, and the third grating profile (dashed line) intersects the saturated grating profile (solid line) at $1/2$.

In the next section, the DE in terms of the dependence on the lateral and longitudinal position of the readout beam is modeled in order to determine the spatial selectivity of the gratings. The wavelength selectivity of gratings with saturation is calculated in Section 5.4.

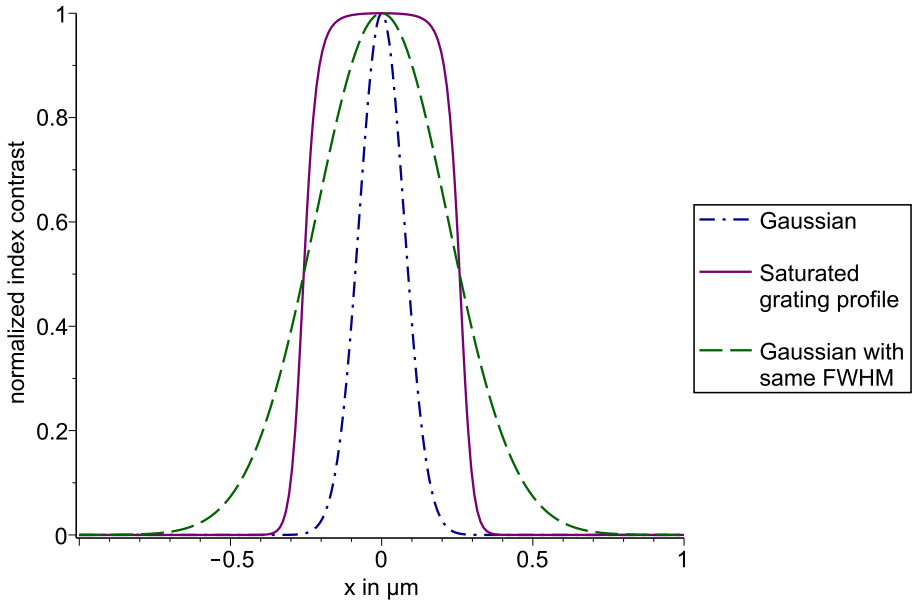

(a) Index contrast at $z = 0$, normalized

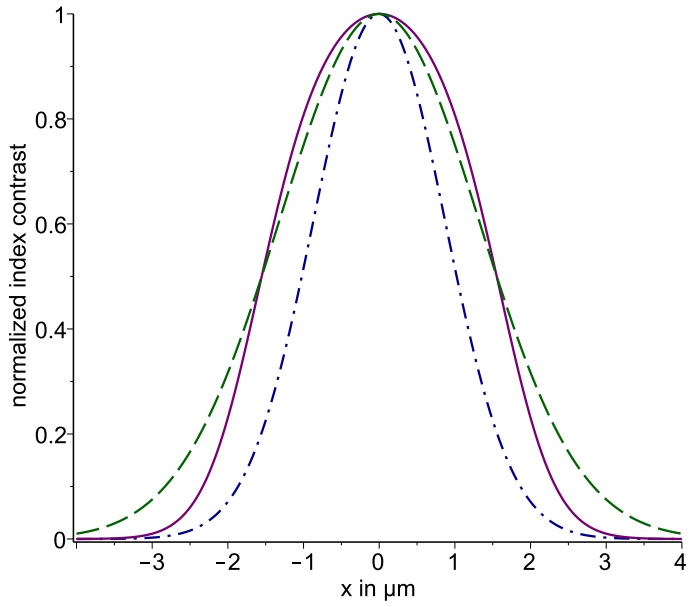

(b) Index contrast at $z = 3\,\mu\mathrm{m}$, normalized

Figure 5.4: Normalized index contrast of a grating with saturation in the lateral direction, with a Gaussian profile (n_2) and with the same FWHM (n_3). The saturation parameter is $\alpha = 400$, which yields a FWHM of 10.3 µm along z. The incident beam has NA of 0.75 and a wavelength of 405 nm.

5.3 Readout of microgratings in a saturating medium

In this section, the effective size of the microgratings with saturation is determined. They are recorded at a wavelength of 405 nm with $NA = 0.75$. The recording material has a refractive index of $n_0 = 1.5$ and the maximum index contrast is $\Delta n = 0.001$. Due to the larger dimensions of microgratings enabled by saturation, the diffraction efficiency (DE) for confocal readout increases with larger saturation parameter α, which is shown in Figure 5.5. The grating with the narrow profile, n_2, yields the lower DE, as displayed by the dot-dashed line. The results for the profile with the same FWHM as the grating with saturation, n_3, are described by the solid line. The DE can be described by the empirical polynomial functions

$$DE^{(2)} = 4.47 \cdot 10^{-6} + 2.66 \cdot 10^{-6}\alpha - 4.38 \cdot 10^{-10}\alpha^2 \,, \tag{5.11}$$

$$DE^{(3)} = 1.41 \cdot 10^{-5} + 3.96 \cdot 10^{-6}\alpha - 7.50 \cdot 10^{-10}\alpha^2 \,. \tag{5.12}$$

Even at strong saturation, $\alpha \lesssim 1000$, the DE is of the order of 10^{-3}. At typical recording energy densities with $\alpha \approx 100$, the DE is $4 \cdot 10^{-4}$, so an index contrast of 0.01 is required to achieve a DE of 10^{-2}, which is needed to suppress material noise [8].

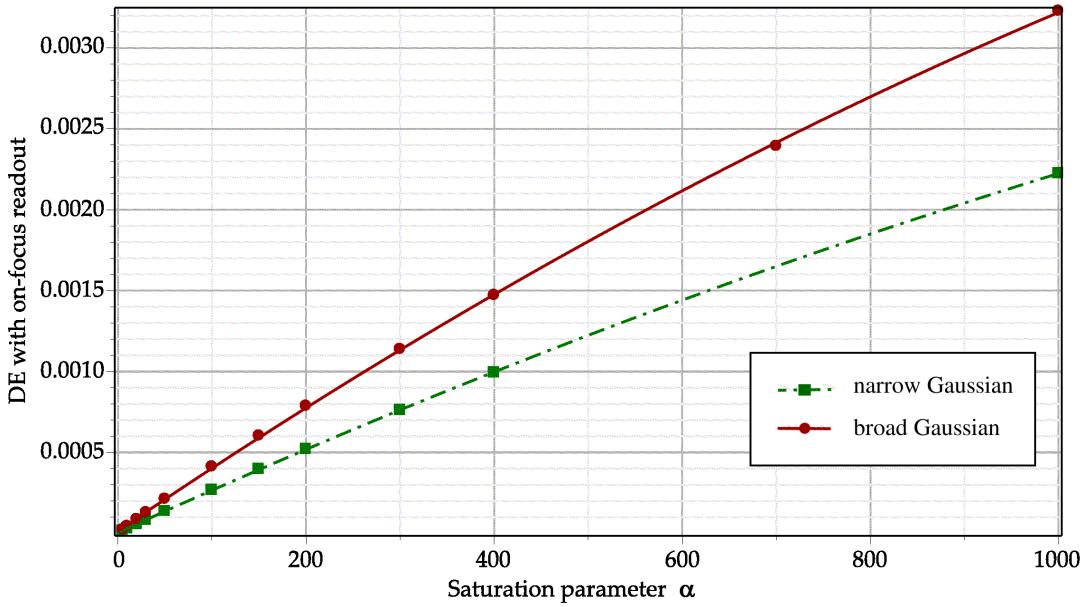

Figure 5.5: Diffraction efficiency of microgratings in terms of the saturation parameter α.

5.3.1 Laterally resolved diffraction efficiency

In order to determine the effective lateral size of the microgratings, the second and third index profiles are investigated. The diffraction efficiency (DE) is calculated depending on the lateral focus position of the readout beam where the focus is at $x = \Delta x$ and $z = 0$. As shown in Figure 5.6 at various saturation parameters for the second grating profile, the normalized DE excellently follows a Gaussian function

$$\exp\left(-\frac{\Delta x^2}{x_{\text{eff}}^2}\right) .$$

This is found for both grating profiles. For each saturation parameter α, the effective lateral size x_{eff} is determined by fitting the Gaussian function to the DE.

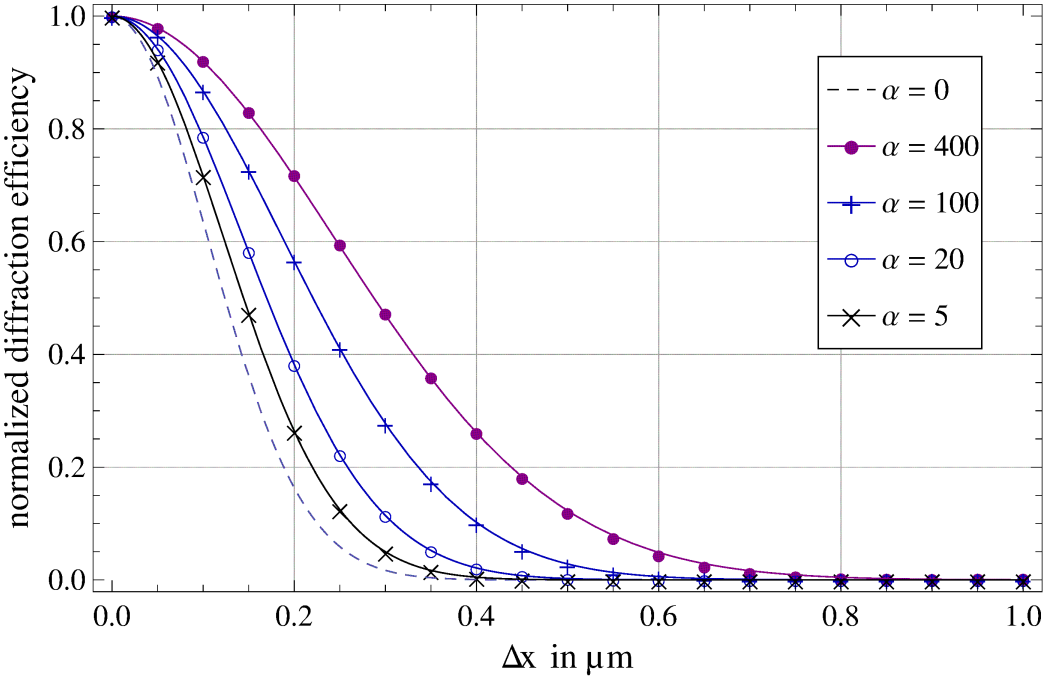

Figure 5.6: DE for lateral scanning at several parameters of saturation. Grating index profile in the lateral dimensions described by n_2, (5.9).

Figure 5.7 shows the effective lateral size x_{eff} of the gratings in terms of the saturation parameter. The points are results of the computation of the diffraction integral, whereas the lines connecting the points are empirical curves. The dashed line belongs to the second grating profile, which has the same width as the recording beams.

The solid line describes the grating (3) with an index contrast which has the same FWHM as the grating with saturation. As the grating (3) has a broader profile, the curved wavefronts are more pronounced, which enhances its Bragg selectivity. This leads to a smaller effective width.

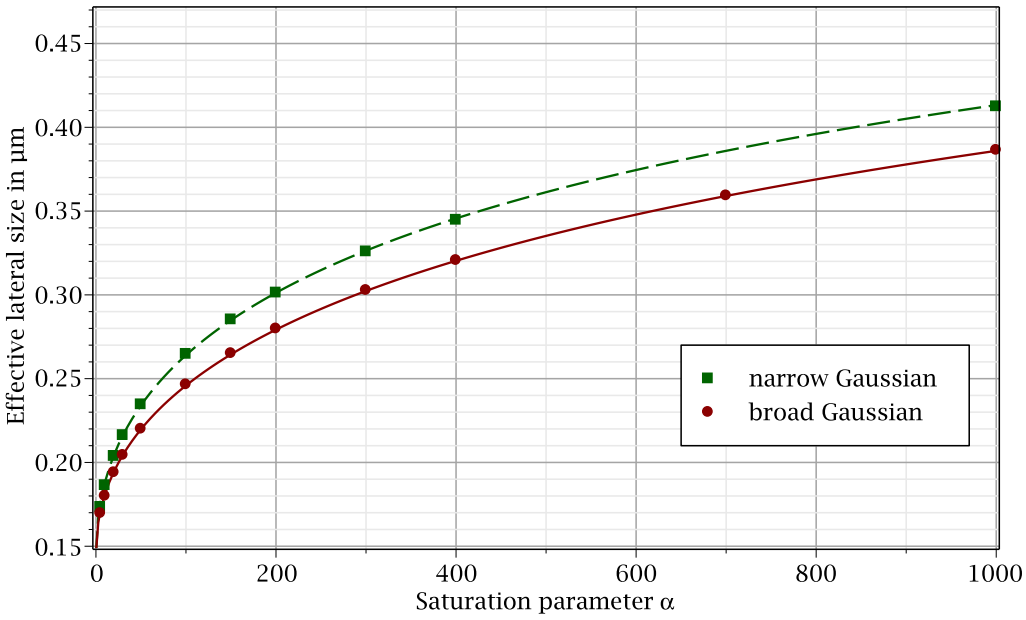

Figure 5.7: Effective width of gratings in terms of saturation parameter. Index profile: narrow Gaussian with n_2 (dashed), wide with n_3 (solid line). Details in the text.

The effective width of the grating type (2) can be described by the empirical function

$$x_{\text{eff}}^{(2)} = 0.785\,\mu\text{m} - \frac{0.639\,\mu\text{m}}{1 + 0.0228\sqrt{\alpha}}\,.$$

For grating type (3), the effective width yields

$$x_{\text{eff}}^{(3)} = 0.826\,\mu\text{m} - \frac{0.680\,\mu\text{m}}{1 + 0.0173\sqrt{\alpha}}\,.$$

The results of the two gratings are similar. The upper limit of about 800 nm effective width of the gratings shows the high Bragg selectivity of these microgratings. In the experimental setup a confocal filter blocks scattered light and diffracted light emerging from adjacent data layers. This filter may reduce the diffraction of the micrograting which is being addressed by the readout beam when the beam focus is shifted, further improving the selectivity. To calculate this is not feasible with the diffraction integral.

5.3.2 Longitudinally resolved diffraction efficiency

In order to determine the effective depth of the gratings, the diffraction efficiency is calculated depending on the focus position along the optical axis. The first grating profile to be calculated has a constant refractive index contrast in the lateral dimensions as in (5.8). As the readout beam is scanned over the focus of the grating in the longitudinal direction, the normalized diffraction efficiency changes according to a Lorentzian function, namely

$$\frac{1}{1+\frac{\Delta z^2}{z_{\text{eff}}^2}} \,. \tag{5.13}$$

The FWHM of the DE rises with the degree of saturation α as shown by the blue dashed line in Figure 5.8. An empirical function which fits the data is

$$2\,z_{\text{eff}}^{(1)} = 5.00\,\mu\text{m} - \frac{4.56\,\mu\text{m}}{1+0.00926\sqrt{\alpha}} \,.$$

When the index contrast is constant in x and y, the grating is larger in the lateral dimensions than the grating with saturation. When the focus of the readout beam is moved away from the focus of the grating, the DE decreases due to Bragg dephasing. With high contrast in the curved fringes, the Bragg selectivity of this grating is enhanced and the effective size is the smallest of the three gratings.

The second lateral profile of the index contrast has the same Gaussian form as the Gaussian beam, as in (5.9). At the focus, the grating is as narrow as the resolution-limited grating. In the focal region, the curved outer parts of the fringes receive a lower index contrast than the grating with saturation. The green line in Figure 5.8 shows the FWHM of the DE in terms of α. As the grating depth becomes larger with saturation, the diffracted light emerges largely from the parts near the optical axis, which leads to a large effective depth. An empirical function which fits the data is

$$2\,z_{\text{eff}}^{(2)} = 7.41\,\mu\text{m} - \frac{6.38\,\mu\text{m}}{1+0.0233\sqrt{\alpha}} \,.$$

In the range of $0 < \alpha < 1000$, this grating has an effective depth of up to 3.8 µm. As the curved outer parts of the grating fringes have a low index contrast, they do not contribute much to the diffraction process. Hence, this grating profile has a lower Bragg selectivity.

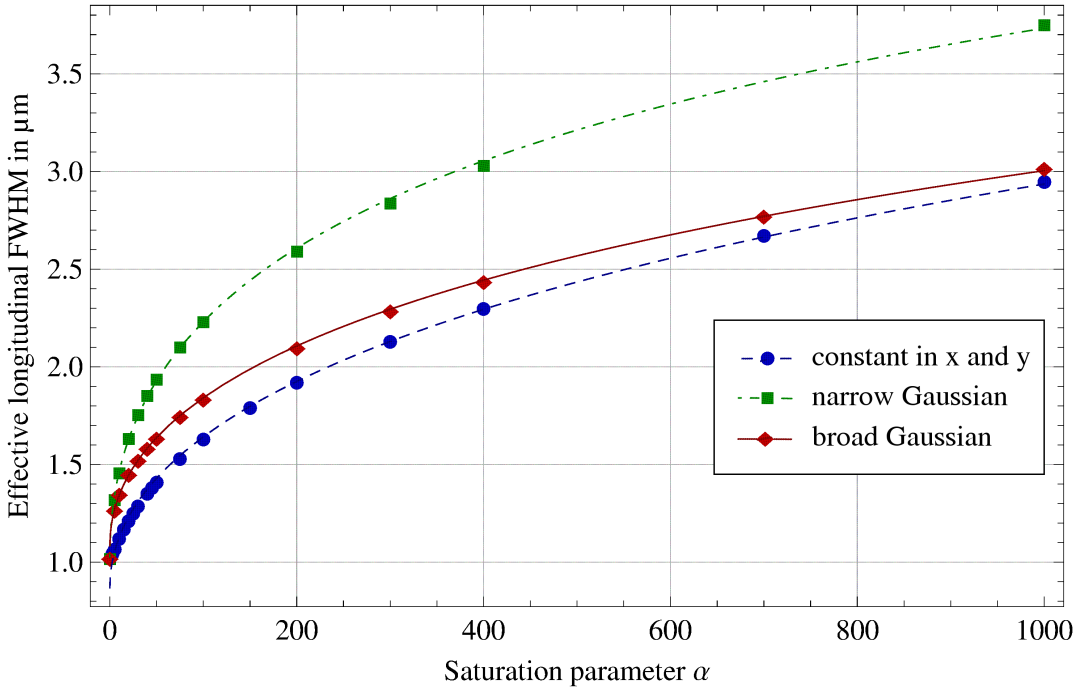

Figure 5.8: FWHM of the diffraction efficiency for longitudinal scanning in terms of the saturation parameter α, shown for three lateral index profiles: calculated data as points, empirical fit function as lines.

The third grating index profile, (5.10), with the same width as the grating with saturation, yields the results depicted by the red, solid line in Figure 5.8, described by

$$2\,z_{\text{eff}}^{(3)} = 7.69\,\mu\text{m} - \frac{6.60\,\mu\text{m}}{1 + 0.0130\sqrt{\alpha}}\,.$$

In the broad range of $0 < \alpha < 1000$, the grating of the third type has a smaller effective depth (up to 3 µm) than the second grating with the narrow profile. In the focal region, the third grating is broader and the curved grating fringes enhance the Bragg selectivity. When the readout beam is moved in the z direction, the wavefronts of the incident light match the grating only in its central part. The diffraction efficiency is reduced, which leads to a smaller effective size of the grating. The effective depth $2\,z_{\text{eff}}^{(3)}$ is only slightly larger than the depth $2\,z_{\text{eff}}^{(1)}$ of the grating with constant index contrast in x and y as the focused readout beam is much narrower than these gratings.

The contribution of Bragg selectivity to the results is large, as for example at $\alpha = 400$ with a grating depth (FWHM) of 10.3 µm, the effective depth obtained by readout is below 3 µm.

5.4 Wavelength selectivity of microgratings with saturation

As thick holograms have narrow peaks of the DE in the spectral domain, several spectral channels can be used for parallel recording and readout. The potential of wavelength multiplexing for microholographic data storage with moderate NA has preliminary been investigated in [32]. Strongly localized microgratings only have a moderate spectral selectivity in consequence of the small effective number of grating fringes. Experiments which could investigate the wavelength selectivity are challenging and would require a highly sensitive spectrometer.

Resolution-limited microgratings in a linear medium are analyzed in Section 4.3 and the results have been published in [77]. Calculation of the diffraction efficiency as a function of the readout wavelength with the diffraction integral yields a FWHM of 22 nm, with $NA = 0.75$. Within the practically usable spectral range of blue-sensitive storage materials (400 to 430 nm), wavelength multiplexing is hardly feasible with resolution-limited microgratings.

Due to their larger size, microgratings with saturation can exhibit an enhanced wavelength selectivity compared to resolution-limited gratings. The reason is that dephasing by a shift in the readout wavelength causes the diffraction efficiency (DE) to drop. As more grating fringes contribute to the diffracted field, off-Bragg effects set in at a smaller wavelength shift and the spectral FWHM of the diffraction efficiency is smaller.

The spectral properties of these gratings are analyzed in this section. For this purpose, the DE is calculated based on the profile n_2 (5.9), a Gaussian as narrow as the recording beams. The results are compared to the results produced by the third lateral profile (5.10), a Gaussian profile with the same FWHM as the grating with saturation. The grating with saturation has a flat-top profile in the focal region and more and more turns into a Gaussian in the outer regions. With only slight modifications of the shape of the grating near the focus, the wavelength selectivity predicted by these calculations should be near to the values for the grating with saturation.

Figure 5.9 shows the DE in terms of the dependence on the readout wavelength, when the grating has a profile described by (5.10) and $\alpha = 70$. Two curves are displayed. The DE can be described by the empirical fit function (4.22), which was used for

resolution-limited gratings in Section 4.3. When the diffracted light is clipped at an angle of $\arcsin(NA/n_0) = 30°$, the points follow the dashed line. With a clipping angle of 41.8°, which is the angle of total reflection at the boundary of the material with $n_0 = 1.5$ to air, the obtained diffraction efficiency is slightly larger ($\times$ and solid line).

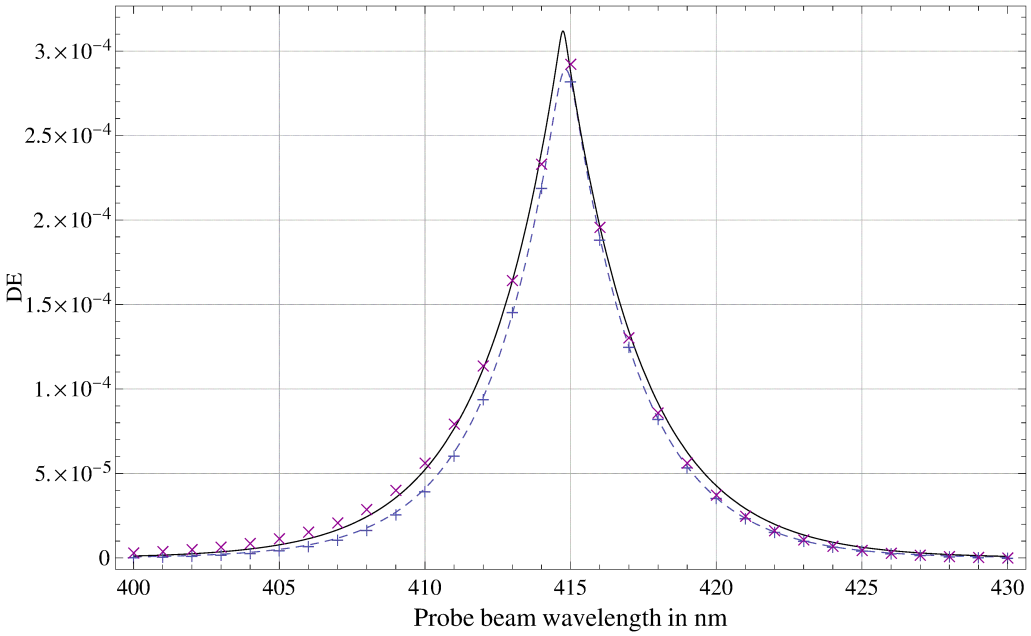

Figure 5.9: DE over wavelength for a micrograting with Gaussian profile with the width of the grating with saturation (n_3) and saturation parameter $\alpha = 70$. With $+$: clipping at the angle of $\arcsin(NA/n_0)$, $\times$: clipping at the angle of total reflection 41.8° at the boundary between air and the material ($n_0 = 1.5$).

The FWHM of the resulting curve is 3.8 nm. The curve is nearly symmetric, whereas resolution-limited microgratings as described in Chapter 4 yield an asymmetric spectral curve. At shorter readout wavelengths, the small dimensions of these gratings allow smaller Bragg angles which are part of the spectrum of the incident beam. The maximum of the intensity of the diffracted light occurs at a larger radius, which enlarges the diffraction efficiency at smaller wavelengths.

For gratings with moderate saturation ($\alpha = 70$), the limiting of the aperture has little effect on the measured DE. The larger dimensions of the gratings improve the angular selectivity and constrain the diffraction angles which can be returned. The shift of the Bragg angle is less profound, shown by the similarity of the two curves.

Figure 5.10 shows the spectral FWHM of the gratings in terms of the saturation parameter α. The green squares show the FWHM for the second grating profile, and the circles describe the results for the third profile. The spectral FWHM of the gratings with the broader profile is larger than with the narrow profile, which can be explained by the broader grating near the focus.

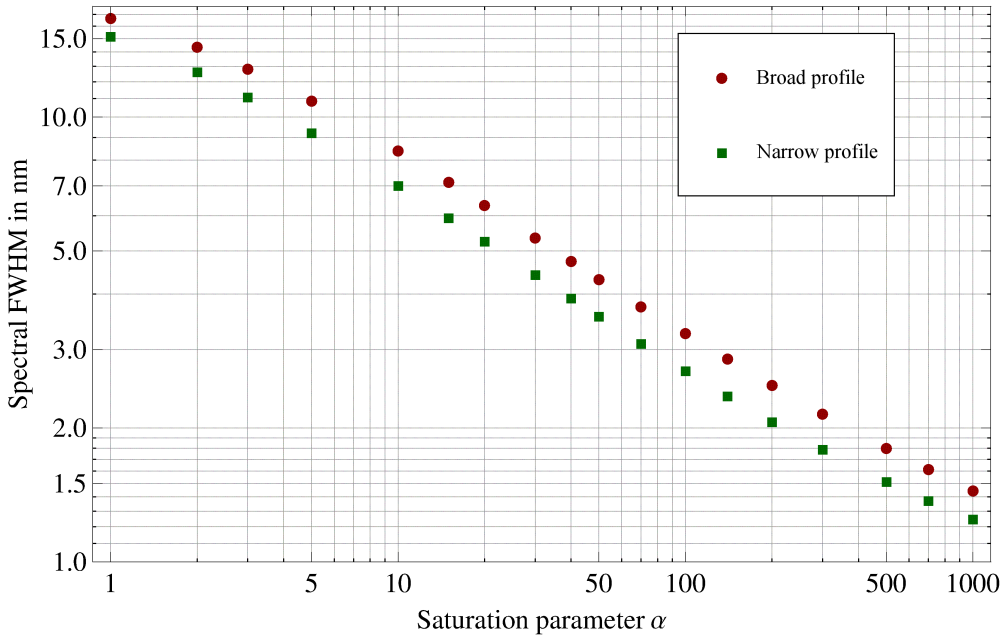

Figure 5.10: Spectral FWHM of the microgratings as a function of the saturation parameter α. Green squares: grating profile n_2 (5.9), red circles: n_3 (5.10).

A larger saturation α enhances the spectral selectivity of the gratings. For $\alpha \geq 400$ the FWHM is below 2 nm. Both grating profiles yield better selectivity when α grows as the depth of the gratings increases, which makes a major contribution to the spectral selectivity. With a weak saturation effect, such as α between 3 and 5, the gratings have a FWHM of 11 nm, which is half the spectral width of the resolution-limited grating.

Moderate saturation levels α between 100 and 300 at typical recording exposure densities of 2 to 6 J/cm^2 yield a spectral FWHM between 2 nm and 3 nm. This may enable wavelength multiplexing unless the storage of several gratings at the same position is impeded by saturation. Shrinkage of the recording material should be cared of as a shrinkage of 1 % corresponds to a wavelength shift of 4 nm.

5.5 Micrograting with depleted contrast near the focus

Several effects can cause depletion of the grating structure near the focus. When micrograting are recorded in a saturating material with unequal intensities of the recording beams, the contrast of the grating structure in the focal region is reduced. This section is focused on the DE, the spatial and spectral selectivity of these micrograting.

Thermal effects due to absorption of the strongly focused light during recording can cause chain transfer, which leads to shorter polymer chains with greater mobility and dissolving of the grating near the focus [7,37]. Saturation of the material is expected to modify the structure of micrograting, which causes a depletion of the $\lambda/2$ component near the focus, as described in detail in Subsection 5.5.2. As the grating profiles are similar in these cases, these micrograting are expected to yield similar results.

5.5.1 Unequal intensities of the recording beams

In the optical setup for microholographic data storage, a retroreflector unit is used which mirrors the beam in itself. After having passed through the photosensitive material, the intensity of the mirrored beam may be reduced. Unequal intensities add a slowly varying component to the exposure pattern which forms the grating.

Without saturation, this part, which has no grating structure, can be neglected when diffraction effects are considered. Resolution-limited micrograting will not influence the phase structure of the incident light as the index contrast Δn is small. With saturation, the raised index contrast within an extended region may introduce a small phase shift to the incident light during readout. Moderate saturation ($\alpha \lesssim 400$) with a grating depth of up to 10 µm and $\Delta n = 0.001$ yields a phase shift of 10 nm at most.

In a saturating photopolymer however, the remaining range of the grating is reduced by the constant component. The minima in the grating structure are above zero. Consequently the grating fringes fade away in the focal region where the exposure is highest. As an example, the intensity ratio of the beams is set to 2:1, which is realistic [8], while the saturation parameter of the grating is 400. To illustrate this, the grating structure is shown in Figure 5.11. In the center of the grating the structure has a low contrast.

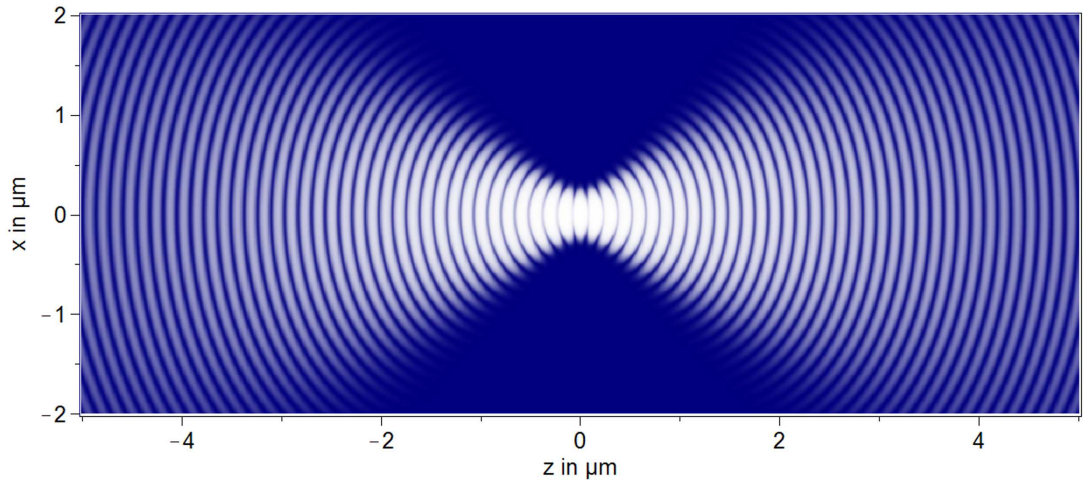

(a) Micrograting view in x and z.

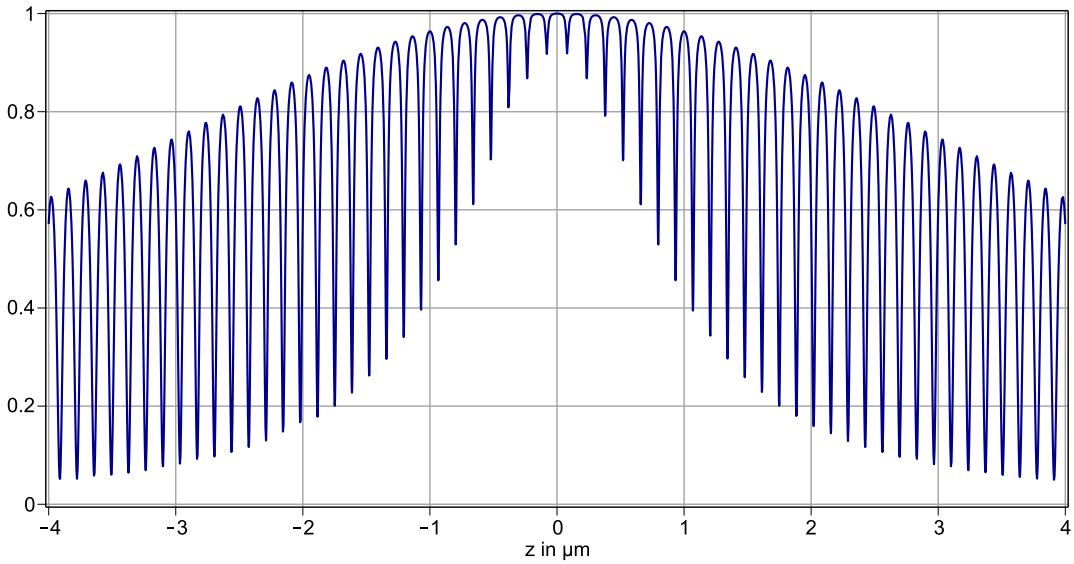

(b) Normalized index contrast of the grating on the longitudinal axis.

Figure 5.11: Micrograting recorded with an intensity ratio of 2:1 in a material with saturation $\alpha = 400$ (FWHM 10.3 µm in z), with $NA = 0.75$ and wavelength 405 nm.

The normalized interference structure during recording of a grating with an intensity ratio of 2:1 is described by

$$\begin{aligned}\frac{I(\vec{r})}{I_{\max}} &= \frac{2}{2\sqrt{2}+3}\left|e^{i\phi(\vec{r})}+\frac{1}{\sqrt{2}}e^{-i\phi(\vec{r})}\right|^2\frac{\widehat{I}(\vec{r})}{I_{\max}} \\ &= \left(1-\frac{4\sqrt{2}}{2\sqrt{2}+3}\sin^2(\phi(\vec{r}))\right)\frac{\widehat{I}(\vec{r})}{I_{\max}}\,,\end{aligned} \tag{5.14}$$

where $\widehat{I}(\vec{r})$ is the envelope of the intensity and $\phi(\vec{r})$ is the phase of the reference beam. From the maxima to the minima, the intensity drops to 3 %. In a recording material with the saturation function f_α as in (5.5), the contrast of the grating structure yields

$$n_{2:1}(\vec{r}) = \Delta n\, f_\alpha\left(\frac{\widehat{I}(\vec{r})}{I_{\max}}\right) - \Delta n\, f_\alpha\left(\frac{\widehat{I}(\vec{r})}{I_{\max}}\left(1-\frac{4\sqrt{2}}{2\sqrt{2}+3}\right)\right)\,, \tag{5.15}$$

where the envelope of the normalized intensity is

$$\frac{\widehat{I}(\vec{r})}{I_{\max}} = \frac{w(0)^2}{w(z)^2}\exp\left(-2\frac{x^2+y^2}{w(z)^2}\right)\,. \tag{5.16}$$

A grating with a lower contrast at the center can have different properties concerning the DE and the localization. Recorded with unequal intensities, the grating has a particular profile: At the focus the contrast of the grating structure has a local minimum, if $\alpha > 5.83$. Away from the focus, the minimum rises and gradually disappears. As the focused readout beam scans over such a grating, the effective width is larger compared to the gratings with equal intensities in Sections 5.3 and 5.4.

The lateral profile of the grating structure is shown in Figure 5.12 at $\alpha = 400$. At the focal plane $z = 0$, the contrast of the rotation-symmetric grating structure $n_{2:1}(\vec{r})$ (dashed line) has a maximum reaching 0.71 and a local minimum at the center. In the focal region, the index contrast is depleted to about 8 %. The profile at $z = 1\,\mu\mathrm{m}$ shows that away from the focus, the minimum of the contrast slowly disappears.

A similar change of the grating structure can be expected by thermal effects due to the absorption of the highly focused light. Shorter polymer chains transfer their active part to free monomers and stop growing. Their greater mobility leads to a depletion of the contrast of the grating near the focus [7, p. 118]. A comprehensive material model including multicomponent diffusion, viscosity and thermal effects is yet to be found [40]. These aspects influence each other, for example the viscosity of a photopolymer depends on its temperature, which in turn accelerates the diffusion.

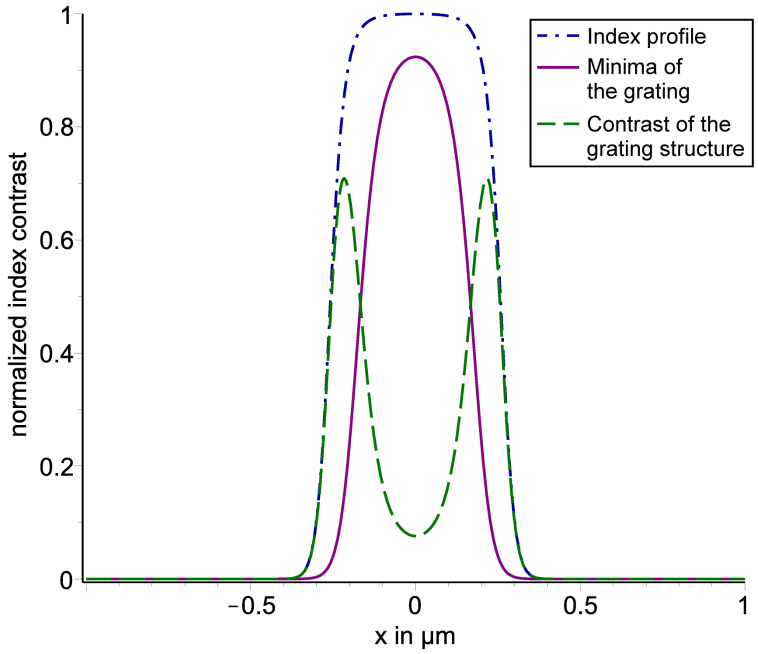

(a) At $z = 0$

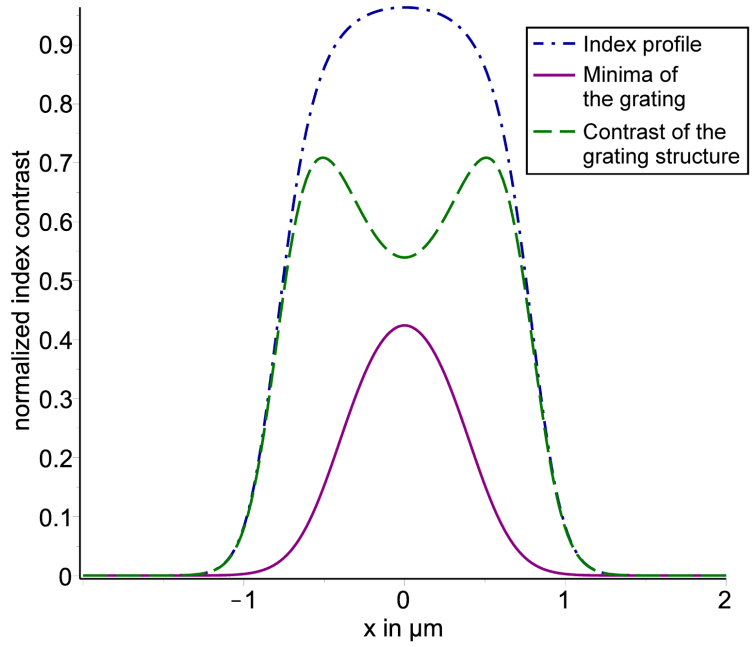

(b) At $z = 1\,\mu\mathrm{m}$

Figure 5.12: Normalized index contrast of a grating with 2:1 intensity ratio: Level of maxima (dash-dot), level of minima and contrast of grating structure (the difference of the two). Saturation parameter $\alpha = 400$, $NA = 0.75$ and $\lambda = 405\,\mathrm{nm}$.

5.5.2 Modification of the grating structure due to saturation

Not only the index contrast is changed by saturation, but the grating structure is modified as well. Figure 5.13 shows the normalized refractive index along the optical axis as predicted using the saturation function. The maxima of the grating structure are broadened while the minima become thin. At two Rayleigh lengths, the resolution-limited grating (or the exposed intensity pattern) has an index contrast of 0.2 of its maximum value, whereas the contrast of the grating with saturation remains large.

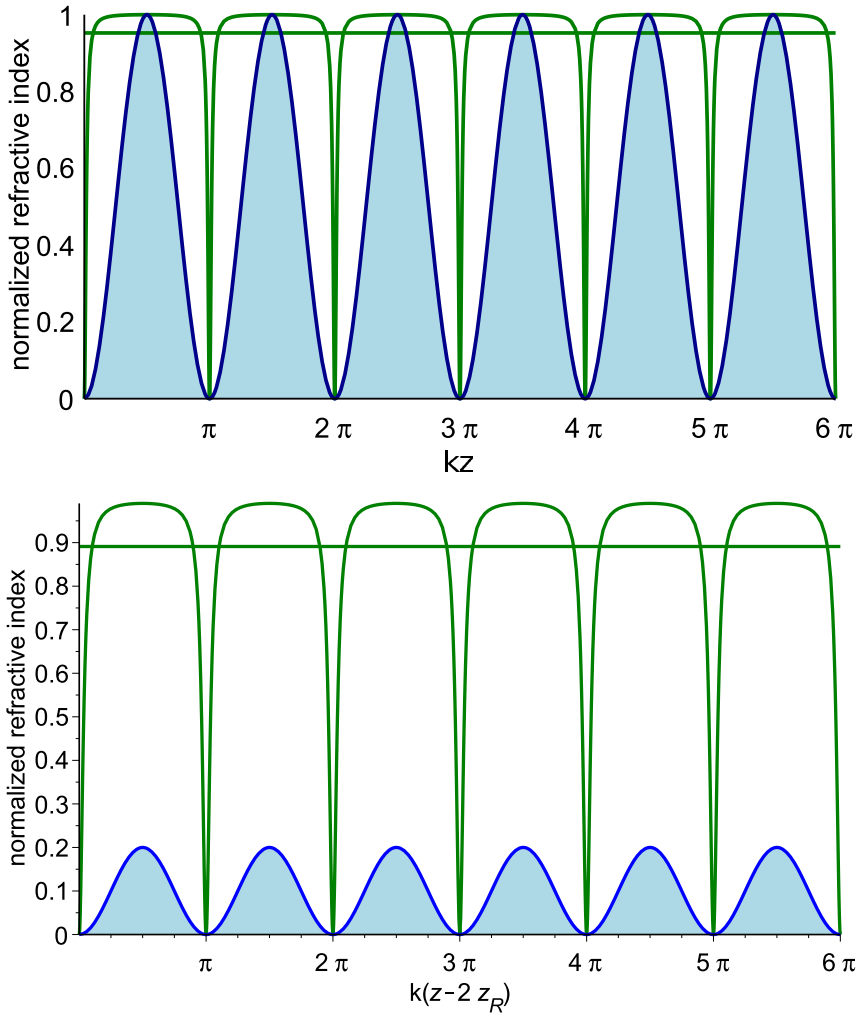

Figure 5.13: Saturated grating structure (with $\alpha = 400$, FWHM $\approx$ 10 µm in z) at the center (top) and at $z = 2\,z_R$ (down). The saturated structure is shown, its average (horizontal line) and the sinusoidal exposure pattern (levels 1 and 0.2). The index contrast is fixed for clarity; precisely it loses 7% from 0 to 6π in the bottom picture.

The diffraction properties of the grating can change due to saturation as the amplitude of the first harmonic with a grating period of $\lambda/2$ is modified. Diffraction is generated mainly by this component, as higher harmonics are not supported in a reflection grating. In addition, higher harmonics are expected to be cut off by the nonlocal material response [80]. A grating model which should be more accurate is developed here. The saturation function f_α with $\gamma(\vec{r}) = I(\vec{r})/I_{\max}$ yields the grating structure

$$f_\alpha(\gamma(\vec{r})) = \frac{(1+\alpha)\gamma(\vec{r})}{1+\alpha\,\gamma(\vec{r})}\ . \tag{5.17}$$

The phase of the grating structure is denoted as $\phi(\vec{r})$. The envelope of the grating varies more slowly than the grating structure itself. In a small region around a point $\vec{r}$, it is taken to be constant. For an approximate one-dimensional representation of the grating structure, a line $\vec{r}+\vec{s}(u)$ is parameterized which is orthogonal to the grating fringes. With the unit vector

$$\frac{\mathrm{d}\vec{s}}{\mathrm{d}u} = \vec{e}_u = \frac{\nabla\phi}{\|\nabla\phi\|}\ , \tag{5.18}$$

the saturated grating structure along this line is written as

$$f_\alpha\left(\gamma\left(\vec{r}+\vec{s}(u)\right)\right) = f_\alpha\left(b\cos^2\left(\phi(\vec{r})+k\cdot u\right)\right)\ , \tag{5.19}$$

where $b = \widehat{I}(\vec{r})/I_{\max}$ is the envelope of the normalized intensity, $k = k_0\,n_0$, and $k_0 = 2\pi/\lambda_0$ is the length of the wave vector in vacuum. The normalized index contrast of the grating is $f_\alpha(b)$. The average of $f_\alpha(b)$, described by horizontal lines in Figure 5.13, is the largest in the focal region and is calculated as

$$\overline{f_\alpha}(b) = \frac{1}{2\pi}\int_0^{2\pi} f_\alpha\left(b\cos^2(u)\right)\mathrm{d}u = \frac{(1+\alpha)(-1+\sqrt{1+\alpha b})}{\alpha\sqrt{1+\alpha b}}\ . \tag{5.20}$$

The nonlocal material response [37, 80] indicates that the grating structure is not the structure predicted using the saturation function given by (5.17). In the illuminated fringe areas polymer chains are initiated. They start to grow away from their initiation point and may extend into the darker regions. This leads to a high-frequency cut-off of the material response. Higher harmonics with grating periods $\lambda/4$ or smaller may be suppressed completely. Considering this effect, the real grating structure may be closer to the following approach.

Assuming that the spatial change of the refractive index is proportional to the consumption of monomers [81], the local average $\overline{f_\alpha}(b)$ approximately corresponds to the

averaged consumption of monomers. If the shorter polymer chains diffuse and the grating partly dissolves, it can be expected that $\overline{f_\alpha}(b)$ stays the same. In addition, it is assumed that the envelope of the grating, described by $f_\alpha(b)$, remains unchanged as well. Finally, if only the $\lambda/2$ component remains, the normalized grating structure yields

$$\frac{\Delta n(\vec{r})}{\Delta n_{\max}} \approx \overline{f_\alpha}\left(\frac{\widehat{I}(\vec{r})}{I_{\max}}\right) + \left(f_\alpha\left(\frac{\widehat{I}(\vec{r})}{I_{\max}}\right) - \overline{f_\alpha}\left(\frac{\widehat{I}(\vec{r})}{I_{\max}}\right)\right)\cos\left(2\phi(\vec{r})\right) \ . \tag{5.21}$$

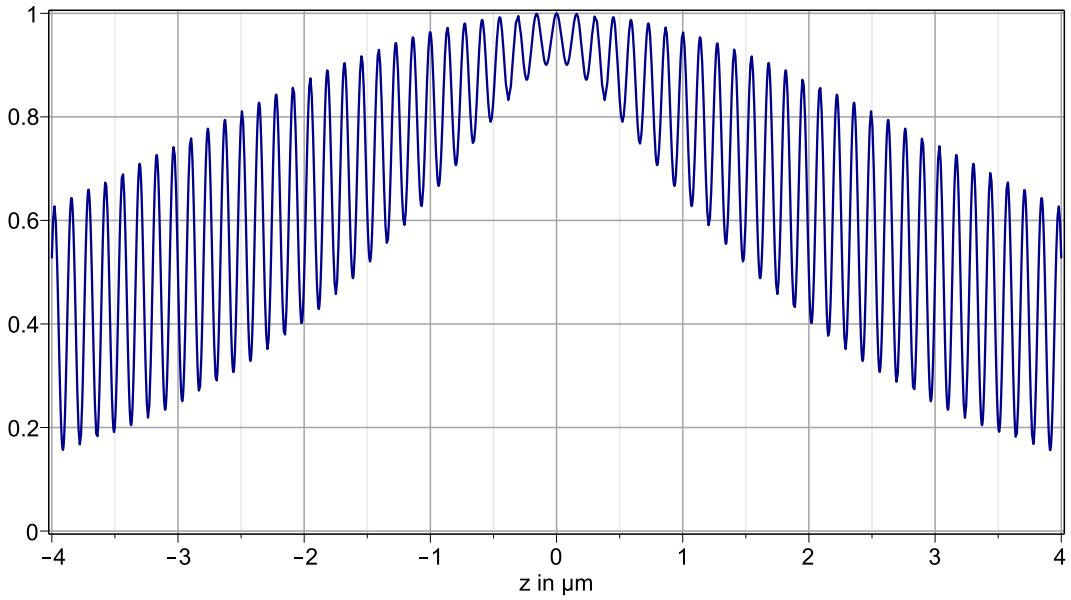

Figure 5.14: Saturated grating structure as described by (5.21), normalized, with $\alpha = 400$.

In the focal region with the highest intensity of light during recording, the saturation effect is the strongest. Figure 5.14 shows the grating structure described by (5.21) on the optical axis with a saturation parameter of $\alpha = 400$. This grating resembles the grating with an intensity ratio of 2:1 in Figure 5.11. The lateral profile of the $\lambda/2$ component is displayed in Figure 5.15. At the focus ($z = 0$) it has a local minimum which slowly disappears with larger distance from the focus.

The similarity of the profiles with an intensity ratio of 2:1 to the profiles described here clearly indicates that the diffraction effects, the localization and the wavelength selectivity of both grating types are similar. Therefore, the analysis of the diffraction by microgratings with an intensity ratio of 2:1 on the following pages is sufficient.

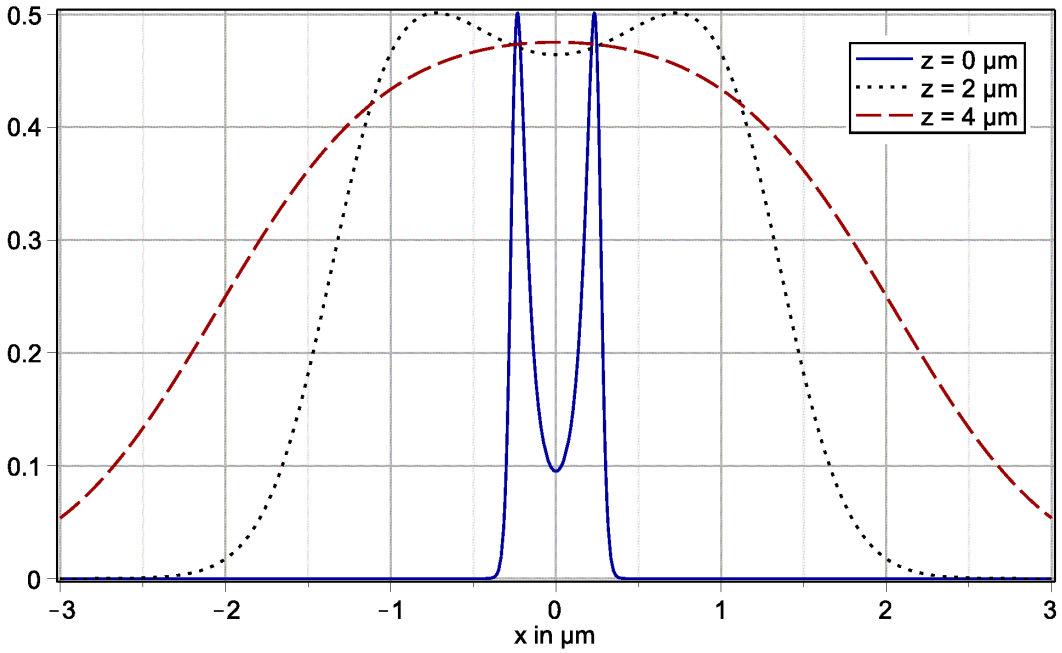

Figure 5.15: Lateral profiles of the grating-structure contrast as described by (5.21) at three z positions, with $\alpha = 400$.

5.5.3 Modeling gratings recorded with unequal intensities

This subsection is focused on gratings which are recorded with an intensity ratio of 2:1, when the intensity of the reflected beam returning from the retroreflector unit is half the intensity of the incident beam. To compute the DE of these gratings, the grating profiles are represented by similar grating profiles composed of Gaussian functions.

The resulting integrals are solved as described in Chapter 4. With this method, the DE for confocal readout, the lateral and the longitudinal selectivity of the gratings are analyzed. The section ends with the wavelength selectivity of these gratings.

The normalized contrast of the grating structure $n_{2:1}(\vec{r})/\Delta n$ is given by (5.15), which is the difference between the maxima and the minima of the grating structure. The envelope of the maxima is described by

$$f_\alpha\left(\frac{\widehat{I}(\vec{r})}{I_{\max}}\right) \tag{5.22}$$

and the minima of the grating structure are connected by

$$f_\alpha\left(\frac{\widehat{I}(\vec{r})}{I_{\max}}\left(1-\frac{4\sqrt{2}}{2\sqrt{2}+3}\right)\right)\ . \tag{5.23}$$

To calculate the diffraction efficiency of gratings with the same characteristics, two similar profiles are devised which can be integrated in the lateral dimensions. These profiles are the same along the optical axis, whereas the maxima of the second profile are stronger. Comparison of the two results enables an evaluation of the impact of the side peaks of the grating-structure contrast on the selectivity of the grating.

The profile of the maxima (5.22) is replaced by a Gaussian as given in (5.10), which has the same amplitude and FWHM as the grating with saturation recorded with equal intensities:

$$n_{\max}(\vec{r}) = \Delta n\ \left(1+\frac{z^2}{z_R^2(1+\alpha)}\right)^{-1}\exp\left(-2\frac{x^2+y^2}{w(z)^2}\,\frac{\ln(2)}{\ln(2+\alpha w_0^2/w(z)^2)}\right)\ . \tag{5.24}$$

In the next step, the profile of the minima is represented by a Gaussian of the same height and FWHM:

$$\begin{aligned} n_{\min,1}(\vec{r}) &= \Delta n\,\frac{1+\alpha}{\alpha+(17+12\sqrt{2})(1+z^2/z_R^2)}\exp\left(-2\,\frac{x^2+y^2}{w(z)^2}\,\frac{\ln(2)}{w_d^2}\right) \\ \text{with}\quad w_d^2 &= \ln\left(2+\left(17-12\sqrt{2}\right)\frac{\alpha\,w_0^2}{w(z)^2}\right)\ . \end{aligned} \tag{5.25}$$

The second profile gets an extra factor 2 in the Gaussian function to produce stronger maxima of the contrast:

$$n_{\min,2}(\vec{r}) = \Delta n\,\frac{1+\alpha}{\alpha+(17+12\sqrt{2})(1+z^2/z_R^2)}\exp\left(-4\,\frac{x^2+y^2}{w(z)^2}\,\frac{\ln(2)}{w_d^2}\right)\ . \tag{5.26}$$

The two profiles are given by $n_{\max}(\vec{r})-n_{\min,1}(\vec{r})$ and $n_{\max}(\vec{r})-n_{\min,2}(\vec{r})$. Along the optical axis, the contrast of the two profiles is the same as for the grating described by (5.22) and (5.23).

Figure 5.16 shows the lateral profile of the grating at the focus ($z=0\,\mu\text{m}$) and at $z=1\,\mu\text{m}$, with a saturation parameter $\alpha=400$. In black, the $\lambda/2$-component of the normalized index contrast $n_{2:1}(\vec{r})/\Delta n$ is displayed. The two profiles, each composed of two Gaussian functions, are shown by dashed lines. The improved version of the profile has stronger maxima which are closer to the maxima of $n_{2:1}(\vec{r})/\Delta n$. For all of the three profiles, the minimum at the center is the same.

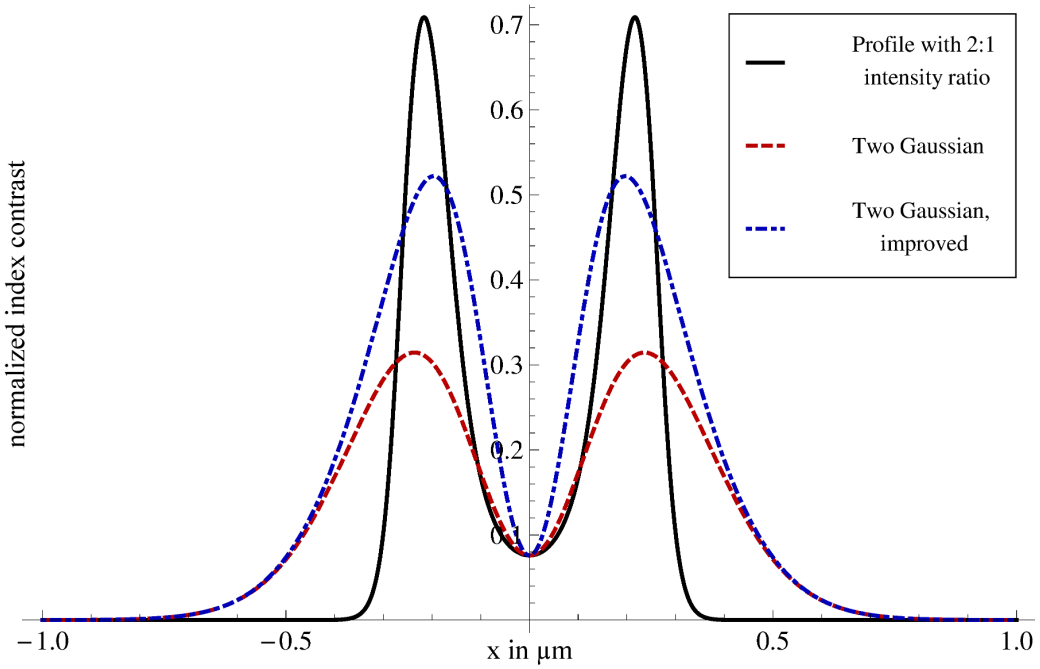

(a) At $z = 0$

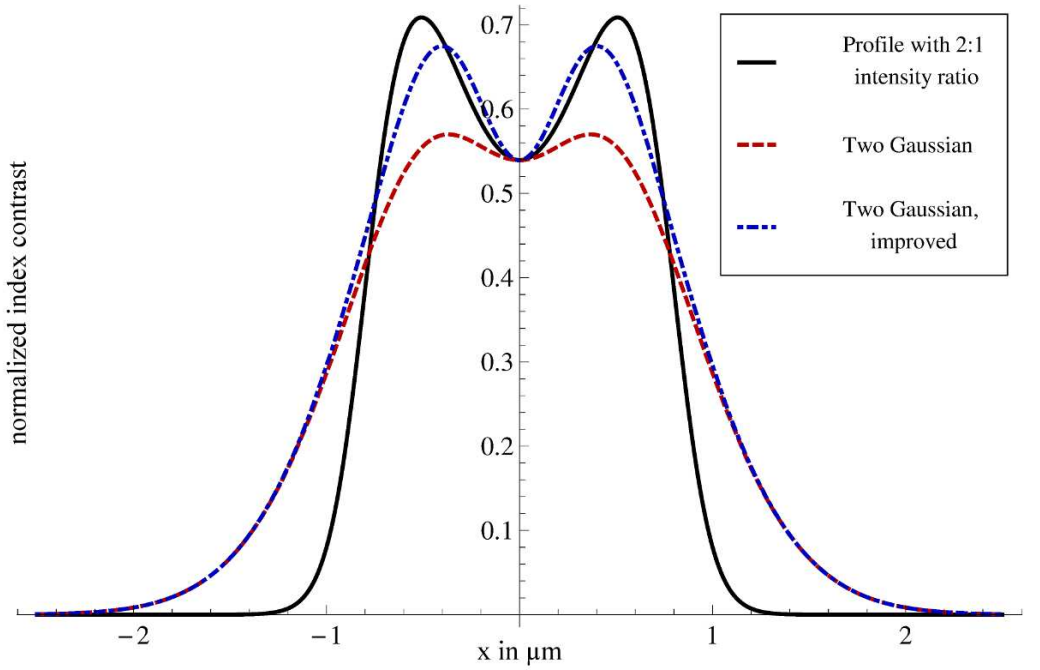

(b) At $z = 1\,\mu\text{m}$

Figure 5.16: Normalized index contrast of a grating with 2:1 intensity ratio and $\alpha = 400$. Two different profiles made of two Gaussian functions are shown.

Diffraction efficiency for confocal readout

Figure 5.17 shows the DE for confocal readout of the two micrograting types in terms of the saturation parameter. It also displays the results for gratings with saturation recorded with equal intensities with the narrow and the broad profile. The two grating profiles for 2:1 intensity ratio yield almost the same DE, which closely resembles the DE of the narrow gratings in Section 5.3. The DE follows the empirical polynomial functions

$$\begin{aligned} DE_{2:1,1}(\alpha) &= 2.35 \cdot 10^{-5} + 2.76 \cdot 10^{-6}\,\alpha - 6.62 \cdot 10^{-10}\,\alpha^2\,, \\ DE_{2:1,2}(\alpha) &= 2.33 \cdot 10^{-5} + 3.04 \cdot 10^{-6}\,\alpha - 7.31 \cdot 10^{-10}\,\alpha^2\,. \end{aligned} \tag{5.27}$$

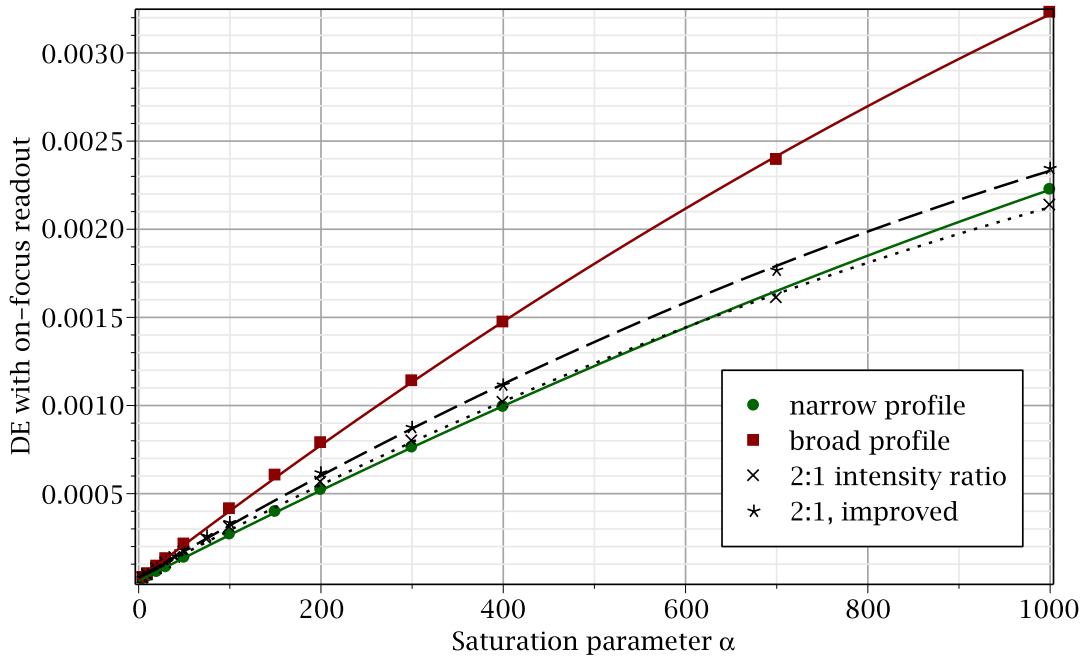

Figure 5.17: DE of microgratings with intensity ratio of 2:1 in terms of the saturation parameter α, together with results for gratings recorded with equal intensities.

As the contrast of the grating structure is reduced by saturation in the focal region, the diffraction efficiency of the gratings is reduced to about 2/3 of the DE of the broad profile. This results in a weaker signal for readout of the stored data. The material consumption of data layers however, which is discussed in Chapter 6, remains unchanged as it depends on the index contrast, not on the structure of the gratings.

Lateral selectivity of the gratings

The effective lateral size of the microgratings with 2:1 intensity ratio is determined by calculating the DE in terms of the lateral focus position Δx. For the second grating profile, given by $n_{\max}(\vec{r}) - n_{\min,2}(\vec{r})$, Figure 5.18 shows the normalized DE at various saturation parameters α. For both profiles, the results can be described by the empirical fit function

$$\left(1 + q^2 \frac{\Delta x^2}{x_0^2}\right) \exp\left(-\frac{\Delta x^2}{x_0^2}\right) ,$$

where q and x_0 are parameters. For larger saturation parameters, the DE deviates from a Gaussian form to a flat-top profile, which is implemented by the parameter q. As α is increased, q grows from zero at $\alpha = 0$ to 0.85 at $\alpha = 1000$. This change is clearly due to the depletion of the grating-structure contrast near the focus which reduces the DE for nearly confocal readout. For larger focal shift, the readout beam overlaps mostly with the gratings at larger distances where the minimum of the grating contrast rises, giving almost the same DE as the broad gratings.

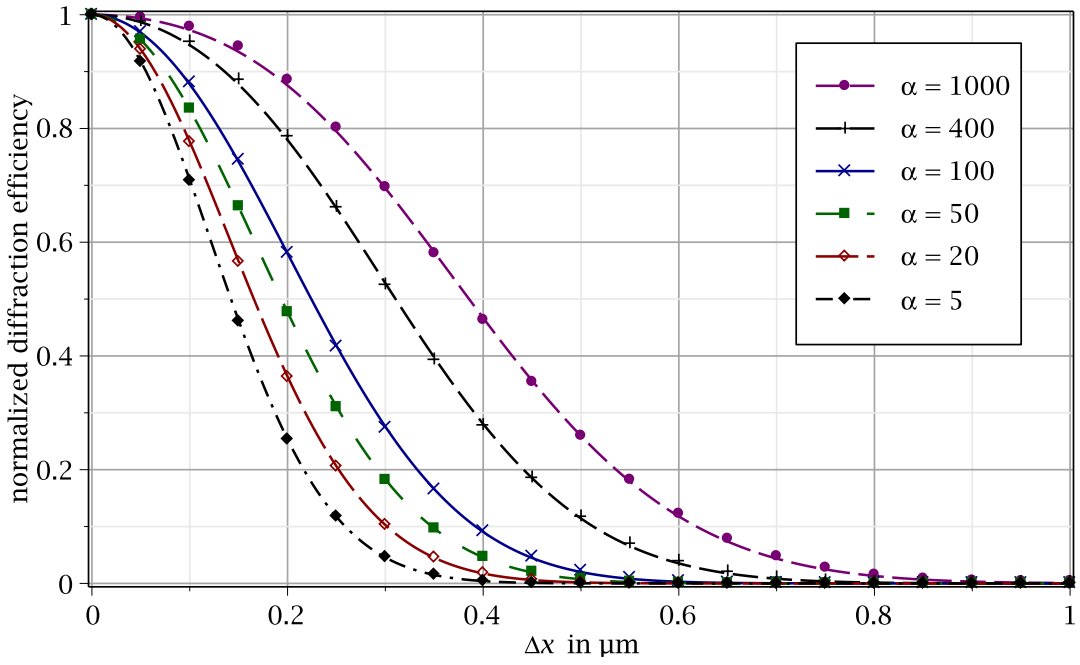

Figure 5.18: Lateral scanning: DE in terms of the focus position at several saturation parameters for the second grating profile.

The effective lateral size x_{eff} is the point at which the normalized DE reaches e^{-1}. In

this way, the calculated results can be compared to the results for gratings recorded with equal intensities in Section 5.3.

Figure 5.19 shows the effective lateral size of the gratings recorded with unequal intensities, together with the results for equal intensities. The effective lateral size of the gratings is larger if the recording intensities are unequal. The depletion of the grating contrast in the focal region leads to a larger effective width. This difference increases as the saturation parameter α gets larger because the depleted focal region of the gratings becomes larger. The stronger maxima of the improved grating profile, $n_{\max}(\vec{r}) - n_{\min,2}(\vec{r})$ seem to lead to a better lateral selectivity.

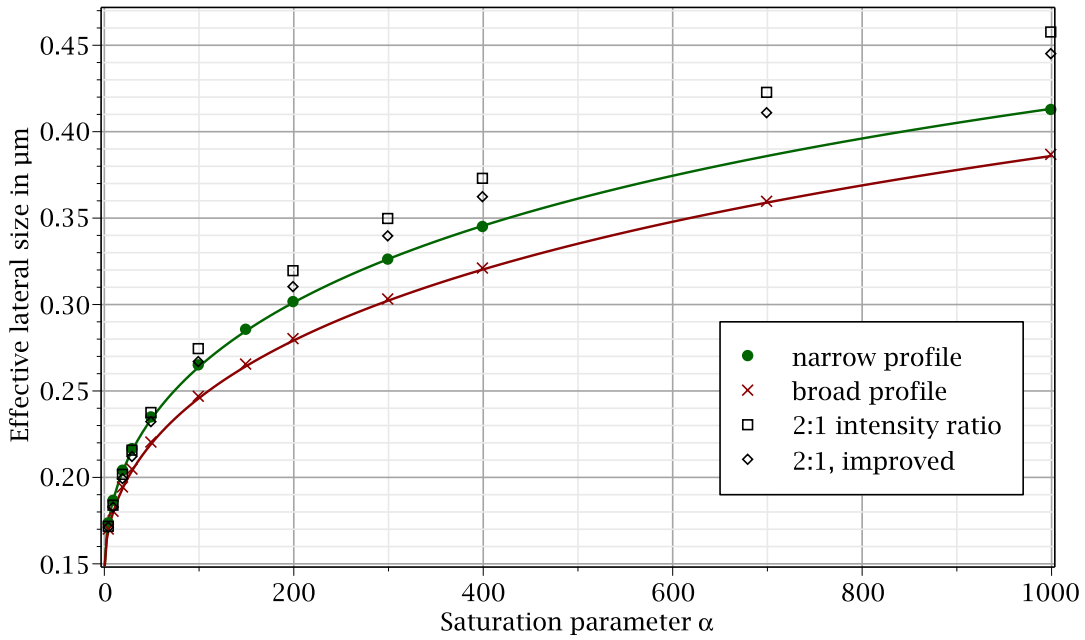

Figure 5.19: Effective width of gratings with intensity ratio of 2:1 in terms of saturation parameter, compared to the results in Figure 5.7.

For the lateral selectivity of microgratings, the lateral profile plays an important role. The effective width of the gratings is the smallest when the gratings are broad with strong contrast in the center, which enhances the contribution of the curved fringes. If the focus of the readout beam is shifted, phase mismatch of the wavefronts leads to a lower diffraction efficiency. As the phase mismatch is the largest in the grating region with the strongest curvature of the grating fringes, an enhanced index contrast in this region improves the lateral selectivity of microgratings with saturation.

Longitudinal selectivity of the gratings

By calculating the DE in terms of the focus position Δz along the optical axis, the effective depth of the microgratings with saturation with 2:1 intensity ratio is determined. As the readout beam is moved in the longitudinal direction, the change of the normalized DE can be described by a Lorentzian function

$$\left(1+\frac{\Delta z^2}{z_{\text{eff}}^2}\right)^{-1}.$$

Figure 5.20 shows the effective depth of the gratings (FWHM) in terms of the saturation parameter α. The results for the two profiles (points) are shown together with the results for the gratings with a narrow profile (green line with circles) and with a broad profile (red line). The narrow gratings have the largest depth, whereas the gratings with the broad profile have the shortest depth, as the stronger contrast of the curved fringes enhances the Bragg selectivity. The effective depth of the gratings with 2:1 intensity ratio is between the depth of the broad and the narrow gratings. With depleted contrast at the focus, a part of the enhanced selectivity of the broad gratings is lost.

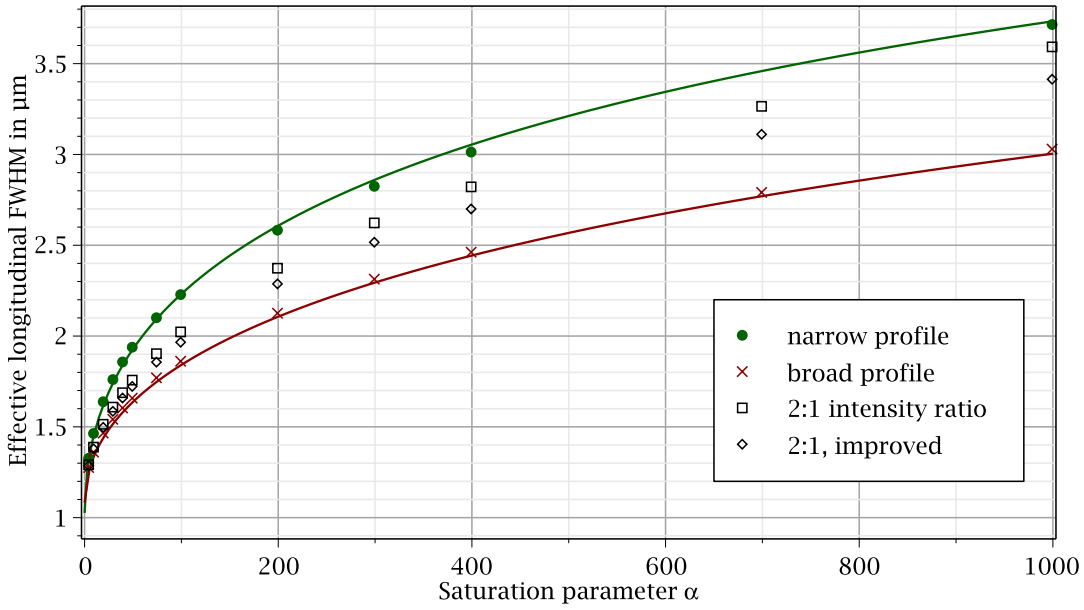

Figure 5.20: FWHM of the DE for longitudinal scanning in terms of the saturation parameter α, for gratings with 2:1 intensity ratio together with the results of Figure 5.8.

Wavelength selectivity of the gratings

In a saturating recording medium, microgratings have an enhanced wavelength selectivity compared to resolution-limited gratings. With unequal intensities of the recording beams, the contrast of the grating structure is depleted near the focus. This may change the spectral selectivity of the gratings, which is analyzed here.

The DE of the gratings can be described by the empirical fit function (4.22). Figure 5.21 shows the spectral FWHM of the gratings with unequal intensities. The two types give almost the same result, with a difference of up to 5 %. In the focal region, the radius of the readout beam is narrow compared to gratings with saturation. Thus the stronger maxima of the improved profile have little effect on the spectral selectivity.

The spectral width of these gratings is between the spectral width of the broad and the narrow profile. The lower spectral width of microgratings in saturating media is mainly due to the increased depth of these gratings, while the lateral profile in the focal region has a minor influence on this result. Even if the contrast of the grating at the focus drops to 8 % as in the example here, the gratings have a small spectral width.

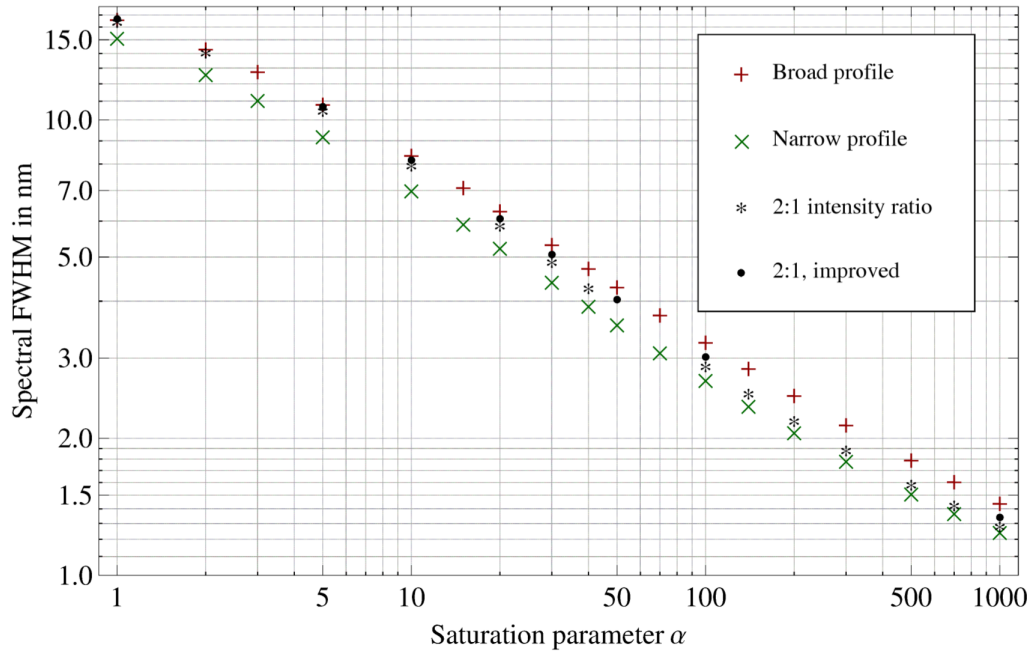

Figure 5.21: Spectral FWHM of the microgratings with 2:1 intensity ratio as a function of the saturation parameter α, together with results in Figure 5.10.

5.6 Conclusion

In this chapter, microgratings in a linear recording material with saturation were analyzed. The effects of saturation on the structure of microgratings, on the diffraction efficiency (DE) and on the spatial and spectral selectivity were described. A mathematical model for the profile of these microgratings was introduced, which was used to analyze and compare the characteristics of different types of microgratings in a saturating recording material.

The first type of microgratings are recorded with equal intensities of the recording beams. The grating structure is assumed to be unchanged, containing no higher harmonics. Enabled by the Bragg selectivity of the volumetric grating structure, the effective width of the microgratings at moderate saturation allows for optical data storage with a track pitch of 0.7 µm as in DVDs. A higher capacity per layer, comparable to Blu-ray discs, can hardly be reached.

Due to saturation, the gratings are larger and have more grating fringes, which enhances the DE. With a recording wavelength of 405 nm and $NA = 0.75$ it reaches 10^{-3} at an index contrast of 10^{-3}. The resolution-limited grating with the same parameters has a DE of the order of 10^{-6}.

Microgratings with saturation have an effective depth (FWHM of the DE) of up to 3 µm if the saturation is moderate ($\alpha \lesssim 400$). The effective depth of these gratings is much smaller than the real dimensions of the gratings. At $\alpha = 100$, which corresponds to an exposure energy density of about $2\,\mathrm{J/cm^2}$, the FWHM of the DE is around 2 µm, at a real depth (FWHM) of 5 µm of the grating.

In multilayer microholographic data storage, the achievable interlayer spacing is not only regulated by the diffraction effects of single microgratings which were evaluated in this chapter. It also depends on the recording material and on the consumption of the material dynamics by each layer, which is dictated by the real depth of the recorded microgratings.

The spectral width of the microgratings with saturation was analyzed as well. Microgratings with moderate saturation level α between 100 and 300 have a spectral FWHM

between 2 nm and 3 nm, which basically enables wavelength multiplexing. However, any multiplexing method which involves the storage of several microgratings at the same position may be completely impeded by saturation. The wavelength shift due to shrinkage of the material may reach the same order of magnitude, so that the DE drops.

The second type of microgratings are obtained with a 2:1 intensity ratio of the recording beams, when the reflected beam, which returns from the retroreflector unit, has 50 % intensity of the incident beam. The main feature of such gratings is a reduction of the contrast of the grating structure in the focal region, for example to 8 % at $\alpha = 400$. The effective width of these microgratings is slightly larger than for gratings without a depleted contrast near the focus. At $\alpha \lesssim 300$, the effective width is about 0.35 µm.

The longitudinal selectivity (FWHM) of these gratings is between the selectivity of the narrow grating and the smaller FWHM of the broad grating, with a value of 2 µm if $\alpha = 100$. Mostly influenced by the depth of the microgratings, not by their lateral profile, the spectral selectivity is between the selectivity of the narrow grating and of the broad grating.

In summary, saturation of the recording material produces larger microgratings with a higher diffraction efficiency. Enabled by Bragg diffraction, the microgratings can be localized with smaller dimensions compared to their real size. The drawback of saturation is that the consumption of material dynamics limits the prospects for multilayer data storage in linear recording media. This is analyzed in the next chapter.

6 Multilayer holographic data storage in saturating photopolymers

Microgratings written in a saturating recording material are larger in all the three dimensions. The diffraction effects of different microgratings were analyzed in the previous chapters. For strongly localized (resolution-limited) microgratings as in Chapter 4, diffraction mostly emerges from the confocal region of the grating. With saturation of the material, the regions of the microgratings beyond the focal area largely contribute to the diffraction efficiency during readout, as described in Chapter 5.

Due to saturation, consecutive microgratings in the same data track will overlap, even if they are laterally spaced several beam waists apart. Having an increased depth, the microgratings in adjacent layers overlap even with an interlayer spacing of several micrometers. When subsequent layers are recorded, the material dynamics are reduced. As a result, the feasibility of linear recording materials for multilayer data storage is limited, even if only a small number of tracks are recorded, which is analyzed in this chapter.

To illustrate the overlapping microgratings and to give an idea of the effects which occur, Figure 6.1 shows two adjacent microgratings. They are recorded at a wavelength of 405 nm with $NA = 0.75$ in a material with a refractive index of $n_0 = 1.5$ and the maximum index contrast is $\Delta n = 0.001$. Linearly recorded microgratings without saturation are strongly localized. As the index contrast decreases rapidly with distance from the focus, the gratings are well separated from each other, as shown in Figure 6.1a.

Gratings with saturation are larger than the linearly recorded ones, which causes them to overlap more easily. Figure 6.1b shows two gratings separated by a lateral spacing of 1 µm. At a distance of $|z| > 2z_R$ from the focus, the gratings start to overlap.

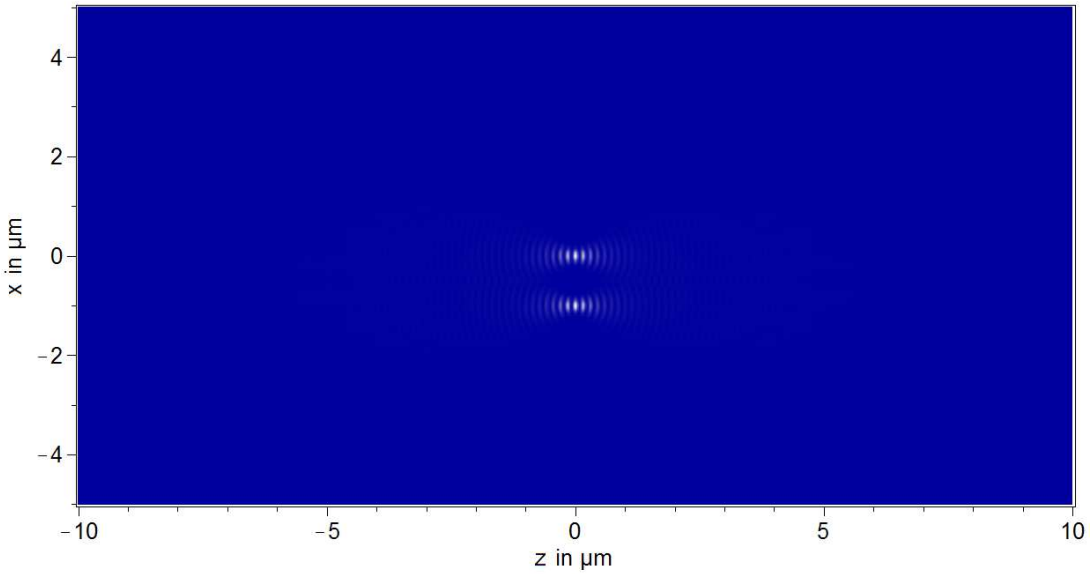

(a) Two microgratings without saturation, separated laterally by 1 µm.

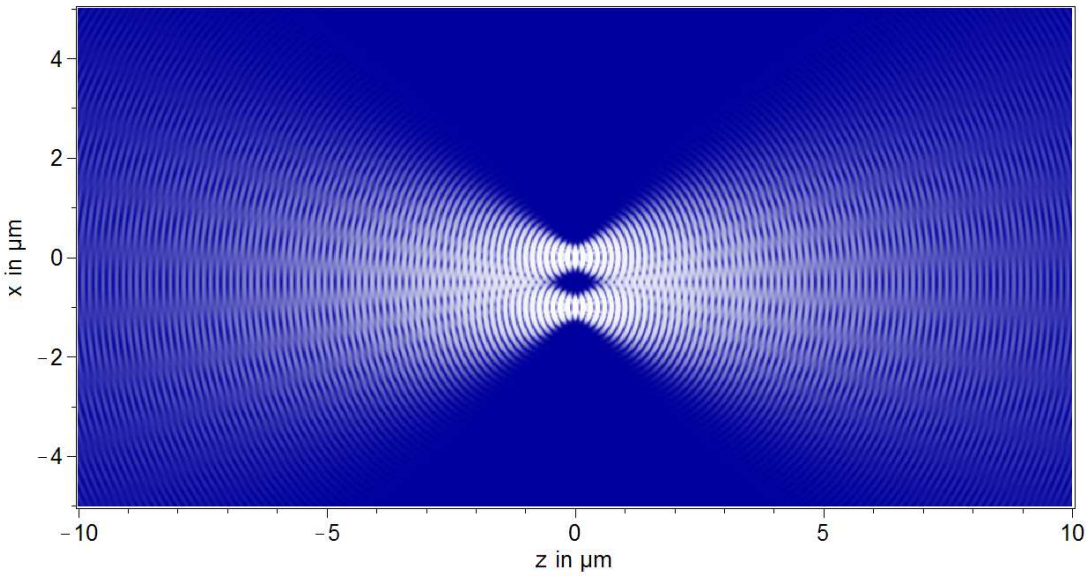

(b) Two gratings with saturation, separated laterally by 1 µm.

Figure 6.1: Microgratings without saturation (a) and with saturation $\alpha = 400$ (b,c). Parameters: wavelength 405 nm, $NA = 0.75$, refractive index of recording material $n_0 = 1.5$, and maximum index contrast $\Delta n = 0.001$

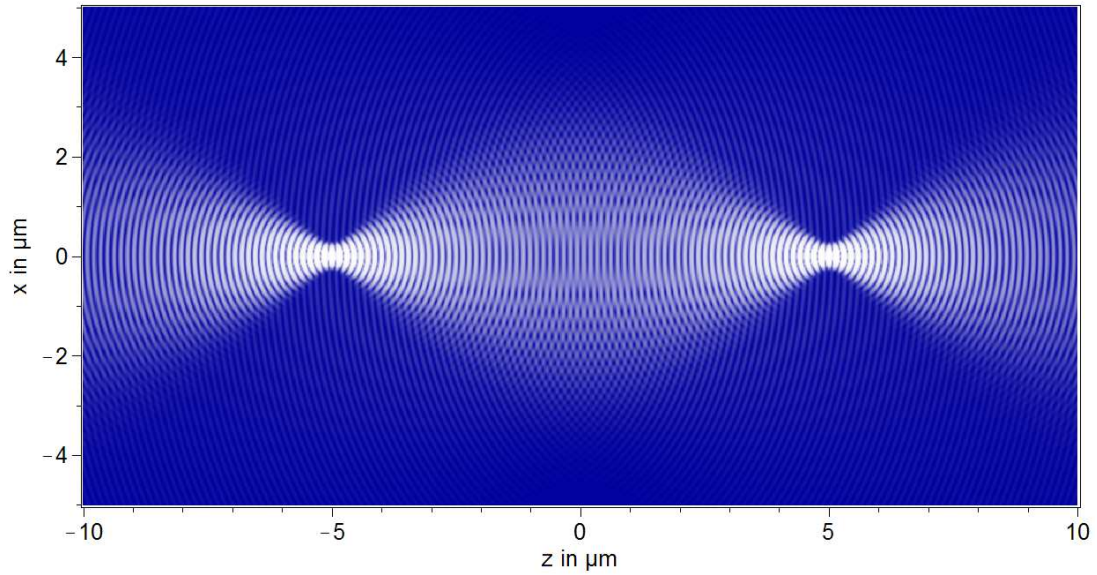

(c) Two gratings with saturation, separated in z by 10 µm.

Figure 6.1: (continued)

The grating structures interfere, occupying virtually the same region of the recording material. Figure 6.1c displays two gratings which are separated by an interlayer spacing of 10 µm. In spite of the large distance, the gratings share a large volume between the two spots. Above and below the focus of each grating, the structure of the other grating is clearly visible.

Multilayer data storage in a saturating recording material requires an appropriate exposure schedule. As the gratings are extended in depth, writing a track of data in one layer induces consumption of the material dynamics in the adjacent layers as well. Consequently, if gratings are recorded in several layers with equal exposure energies, the diffraction efficiency decreases from layer to layer, which is a hindrance to multilayer data storage. Such overlapping microgratings may also reduce the quality of the readout signal.

In linear recording materials, multilayer data storage with full layers is hardly feasible, since during writing of one layer all other layers receive the same exposure dose. Recording media with a quadratic material characteristic, such as two-photon sensitized media [82], confine the exposed volume. Recently multilayer microholographic data

storage with two-photon recording was achieved with holographic transmission gratings in a lithium tantalate crystal [83] and in a cationic ring-opening polymerization material [84]. Microholographic data storage proposed by Orlic *et. al.* uses volumetrically localized reflection gratings. The results of transmission-grating storage cannot be directly transferred to reflection gratings with a smaller grating period and smaller dimensions.

Linear recording media with an intensity threshold level would constrain the change of the refractive index to the layer being recorded, which enables multilayer data storage [85, 86]. During writing of one layer, both the intensity and the exposure time for each point in the volume of the recording material depend on the depth position. A threshold in terms of exposure energy density instead of intensity would be overcome after the first layer has been recorded. If the threshold is at 10 % of the maximum exposure energy density of one micrograting, recording of one data layer with an average filling factor of 10 % will virtually cancel the threshold for subsequent recordings in the whole volume of the material.

When subsequent layers of data are recorded with equal exposure energy density in a saturating linear recording material, the diffraction efficiency decreases from layer to layer. Equalized diffraction efficiencies of multiple layers, which are essential for the signal quality, require an appropriate recording schedule. Increasing recording times compensate for the loss of material dynamics due to subsequent recording. A nearly equal diffraction efficiency of multiple layers is achieved, which depends on the number of layers and on the interlayer spacing.

This chapter is focused on linear recording materials with saturation. In Section 6.1 the effect of subsequent data storage in multiple layers on the material dynamics and the resulting index contrast of each grating is described. To equalize the diffraction efficiencies of the layers, exposure schedules are derived. The method is described in Section 6.2. For data storage with capacities from one grating per layer to three tracks per layer, the exposure schedules and the achieved diffraction efficiency are analyzed in Section 6.3. Schedules for multilayer data storage are described in Subsection 6.3.4. Consequences and limitations of data storage in linear photosensitive materials with saturation are obtained.

6.1 Refractive index contrast in multilayer recording

In a saturating recording material, the gratings overlap and extend into the adjacent layers. When a grating or a track of data is recorded, some part of the material dynamics is consumed in the other layers. If several gratings or tracks are recorded in subsequent layers with equal exposure energies, the diffraction efficiency of each grating decreases from layer to layer, reducing the available number of layers and their signal quality. This is modeled in this section using a mathematical description of the index contrast of the gratings.

A complete material model should include all the relevant chemical processes and nonlocal material dynamics, especially the polymerization and the diffusion of the monomers and of the short polymer chains [38, 85]. Monomer diffusion can already start during recording as it takes time to move the optical head from one layer to another. Due to some shrinkage of the recording material, wavelength shift and DE loss may occur. These effects are not included here as this would require a full study of the material dynamics.

The analysis starts with two layers. Recording data in the first layer consumes some of the resources in the material. Consequently the index contrast for the second layer is reduced, provided that both layers are recorded with equal exposure energy. With the saturation function as in Chapter 5,

$$f_\alpha(\gamma(\vec{r})) = \frac{(1+\alpha)\gamma(\vec{r})}{1+\alpha\,\gamma(\vec{r})}\,, \tag{6.1}$$

the normalized index contrast of the first two gratings can be described in the following way:

$$\begin{aligned} \frac{\Delta n_1(\vec{r})}{\Delta n_{\max}} &= f_\alpha\left(\gamma_1(\vec{r})\right) \\ \frac{\Delta n_2(\vec{r})}{\Delta n_{\max}} &= \left(1-\beta\frac{\Delta \widehat{n}_1(\vec{r})}{\Delta n_{\max}}\right) f_\alpha\left(\gamma_2(\vec{r})\right)\,. \end{aligned} \tag{6.2}$$

Here, $\gamma_j(\vec{r}) = I_j(\vec{r})/I_{\max}$ is the normalized intensity which is applied when the j-th grating is written. The saturation parameter α is adapted corresponding to the exposure energy density and the saturation function of the material. A constant factor β between 0 and 1 describes the filling factor of the tracks or layers. As indicated by $\widehat{n}$, only the index contrast is included, not the grating structure itself, as the consumption

of material most likely is not as local as $\lambda/2$. Now if several tracks are written, the available material dynamics are reduced by the sum of the normalized contrasts of all previously written gratings, multiplied by β:

$$\frac{\Delta n_j(\vec{r})}{\Delta n_{\max}} = \left(1 - \beta \sum_{\ell=1}^{j-1} \frac{\Delta \widehat{n}_\ell(\vec{r})}{\Delta n_{\max}}\right) f_\alpha\left(\gamma_j(\vec{r})\right) \ . \tag{6.3}$$

The recursion equation (6.3) is equivalent to the non-recursive equation

$$\frac{\Delta n_j(\vec{r})}{\Delta n_{\max}} = \prod_{\ell=1}^{j-1} \left[1 - \beta f_\alpha\left(\widehat{\gamma}_\ell(\vec{r})\right)\right] f_\alpha\left(\gamma_j(\vec{r})\right) \ . \tag{6.4}$$

Proof. Starting at (6.4) and shortly writing $A_\ell = 1 - \beta f_\alpha\left(\widehat{\gamma}_\ell(\vec{r})\right)$,

$$\begin{aligned} a &= \frac{\Delta n_j(\vec{r})}{\Delta n_{\max}} + \beta \frac{\Delta \widehat{n}_{j-1}(\vec{r})}{\Delta n_{\max}} f_\alpha\left(\gamma_j(\vec{r})\right) \\ &= \left(\left[\prod_{\ell=1}^{j-1} A_\ell\right] + \beta \left[\prod_{\ell=1}^{j-2} A_\ell\right] f_\alpha\left(\widehat{\gamma}_{j-1}(\vec{r})\right)\right) f_\alpha\left(\gamma_j(\vec{r})\right) \ , \end{aligned}$$

which yields

$$a = \left[\prod_{\ell=1}^{j-2} A_\ell\right] f_\alpha\left(\gamma_j(\vec{r})\right) \ .$$

By adding the $(j-1)$-th term, the upper index of the product is reduced by one. The next step is

$$a' = a + \beta \frac{\Delta \widehat{n}_{j-2}(\vec{r})}{\Delta n_{\max}} f_\alpha\left(\gamma_j(\vec{r})\right) = \left[\prod_{\ell=1}^{j-3} A_\ell\right] f_\alpha\left(\gamma_j(\vec{r})\right) \ .$$

Step by step, this iteration finishes saying (6.3):

$$\frac{\Delta n_j(\vec{r})}{\Delta n_{\max}} + \beta \sum_{\ell=1}^{j-1} \frac{\Delta \widehat{n}_\ell(\vec{r})}{\Delta n_{\max}} f_\alpha\left(\gamma_j(\vec{r})\right) = f_\alpha\left(\gamma_j(\vec{r})\right) \ .$$

■

An example which shows the overlap of consecutive gratings is a row of gratings with their focus positions equally spaced on the optical axis (the z axis). Along the z axis, the normalized intensity which is used for recording of the ℓ-th grating yields

$$\widehat{\gamma}_\ell(z\vec{e}_z) = \frac{1}{1 + \frac{(z - \ell \cdot s)^2}{z_R^2}} \ , \tag{6.5}$$

where z_R is the Rayleigh length and s is the interlayer spacing.

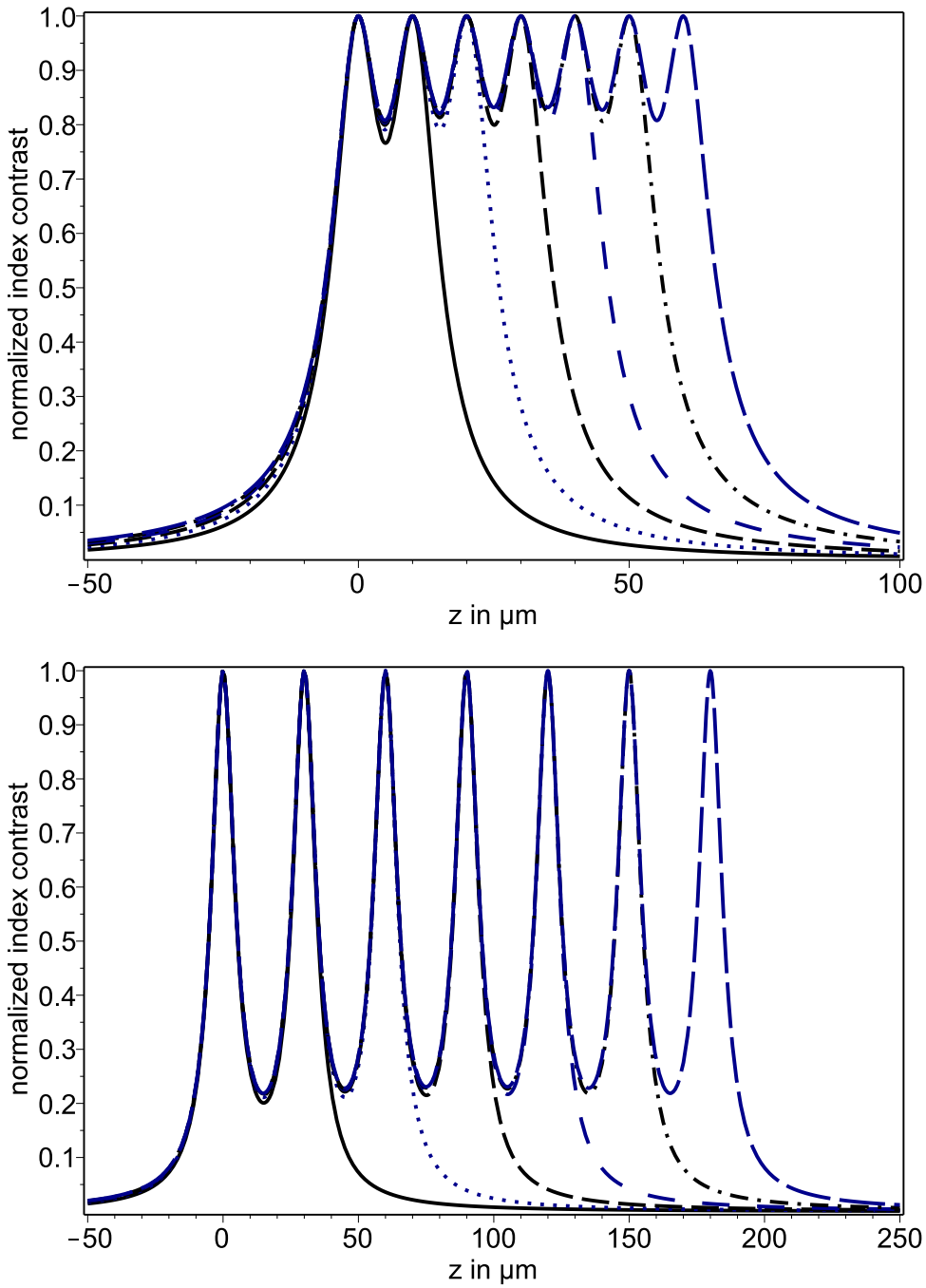

Figure 6.2: Gratings with saturation $\alpha = 400$ (FWHM $\approx$ 10 µm in z) in 2 to 7 layers with an interlayer spacing of 10 µm (top) or 30 µm (down). Only the normalized index contrast is shown.

Figure 6.2 shows the normalized index contrast of the overlapping gratings with saturation parameter $\alpha = 400$ in a cross section along the z axis, recorded at a wavelength of 405 nm with $NA = 0.75$ in a material with a refractive index of $n_0 = 1.5$. The smaller the interlayer spacing or the stronger the saturation effect, the more the gratings overlap. Obviously the total index contrast reaches the same value on each grating. The gratings overlap so that the index contrast belonging to each grating decreases, and the diffraction efficiency will decrease accordingly.

The decrease of the diffraction efficiency from layer to layer was shown in experiments by S. Frohmann [8]. He recorded data in one track per layer as shown in Figure 6.3, separated by an interlayer spacing s, waited 30 seconds and then read out the track which had been recorded as the last one. As the number of layers increased, the diffraction efficiency decreased. A maximum number of seven layers could be achieved.

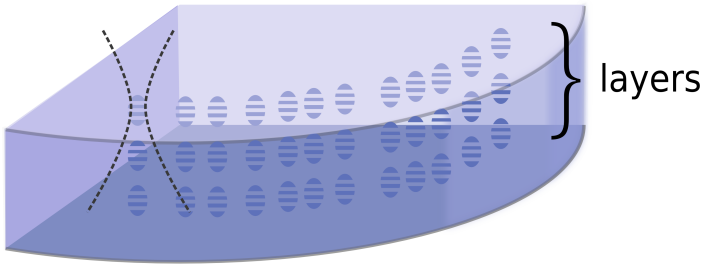

Figure 6.3: Recording of one data track per layer in a transparent disc. Three tracks are shown, together with a pair of dotted lines indicating the incident beam.

The result by S. Frohmann [8] showed that for an interlayer spacing of 15 µm the diffraction efficiency (DE) decreased from layer to layer. For smaller interlayer spacing however the DE of the first few gratings stayed on one level. This can be explained by the shared consumption of monomers by the overlapping gratings [8]. Closely spaced gratings share large parts of the exposed volume. Effects which include time-

dependent processes in the material, such as the diffusion of monomers, are generally not included in this thesis as this would require a full study of the effects in the material.

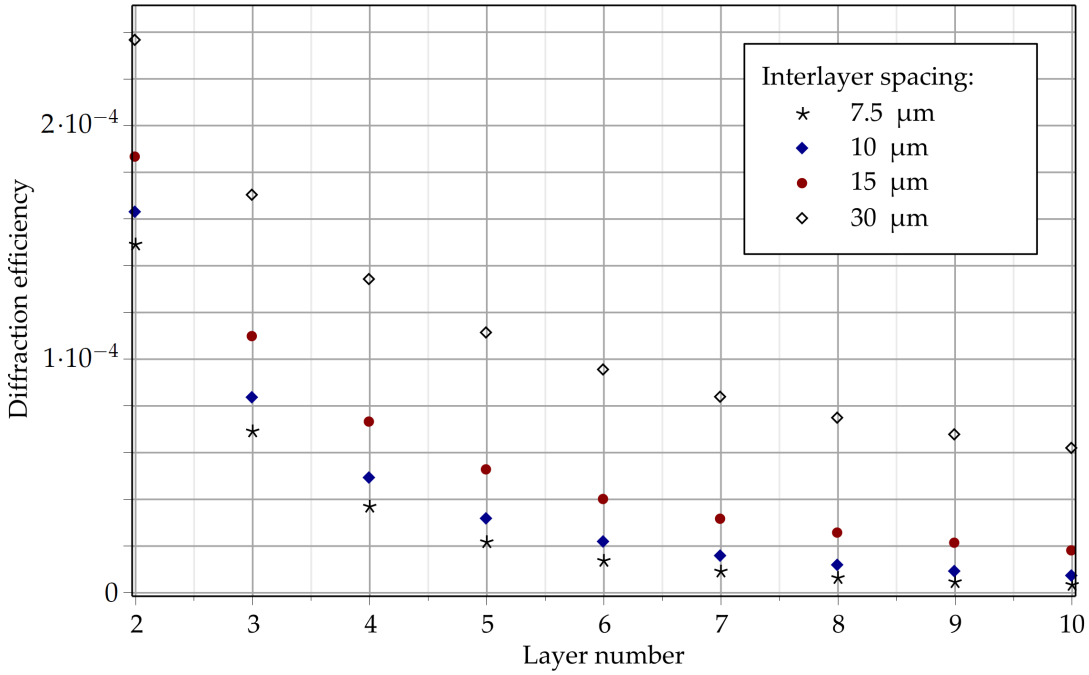

Figure 6.4: Diffraction efficiency for recording of one track per layer with equal exposure and saturation $\alpha = 100$. DE of the first layer is $4 \cdot 10^{-4}$ in each case.

According to the material function of a blue-sensitive STX Aprilis E-Type photopolymer (Figure 5.1), the saturation parameter is $\alpha = 100$ if the exposure energy density is $2\,\mathrm{J/cm^2}$. Figure 6.4 shows the DE for ten layers recorded with these parameters. For an interlayer spacing of 15 µm, the reduction of the DE from layer to layer is similar to the results in [8]. The shared consumption of monomers is not included, which plays a minor role at interlayer spacings of 15 µm or larger.

6.2 Exposure schedules for multilayer data storage

In a linear recording material with saturation, the diffraction efficiency decreases from layer to layer if the exposure energy density is the same. With a suitable exposure schedule, equalized diffraction efficiencies are achieved. For multilayer data storage, the method to derive such schedules is introduced in this section.

The type of schedule depends on the type of the recording material. In photorefractive materials such as $LiNbO_3$, which are used for switchable holograms [87], previously written gratings are partly erased during subsequent recording [88, 89]. To compensate for this effect, decreasing exposure times are required [76, 88, 90]. The first grating, which suffers the most from erasure, receives the largest exposure time.

In contrast, in saturable materials like photopolymers, the exposure times must increase from the first to the last grating [91–93]. The low exposure energies of the first gratings save enough material resources for the last gratings. Compared to angular and peristrophic multiplexing of extended gratings in the same volume as in [91–93], microholographic data storage is achieved by shift multiplexing, so that the larger microgratings overlap partially. This requires a different method and yields different schedules, which are derived in this chapter.

The consumption of material induced by each layer depends on the number of gratings or tracks which are stored therein. The track pitch and the average in-track spacing between the microgratings (or the fill factor of the bit sequence) control the data density of the layers. The achievable diffraction efficiency in multilayer data storage also depends on the interlayer spacing and on the number of layers to be stored.

6.2.1 Equation system for multilayer data storage

The normalized index contrast of a grating in the j-th layer is given by (6.4) if the exposure energy density is constant. With additional parameters b_j, varied exposure energy densities for each layer are included. As the radius of the Gaussian beam at the interlayer spacing s is much larger than the spot size, the lateral profile of the previously written gratings can be neglected. For convenience, $\widehat{\gamma}_\ell(\vec{r})$ is now written as

$\widehat{\gamma}_\ell(z)$. This yields

$$\frac{\Delta n_j(\vec{r})}{\Delta n_{\max}} = \prod_{\ell=1}^{j-1} \Big[1 - \beta\, f_\alpha\left(b_\ell\, \widehat{\gamma}_\ell(z)\right)\Big] f_\alpha\left(b_j\, \gamma_j(\vec{r})\right) \ . \tag{6.6}$$

In the following, the interlayer spacing is denoted as s. The coordinate system is shifted along the z axis by $j \cdot s$ to the center of the j-th layer, which is denoted as $\vec{r} = 0$. As an approximation, the material-consumption factors are replaced by their value at the center of the j-th layer:

$$\frac{\Delta n_j(\vec{r})}{\Delta n_{\max}} \approx \prod_{\ell=1}^{j-1} \Big[1 - \beta\, f_\alpha\Big(b_\ell\, \widehat{\gamma}_\ell((j-\ell)\, s)\Big)\Big] f_\alpha\left(b_j\, \gamma_j(\vec{r})\right) \ . \tag{6.7}$$

The diffraction efficiency of a grating in the j-th layer can now be calculated as

$$DE_j \approx \prod_{\ell=1}^{j-1} \Big[1 - \beta\, f_\alpha\Big(b_\ell\, \widehat{\gamma}_\ell((j-\ell)\, s)\Big)\Big]^2 DE(\alpha, b_j) \ . \tag{6.8}$$

With the saturation function as in (5.5), namely

$$f_\alpha(\gamma(\vec{r})) = \frac{(1+\alpha)\gamma(\vec{r})}{1 + \alpha\, \gamma(\vec{r})} \ , \tag{6.9}$$

it can be shown that

$$f_\alpha(b \cdot \gamma(\vec{r})) = f_{\alpha \cdot b}(\gamma(\vec{r})) f_\alpha(b) \ . \tag{6.10}$$

Using (5.12), the diffraction efficiency $DE(\alpha, b_j)$ in (6.8) is written as

$$DE(\alpha, b_j) = f_\alpha^2(b_j) \left(1.41468 \cdot 10^{-5} + 3.95501 \cdot 10^{-6} \alpha b_j - 7.49766 \cdot 10^{-10} \alpha^2 b_j^2\right) \ . \tag{6.11}$$

For some fixed diffraction efficiency DE_{fix}, the equation system $DE_j = DE_{\text{fix}}$ with (6.8) is solved for b_1 to b_N, where N is the number of layers. For a blue-sensitive STX Aprilis E-Type photopolymer (Figure 5.1), the saturation parameter $\alpha = 100$ and $b = 1$ correspond to an exposure energy density of $2\,\text{J/cm}^2$. To provide ample range of exposure energy densities, the saturation parameter is set to $\alpha = 1000$, so that $0 \leq b \leq 1$ corresponds to exposure energy densities of up to $20\,\text{J/cm}^2$.

For one grating per layer, the results of the approximation (6.8) are accurate enough. If tracks are recorded, especially for three tracks per layer or more, the dependence of the material-consumption factors on z has to be included. The preliminary exposure energy densities given by (6.8) have to be improved using diffraction integrals, as described on the next page.

6.2.2 Improved schedules with the secant method

In (6.8), the material-consumption factors are assumed to be constant over the whole micrograting. The variation of the factors with z causes deviations of the diffraction efficiencies from the fixed value DE_{fix}. For data storage tasks with a small number of microgratings per layer, such as one grating per layer, the error of the diffraction efficiencies will be small. However, for multilayer storage with tracks, an improved method to compute the schedules is needed, which is described here. In most cases, the exposure energy densities have to be larger than the results of (6.8).

To calculate the diffraction efficiency of a grating in the j-th layer, DE_j, the normalized index profile (6.6) is included in a diffraction integral as in Chapter 4. As the interlayer spacing is typically several micrometers, much larger than the Rayleigh length of the recording beams, the lateral profile of the material-consumption factors is very broad and can be replaced by its value on the z axis. The normalized index contrast of a grating in the j-th layer yields

$$\frac{\Delta n_j(\vec{r})}{\Delta n_{\max}} = \prod_{\ell=1}^{j-1} \left[1 - \beta f_\alpha\Big(b_\ell\, \widehat{\gamma}_\ell(z + (j-\ell)\, s)\Big)\right] f_\alpha\left(b_j\, \gamma_j(\vec{r})\right) \ . \tag{6.12}$$

Starting with b_1, each coefficient is improved with the secant method. To label the updates of the coefficients, a second index is added. As starting values, the coefficients $b_1^{(0)}, \ldots, b_N^{(0)}$, where N is the number of layers, are computed with the method in Subsection 6.2.1. The first iteration step is

$$b_j^{(1)} = \frac{DE_{\mathrm{fix}}}{DE_j^{(0)}}\, b_j^{(0)} \ , \tag{6.13}$$

followed by the next steps with $i = 1, 2, \ldots$:

$$b_j^{(i+1)} = b_j^{(i)} - \frac{DE_j^{(i)} - DE_{\mathrm{fix}}}{DE_j^{(i)} - DE_j^{(i-1)}} \left(b_j^{(i)} - b_j^{(i-1)}\right) \ . \tag{6.14}$$

The new coefficients which are finished are inserted in (6.12) before the next coefficient is adjusted. The method needs few iterations, at most four iterations in the example for three tracks in Subsection 6.3.3.

6.3 Multilayer data storage from gratings to full layers

6.3.1 One grating per layer

Storing one micrograting in each layer makes the lowest demands on the storage material. Even in this case, the achievable diffraction efficiency (DE) of gratings with saturation is limited due to the overlap of the gratings in adjacent layers. Recording one micrograting at $\vec{r} = 0$, the normalized exposure of the material is

$$\exp\left(-2\frac{x^2+y^2}{w^2(z)}\right)\frac{w_0^2}{w^2(z)} \approx \frac{w_0^2}{w^2(z)} \; . \tag{6.15}$$

When the gratings are stored at $x = y = 0$ with an interlayer spacing s, the DE of a grating in the j-th layer is

$$DE_j = \prod_{\ell=1}^{j-1}\left[1 - f_\alpha\left(b_\ell \cdot \frac{w_0^2}{w^2((j-\ell)\,s)}\right)\right]^2 DE(\alpha, b_j) \; . \tag{6.16}$$

The recording material has a refractive index of $n_0 = 1.5$ and an index contrast of $\Delta n = 0.001$. Figures 6.5 and 6.6 show the exposure schedules for three DE with interlayer spacing of 7.5 µm and 15 µm, respectively. As the material consumption of a single micrograting decays quickly with depth, the exposure energy densities settle after the tenth layer as only a few gratings contribute to the material consumption. The exposure energy density ρ of the i-th grating can be described by the empirical function

$$\rho_i = \rho_{50} \cdot f_c\left(\frac{i}{50}\right) \; , \tag{6.17}$$

where ρ_{50} is the exposure energy density of the 50th grating, f_c is the saturation function given in (6.9), and c is a parameter which describes how quickly the exposure energy densities level off, which should not be confused with the saturation parameter of a grating, α.

With an interlayer spacing of 7.5 µm, a DE of $3 \cdot 10^{-4}$ is achieved with exposure energy densities of at most 2.34 J/cm^2. However, if the DE is set to a higher value, the exposure energy density in terms of the layer number increases for all layer numbers, as can be seen in Figure 6.5 for DE $= 4 \cdot 10^{-4}$. This is clearly due to high material consumption. With even higher DE the exposure energy densities increase more steeply and a lower number of layers is available.

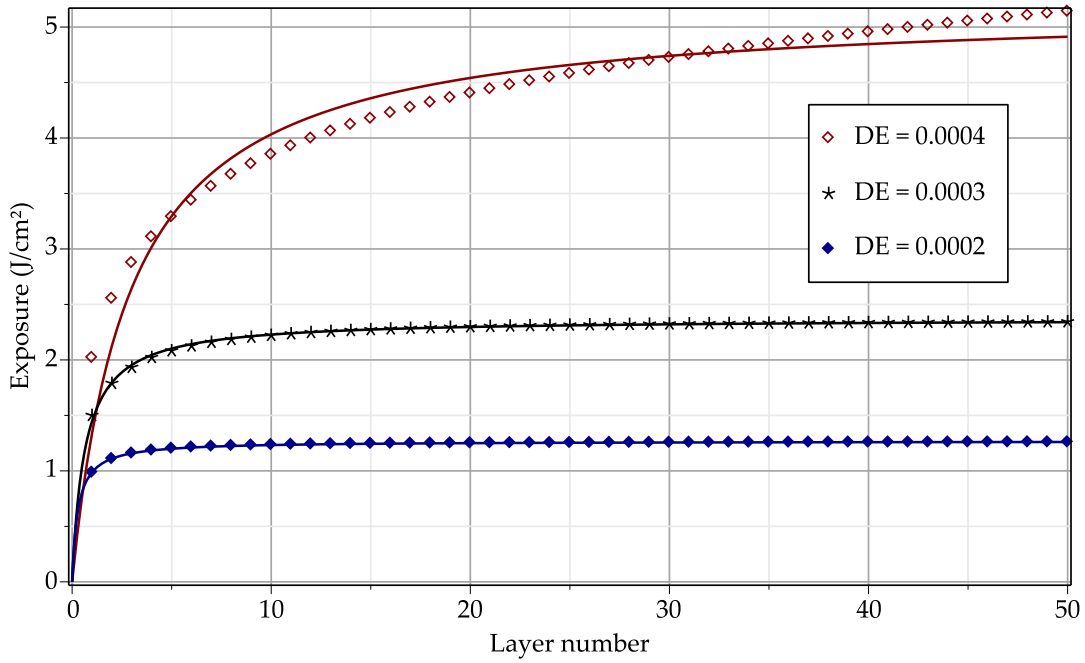

Figure 6.5: Schedules for recording of one grating per layer with interlayer spacing 7.5 µm.

An interlayer spacing of 15 µm enables a higher DE of $1 \cdot 10^{-3}$ and doubles the required thickness of the recording material. The exposure energy densities of at most 7.73 J/cm^2 (Figure 6.6) correspond to a saturation parameter of $\alpha \lesssim 400$.

As shown in Figure 6.7, the diffraction efficiency can be improved by enlarging the interlayer spacing. Each point shows the largest DE for which the exposure energy densities are nearly constant after the 20th layer. The error bars show the uncertainty of this decision. If one grating is recorded in each of 50 layers with interlayer spacing of at least 14 µm, a diffraction efficiency of 10^{-3} can be reached. With an interlayer spacing of 7.5 µm, only a diffraction efficiency of the order of 10^{-4} is achievable. The DE in terms of the interlayer spacing s (in µm) can be approximately described by

$$\mathrm{DE}(s) = 2.69 \cdot 10^{-6}\, s^2 + 4.18 \cdot 10^{-5}\, s - 1.16 \cdot 10^{-4}\,. \tag{6.18}$$

Even if only one grating per layer is stored in a linear recording material with an index contrast of $\Delta n = 0.001$, the diffraction efficiencies are in the range of 10^{-4} to 10^{-3}. To achieve higher diffraction efficiencies, the gratings should be stored at separate lateral positions or rather be stored in tracks. Reducing the NA or a larger index contrast improves the DE as well.

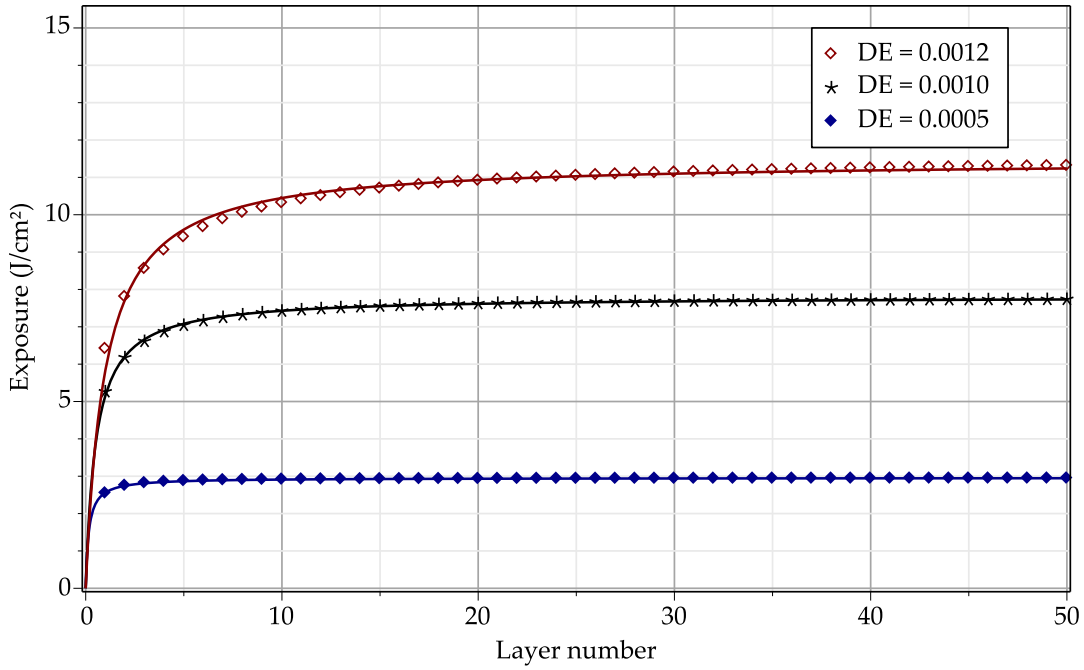

Figure 6.6: Schedules for recording of one grating per layer with interlayer spacing 15 µm.

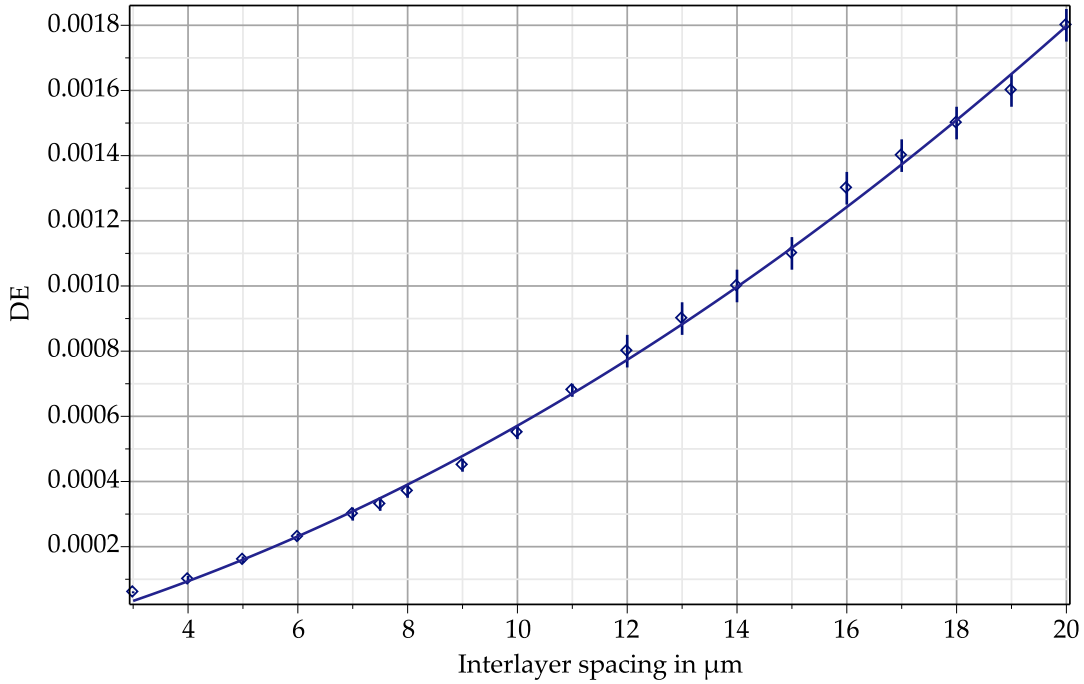

Figure 6.7: Diffraction efficiency available for one grating in each of 50 layers in terms of the interlayer spacing.

6.3.2 One track per layer

The storage of one track per layer is the first step towards multilayer data storage. With seven layers and without an exposure schedule, this was done in experiments by S. Frohmann [8]. The decreasing diffraction efficiency limited the number of layers. To achieve equal diffraction efficiencies in every track and more layers, an exposure schedule is derived.

The tracks are recorded at the same lateral position $y = 0$ with an interlayer spacing s. As the radius of an optical disc is a few centimeters, the spiral tracks can be considered as parallel and equidistant straight lines. Recording one track means at most one whole turn of the disc during exposure. When one of these tracks is recorded in the layer at $z = 0$ with constant power, the normalized exposure of the recording material yields

$$\sqrt{\frac{2}{\pi}}\frac{1}{w_0}\int_{-\infty}^{\infty}\exp\left(-2\frac{x^2+y^2}{w^2(z)}\right)\frac{w_0^2}{w^2(z)}\mathrm{d}x = \exp\left(-\frac{2\,y^2}{w^2(z)}\right)\frac{w_0}{w(z)} \approx \frac{w_0}{w(z)}\,. \tag{6.19}$$

As the lateral profile of a high-NA Gaussian beam in the distance of several micrometers is broad, the exposure is approximated by setting $y = 0$. For every track of data, the bit sequence is supposed to have an average amplitude of 1/2, which contains logical zeroes and ones with equal possibility. The diffraction efficiency of a grating in the j-th layer is

$$DE_j = \prod_{\ell=1}^{j-1}\left[1 - \frac{1}{2}f_\alpha\left(b_\ell \cdot \frac{w_0}{w((j-\ell)\,s)}\right)\right]^2 DE(\alpha, b_j)\,. \tag{6.20}$$

While one grating per layer can be recorded with equal diffraction efficiencies except for the first few gratings, the schedules for data storage with tracks are different. The outreach of the material consumption into the deeper layers decreases slowly, which has to be compensated by rising exposure energies.

As above, the refractive index of the recording material is $n_0 = 1.5$ and the maximum index contrast is $\Delta n = 0.001$. Figure 6.8 shows two schedules for 20 layers with an interlayer spacing of $s = 7.5\,\mu\mathrm{m}$. The diffraction efficiency (DE) dictates the maximum energy density which is needed for the last layer. For 20 layers, only a DE below $3 \cdot 10^{-5}$ is available.

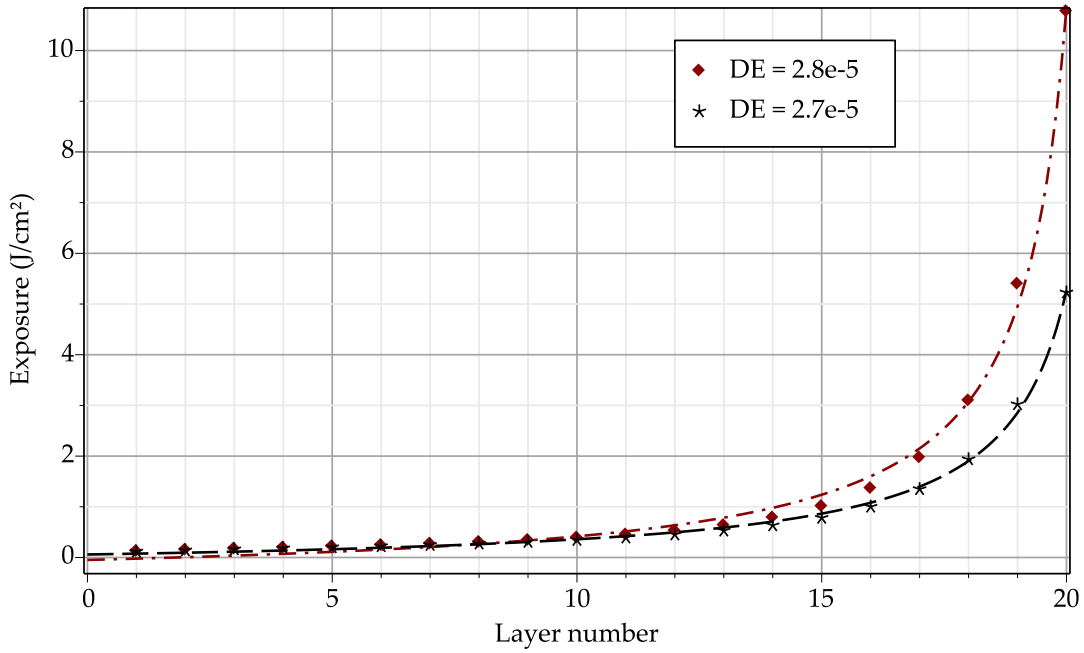

Figure 6.8: Schedules for one track in each of 20 layers with interlayer spacing 7.5 µm.

Figure 6.9 shows two schedules for 50 layers with an interlayer spacing of 15 µm, recorded with a fill factor of 1/2. With a slightly different diffraction efficiency, the exposure schedules change profoundly, for example comparing DE $= 3.1 \cdot 10^{-5}$ to DE $= 3.0 \cdot 10^{-5}$. This can be explained by the slow decrease of the DE in terms of the number of layers. If the DE is set to a slightly lower value, the maximum number of layers is higher and the exposure energies rise much more slowly.

Figure 6.10 displays the available DE in terms of the number of layers with an interlayer spacing of 7.5 µm and 15 µm. Recording one track in each of ten layers with a spacing of 15 µm, a diffraction efficiency of 10^{-4} is available, which yields a poor signal quality due to the material noise of $10^{-5} - 10^{-4}$ in blue-sensitive Aprilis media [8].

There is some scope to improve the DE. With a larger interlayer spacing, the diffraction efficiency can only be increased to values below 10^{-3}. To improve the SNR, sparse coding (with a reduced number of logical ones) could help to relieve the material. Figure 6.10 shows the DE for a fill factor of 20 % with an interlayer spacing of 15 µm. A DE of 10^{-3} is reached for up to five layers. Reducing the NA from 0.75 to 0.5 yields a seven-fold DE with a 2.7-fold interlayer spacing.

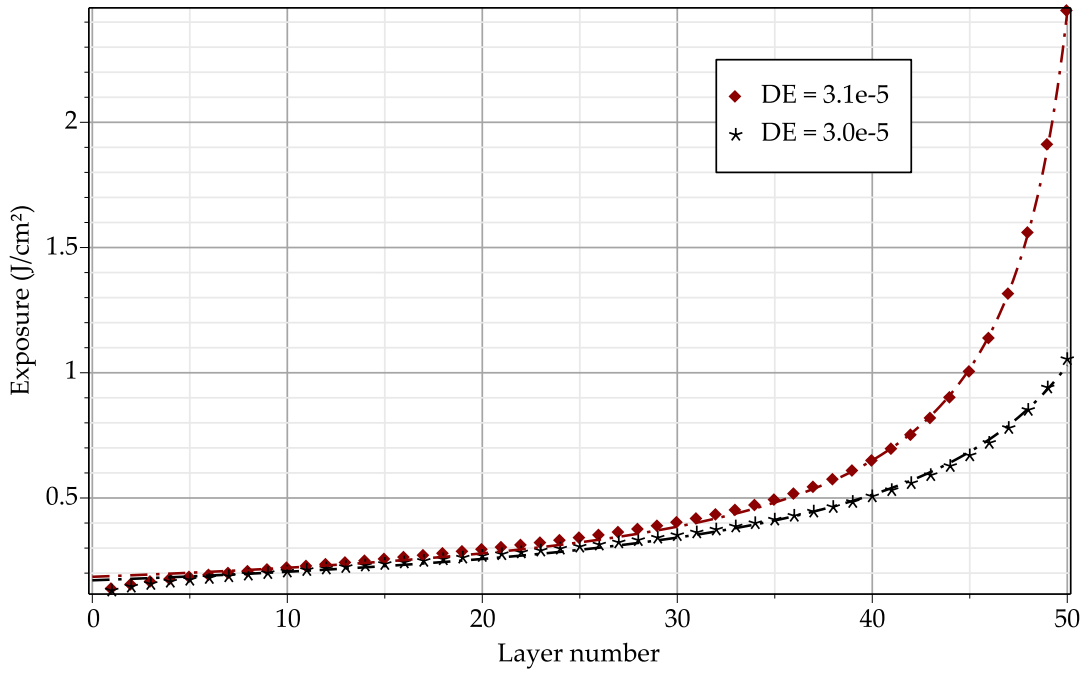

Figure 6.9: Schedules for one track in each of 50 layers with interlayer spacing 15 µm.

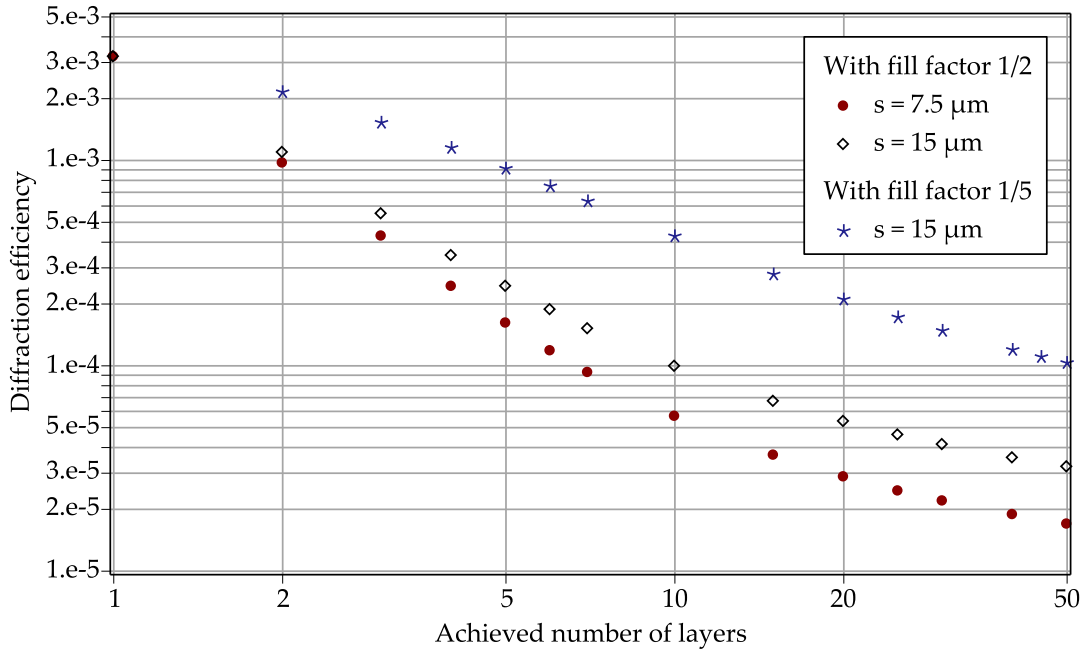

Figure 6.10: Recording of one track per layer: Diffraction efficiency available in terms of the number of layers with an interlayer spacing of 7.5 µm and 15 µm.

6.3.3 Three tracks per layer

The next step towards increased data capacity per layer is to write several tracks in each layer, which corresponds to the same number of revolutions of a spinning disc. In the example given here, three tracks are recorded. As for recording of a spiral track in an optical disc, the three tracks receive the same exposure energy density.

As the interlayer spacing is many Rayleigh lengths, the broad Gaussian profiles of each of the microgratings in one layer are nearly constant over the width of the three tracks in the next layer. Consequently the diffraction efficiency of the three tracks in each layer will be almost equal if the central tracks are equalized.

The tracks in each layer are recorded at the same lateral positions $y = -t, 0, t$ with a track pitch t and an interlayer spacing s of several micrometers. When the tracks in the layer at $z = 0$ are recorded, the normalized exposure of the material is calculated as in (6.19) and yields

$$\gamma_{3\mathsf{T}}(z) = \frac{w_0}{w(z)} \frac{\sum_{m=-1}^{1} \exp\left(-2\,(mt)^2/w^2(z)\right)}{\sum_{m=-1}^{1} \exp\left(-2\,(mt)^2/w_0^2\right)} \,. \tag{6.21}$$

For each track, the bit sequence is supposed to contain logical zeroes and ones with equal possibility, which yields an average amplitude (or fill factor) of 1/2. Assuming a constant material-consumption factor for each layer, the diffraction efficiency of a grating in the j-th layer yields

$$DE_j = \prod_{\ell=1}^{j-1} \left[1 - \frac{1}{2} f_\alpha\Big(b_\ell \cdot \gamma_{3\mathsf{T}}((j-\ell)\,s)\Big)\right]^2 DE(\alpha, b_j) \,. \tag{6.22}$$

With this expression, the exposure schedules are derived as described in Subsection 6.2.1.

Two exposure schedules for 20 layers are displayed in Figure 6.11, which are similar to those obtained with one track per layer. The three tracks per layer are recorded with a track pitch of 0.5 µm and with a relatively large interlayer spacing of 15 µm. With 20 layers, diffraction efficiencies of at most $2 \cdot 10^{-5}$ can be achieved, which yields a poor signal quality at or even below the noise level of blue-sensitive Aprilis media [8]. The achieved diffraction efficiency in 50 layers is 10^{-5}.

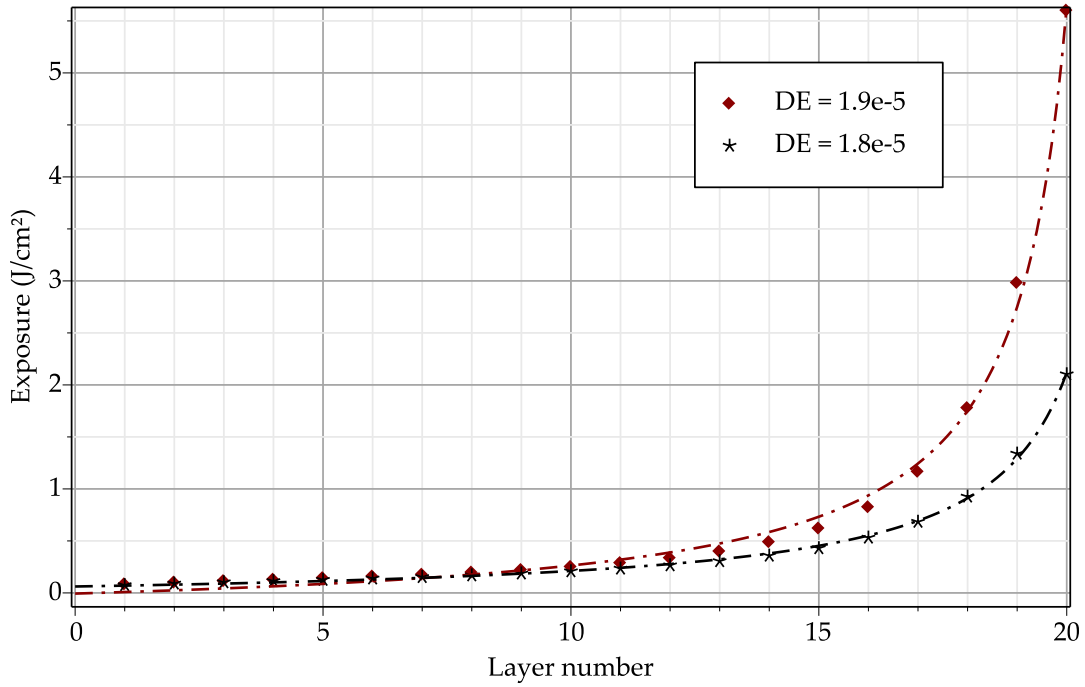

Figure 6.11: Schedules for recording of three tracks in each of 20 layers with two DE values, a track pitch of 0.5 µm, fill factor 1/2 and an interlayer spacing of 15 µm.

Figure 6.12 shows the achievable DE in terms of the number of layers with an interlayer spacing of 7.5 µm, 15 µm and 30 µm, all with a track pitch of 0.5 µm and a fill factor of 1/2. The available DE is smaller than the DE for recording of one track per layer with a corresponding interlayer spacing, see Figure 6.10. By doubling the interlayer spacing, the diffraction efficiency can be almost doubled. Eight layers can have a diffraction efficiency of 10^{-4} at an interlayer spacing of 30 µm.

To ensure a good SNR, a DE of 10^{-2} is required [8], which can only be achieved with a higher refractive index contrast or with a smaller NA. If the NA is reduced from 0.75 to 0.5, the DE of the gratings will get seven times as large with a 2.7-fold interlayer spacing and a 1.6-fold track pitch to compensate for the larger dimensions of the Gaussian beams. These larger dimensions reduce the available data density.

Sparse coding may be used to further improve the SNR. For a fill factor of 20 % with an interlayer spacing of 15 µm, the DE is displayed in Figure 6.12. The achievable DE for four to 20 layers is about five times as large as with a fill factor of 1/2. However, a DE of at least 10^{-3} is only reached for up to four layers.

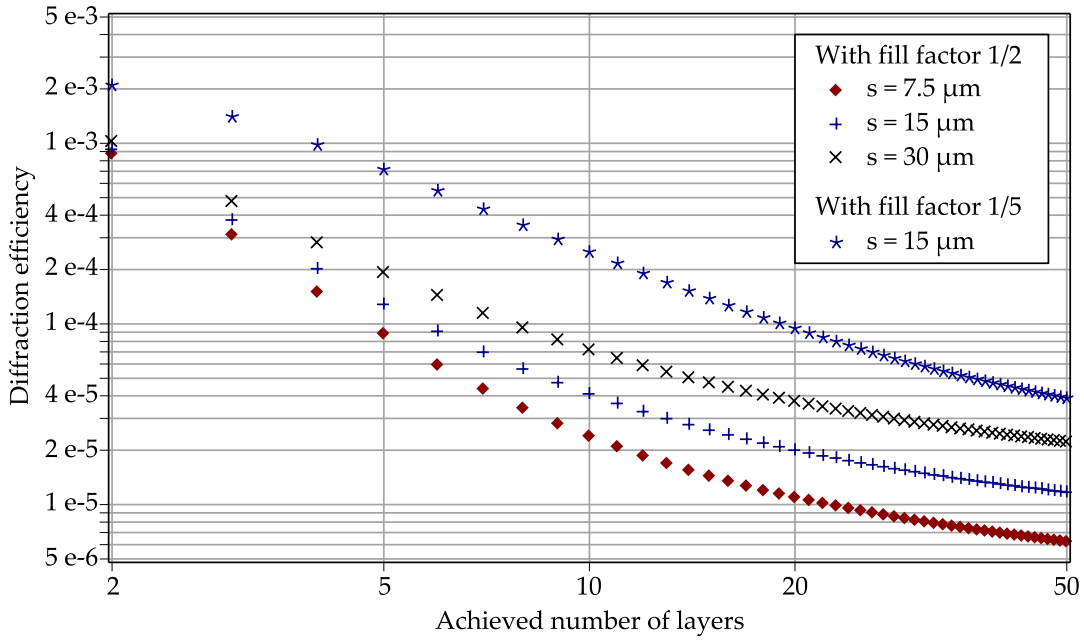

Figure 6.12: Recording three tracks per layer: Available DE in terms of the number of layers with three interlayer spacings , fill factor 1/2 and 1/5 and a track pitch of 0.5 µm.

The above results were calculated with the fast method in Subsection 6.2.1 where a constant material-consumption factor for each layer is assumed. However, these results produce diffraction efficiencies which deviate from the intended value. An example is shown in Figure 6.14 for 10 layers at an interlayer spacing of 15 µm where the DE was set to $3.8 \cdot 10^{-5}$. The diffraction efficiencies of the first few layers are too small. This is partly caused by too large estimates of the DE at low α by (5.12).

With the improved method in Subsection 6.2.2, the diffraction efficiencies are equalized. The exposure schedules are displayed in Figure 6.13, showing that for all 10 layers the exposure energy densities have to be raised. These larger exposure energy densities suggest that the available diffraction efficiencies for each number of layers might be slightly smaller than those shown in Figure 6.12.

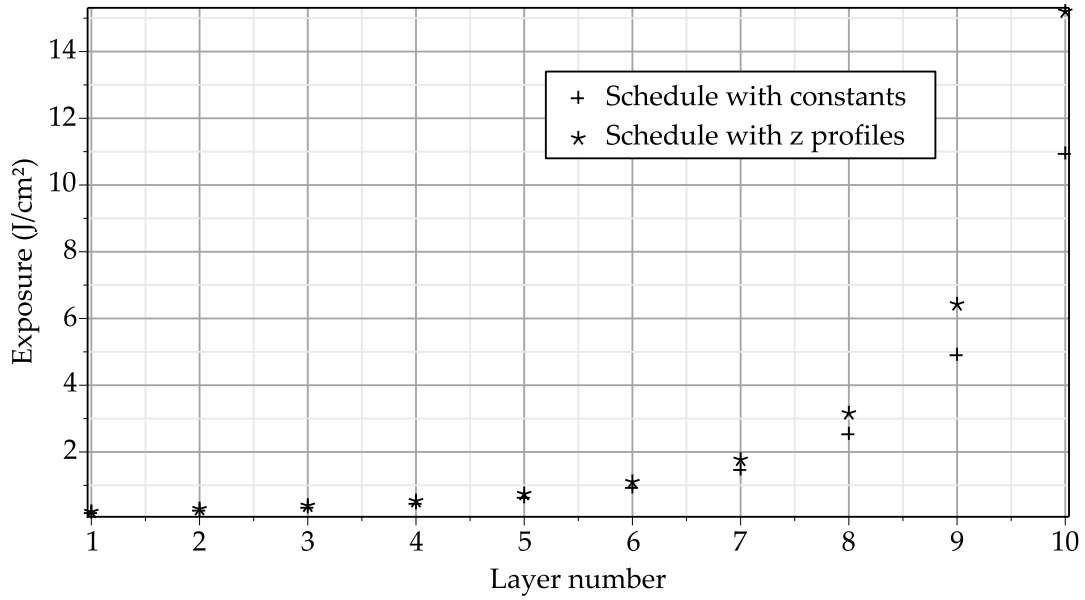

Figure 6.13: Three tracks per layer with 10 layers at an interlayer spacing of 15 µm and $DE = 3.8 \cdot 10^{-5}$: Schedule based on constant material-consumption factors and improved schedule which accounts for their z profiles.

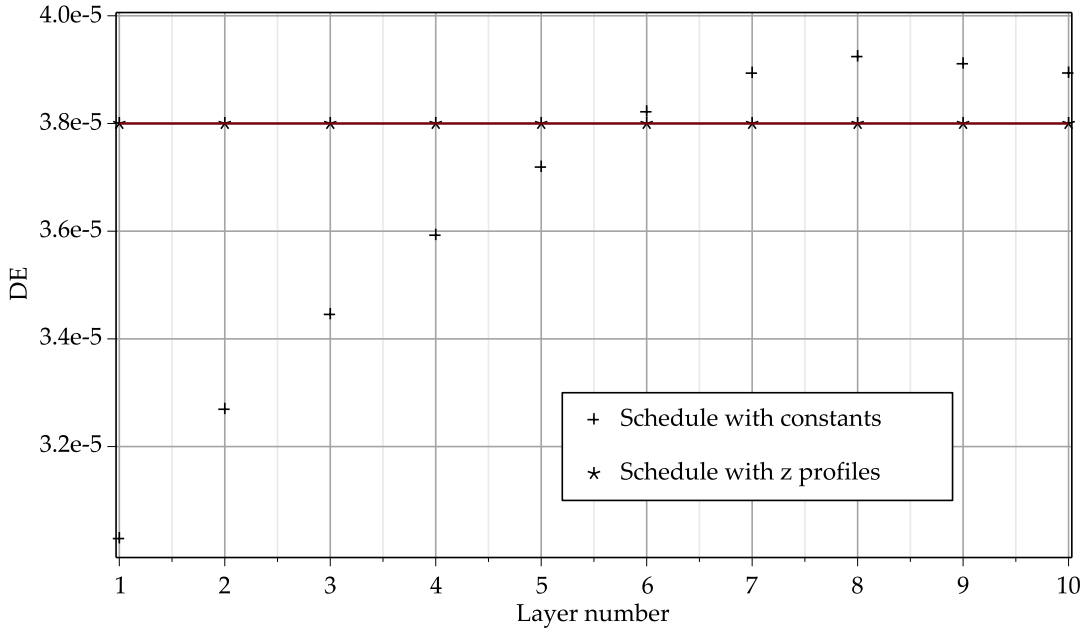

Figure 6.14: Three tracks per layer with 10 layers at an interlayer spacing of 15 µm (Figure 6.13): DE result if the schedule is based on constant material-consumption factors (points), improved schedule reaches $DE = 3.8 \cdot 10^{-5}$ (straight line).

6.3.4 Filled layers of data in linear media

For high-capacity microholographic data storage, multiple layers filled with data should be stored in the photosensitive layer of the disc. In a recording medium with linear behavior, the available capacity of multilayer microholographic data storage is limited, which is analyzed here.

For the calculations, the microgratings are organized in parallel data tracks, which is equivalent to a spiral track in a rotating disc. The track pitch controls the data capacity of each layer but also has an influence on the achievable diffraction efficiency. The tracks are recorded at the lateral positions $y = m\,t$, with a track pitch t and an interlayer spacing s. If a layer is written at $z = 0$, the averaged exposure of the material is

$$\sum_{m=-\infty}^{\infty} \frac{1}{t}\sqrt{\frac{2}{\pi}}\frac{w_0}{w^2(z)} \int_{-t/2}^{t/2}\int_{-\infty}^{\infty} \exp\left(-2\frac{x^2+(y-mt)^2}{w^2(z)}\right) \mathrm{d}x\mathrm{d}y = \sqrt{\frac{\pi}{2}}\frac{w_0}{t}\,. \tag{6.23}$$

As the exposure of the material is independent of the depth position, the achievable diffraction efficiency in multiple layers is not influenced by the interlayer spacing. Hence, the exposure schedules can be computed with the method described in Subsection 6.2.1. The diffraction efficiency of a grating in the j-th layer is

$$DE_j = \left[\prod_{\ell=1}^{j-1}\left(1-\frac{1}{2}f_\alpha\left(b_\ell\cdot\sqrt{\frac{\pi}{2}}\frac{w_0}{t}\right)\right)\right]^2 DE(\alpha, b_j)\,, \tag{6.24}$$

where b_ℓ is proportional to the exposure energy density for the ℓ-th layer, so that $0 \leq b \leq 1$ corresponds to up to 20 J/cm^2. All tracks have an average amplitude (fill factor) of $1/2$, which corresponds to a bit sequence of logical zeroes and ones with equal possibility. The gratings are recorded with a wavelength of 405 nm and $NA = 0.75$ in a material with a refractive index of $n_0 = 1.5$ and an index contrast of $\Delta n = 0.001$.

Figure 6.15 shows recording schedules for various diffraction efficiencies with a track pitch of 0.6 µm. For five layers, the achieved diffraction efficiency is of the order of 10^{-5}. The exposure energy densities of the first layers have to be smaller if the number of layers is larger.

As the material consumption does not depend on the depth position, no gain in diffraction efficiency can be achieved by enlarging the interlayer spacing. The DE can only be improved by the parameters of each layer, such as track pitch and fill factor.

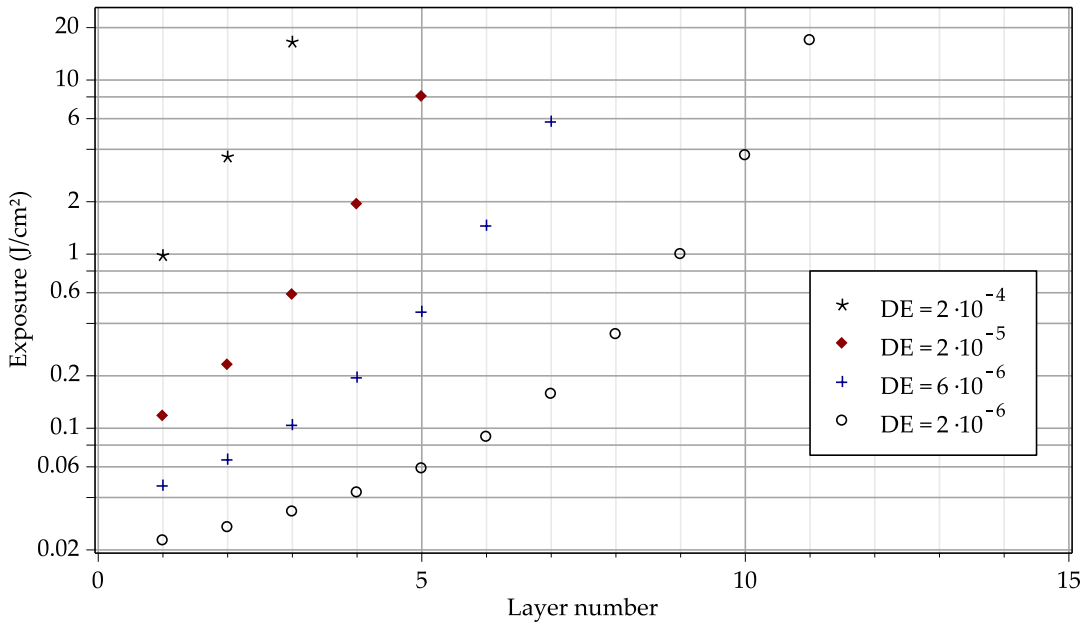

Figure 6.15: Multilayer data storage: Recording schedules for various diffraction efficiencies with a track pitch of 0.6 µm and fill factor 1/2.

Figure 6.16 shows the maximum DE for each number of layers with three different track pitches and a fill factor of 1/2. Five layers with a track pitch of 0.6 µm can have a DE of $3 \cdot 10^{-5}$, while three layers with 0.3 µm track pitch at a DE of $2 \cdot 10^{-4}$ can hold more data. However, the in-track spacing and the track pitch should be at least 0.5 µm to avoid an overlap of adjacent gratings which leads to a decline of the DE [35]. Small exposure energy densities lead to smaller microgratings which may solve this issue.

The DE can be improved by sparse coding, which reduces the material consumption of each layer. This is also displayed in Figure 6.16. A fill factor of 1/5 and a track pitch of 0.6 µm allows four layers with a DE of almost 10^{-3} or seven layers with a DE of $2 \cdot 10^{-4}$. The DE can be improved by a higher index contrast or a smaller NA.

Figure 6.17 summarizes the DE and the capacities which are obtained. The capacities per layer are estimated as follows: A layer with a track pitch of 0.3 µm can contain 25 GB as a Blu-ray disc, 7 GB are available for 0.5 µm and 5 GB for 0.6 µm. With a track pitch of 0.5 µm or 0.6 µm, only 25 GB can be stored with a DE of 10^{-4}. The best trade-off between the capacity and the DE is a five-layer disc with 125 GB. Even this requires a track pitch of 0.3 µm and yields a low DE of $5.5 \cdot 10^{-4}$.

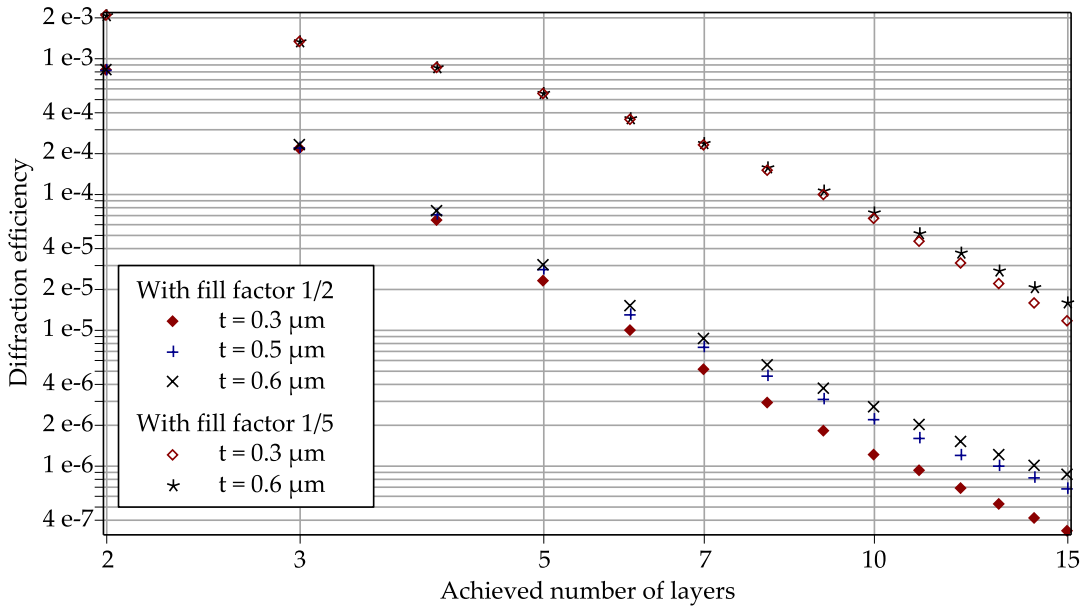

Figure 6.16: Multilayer data storage: Available diffraction efficiency in terms of the number of layers with fill factor 1/2 and three different track pitches and with fill factor 1/5.

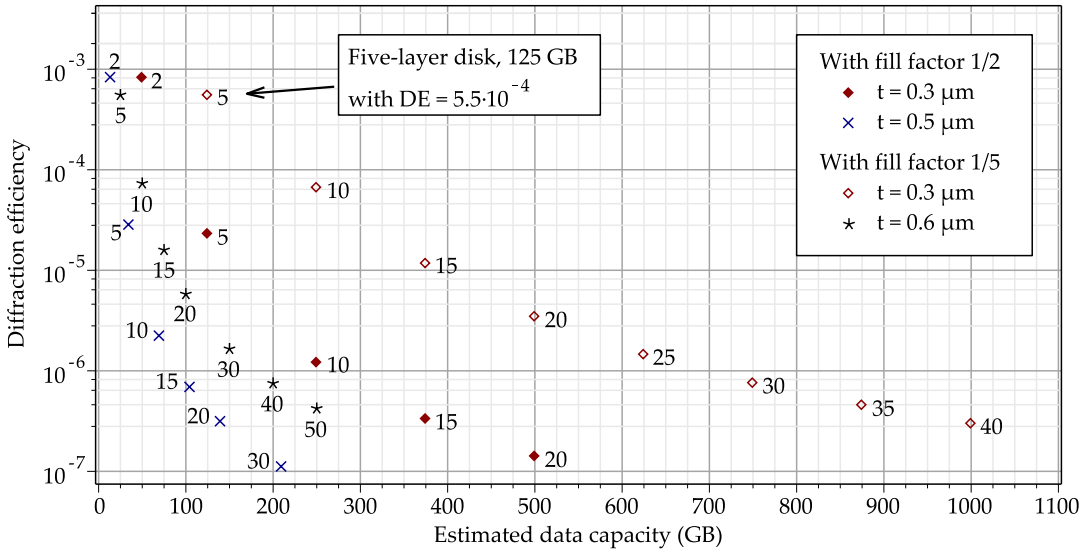

Figure 6.17: Storage capacity and DE for multilayer data storage in a linear recording medium with index contrast of 0.001, with number of layers at each point. Other parameters: wavelength 405 nm, NA = 0.75, refractive index of recording material 1.5.

6.4 Conclusion

This chapter was focused on the prospects of multilayer microholographic data storage in a linear recording medium with saturation. The effect of subsequent recording of gratings or tracks in multiple layers on the material dynamics and the resulting index contrast in each layer were analyzed. Exposure schedules were derived, which yield equal diffraction efficiencies in the layers.

The gratings are recorded with a wavelength of 405 nm and $NA = 0.75$ in a linear recording material with a refractive index of 1.5 and an index contrast of 0.001. With the lowest demands on the storage material, one micrograting in each layer already limits the achievable DE due to the overlap of the gratings in adjacent layers. The diffraction efficiencies are in the range of 10^{-4} to 10^{-3}.

One grating per layer can be recorded with equal DE except for the first few gratings. For data storage with tracks, the outreach of the material consumption into the deeper layers decreases slowly, which is compensated by rising exposure energies. For one track per layer with an interlayer spacing of 7.5 µm, the DE decreases from 10^{-3} for two layers to $3 \cdot 10^{-5}$ for 20 layers. Even with larger spacing, the DE stays below 10^{-3}.

With sparse coding, using an example of bit sequences with 20 % of logical ones, a few layers with a DE of the order of 10^{-3} are obtained. A larger index contrast improves the DE as well. Reducing the NA from 0.75 to 0.5 yields a seven-fold DE. This requires a 2.7-fold interlayer spacing and a 1.6-fold track pitch to compensate for the larger dimensions of the Gaussian beams.

For multilayer data storage, a disc made of a linear storage material with saturation and a maximum index contrast of 0.001 yields low diffraction efficiencies. The best trade-off between the capacity and the DE is a five-layer disc with 125 GB, sparse coding and a DE of $5.5 \cdot 10^{-4}$. Even this requires a track pitch of 0.3 µm.

To cope with material noise, the DE should rather be of the order of 10^{-2} [8]. However, linear recording materials may be used for storage tasks with smaller amounts of data, perhaps with a smaller NA. Multilayer data storage in a square-law material, enabled by a two-photon absorption process, is discussed in the next chapter.

7 Square-law media for multilayer microholographic data storage

The poor performance of linear recording media for multilayer microholographic data storage, as described in Chapter 6, follows from their crucial disadvantage: During exposure of one layer, the other layers receive the same dose of light which is applied to the layer being written in. Figure 7.1 illustrates this: While the first layer is being recorded, the other layers receive the same fluence of (not focused) light as indicated by the dashed lines.

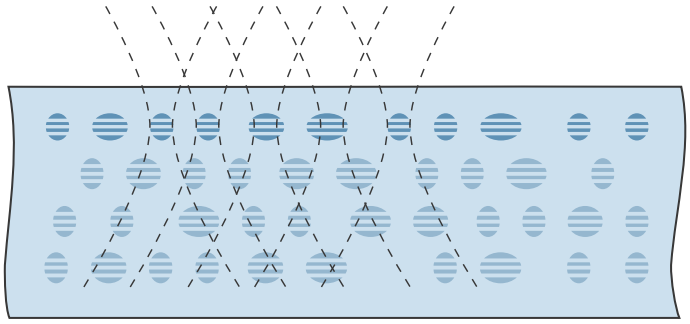

Figure 7.1: While a layer is recorded, diverging beams pass through all layers.

This undesired effect exposes the material with a nearly uniform background. It exploits the photosensitive material so that only a small part of its dynamic range is allocated to each layer. Even if a small number of tracks per layer are stored, the diffraction efficiency is low and can be below the noise level of the storage medium.

For high-capacity volumetric discs with the diameter of a DVD, a nonlinear recording material is required. The material should limit the change of the refractive index to each layer. Quadratic, thresholding and hard clipping material characteristics have been discussed in [85] using small statistics of a few hundred microgratings.

An intensity threshold, where grating formation takes place only in the focal region, would be greatly useful for data storage [85]. However, a linear material with an exposure threshold, which is overcome after the first layer of gratings has been recorded, would not be a solution. The dynamic range would be shared by $N-1$ layers instead of N layers, so the basic drawback of linear materials would remain.

This chapter is focused on square-law media which enable multilayer data storage by constraining the index change closely to each layer. In Section 7.1 the two-photon recording mechanism is introduced, which enables recording of micrograting proportional to the square of the intensity. The most important effects on the dimensions and on the structure and the selectivity of micrograting are outlined.

The prospects of quadratic media for multilayer data storage are analyzed in Section 7.2. Results with different track pitches and interlayer spacings are compared. The chapter ends with recommendations on how to improve the diffraction efficiency for multilayer data storage.

7.1 Micrograting in two-photon recording media

The two-photon recording mechanism is the most promising way to overcome the drawbacks of linear recording. Two-photon absorption (TPA) is a third-order nonlinear optical process [94]. In TPA, the number of photons absorbed is proportional to the square of the intensity of the incident light [83]. In a nonlinear optical material, the applied electric field $\vec{E}$ induces the polarization

$$\vec{P}_{\mathrm{ind}} = \chi^{(1)}\vec{E} + \chi^{(2)}\vec{E}\vec{E} + \chi^{(3)}\vec{E}\vec{E}\vec{E} + \ldots, \tag{7.1}$$

where $\chi^{(j)}$ is the j-th order susceptibility of the medium [95, p. 157ff], in general a $(j+1)$-order tensor. The energy transfer from the electric field to the medium is written as

$$\frac{\mathrm{d}W}{\mathrm{d}t} = \left\langle \vec{E} \cdot \vec{P}_{\mathrm{ind}} \right\rangle . \tag{7.2}$$

The time average $\langle \ldots \rangle$ of the oscillating field eliminates the even-order susceptibilities. Considering only dissipative processes, $\chi^{(1)}$ corresponds to linear absorption,

and nonlinear absorption is described by $\chi^{(3)}$ (two-photon absorption) and $\chi^{(5)}$ (three-photon absorption). The energy transfer rate for absorption of two photons of the same frequency ω yields

$$\frac{\mathrm{d}W}{\mathrm{d}t} = \frac{8\pi^2\omega}{n^2c^2} I^2 \,\mathrm{Im}\left(\chi^{(3)}\right) \,, \tag{7.3}$$

which is proportional to the square of the intensity. Two-photon absorption requires an intensity exceeding 100 MW/cm^2 [83] or even in the GW range [84].

Holography using the two-photon recording mechanism was achieved first with $LiNbO_3$ crystals [96], followed later by photopolymers [97]. Examples for two-photon materials include SU-8 photoresists [98], sol-gel materials [99], and two-photon sensitized fluorescent dye materials [82]. Multi-photon direct laser writing is described in [100]. Direct laser writing with a continuous-wave laser at 532 nm in three different photoresist materials was performed in [101].

Holographic data storage was performed in a new cationic ring-opening polymerization (CROP) material with a two-photon mechanism with a square-law index change and a threshold character. This material can reach a refractive index change of $\Delta n = 3.3 \cdot 10^{-3}$ [84]. The peak light intensity during recording is of the order of 10 GW/cm^2.

Two differences compared to the experimental setup used by Orlic et. al. should be pointed out. Steinberg et. al. [84] use pulsed light at 532 nm and both laser beams come from the same side of the disc. This produces transmission gratings with a larger grating period, which is close to 1 µm in their case. The processes in the material can be largely different depending on the grating period and on the dimensions of the recorded volume gratings.

The microgratings described in this work are reflection gratings, which are recorded with two counterpropagating beams. In a square-law holographic medium, the modulated refractive index is described by

$$n(\vec{r}) = n_0 + \Delta n_{\max} \frac{I^2(\vec{r})}{I^2_{\max}} \,, \tag{7.4}$$

where $\Delta n_{\max}$ denotes the maximum index contrast. With Gaussian beams, the normalized index contrast of the micrograting yields

$$\frac{\Delta n(\vec{r})}{\Delta n_{\max}} = \frac{w_0^4}{w^4(z)} \exp\left(-4\,\frac{x^2+y^2}{w(z)^2}\right) \tag{7.5}$$

with the beam radius $w(z) = w_0\sqrt{1+(z/z_R)^2}$. When a layer is recorded, the averaged exposure of the material is proportional to $1/w^2(z)$. Hence, the material consumption is mostly localized to each layer, which enables multilayer data storage. This is similar to recording of only one grating in a linear recording material, where the exposure is proportional to $1/w^2(z)$ along the optical axis.

The structure of a micrograting in a square-law recording medium is displayed in Figure 7.2. With the envelope of the intensity during recording written as $\widehat{I}(\vec{r})$, the $\lambda/2$ component of the grating structure yields

$$\frac{1}{\pi}\int_0^{2\pi}\frac{\widehat{I}^2(\vec{r})}{I_{\max}^2}\left(\cos^4(u)\right)\cos(2u)\mathrm{d}u = \frac{1}{2}\frac{\widehat{I}^2(\vec{r})}{I_{\max}^2}\,, \tag{7.6}$$

whereas in the linear case

$$\frac{1}{\pi}\int_0^{2\pi}\frac{\widehat{I}(\vec{r})}{I_{\max}}\left(\cos^2(u)\right)\cos(2u)\mathrm{d}u = \frac{1}{2}\frac{\widehat{I}(\vec{r})}{I_{\max}}\,. \tag{7.7}$$

As higher harmonics are not supported in a reflection grating, the relevant part of the micrograting which generates the diffracted field is described by (7.6).

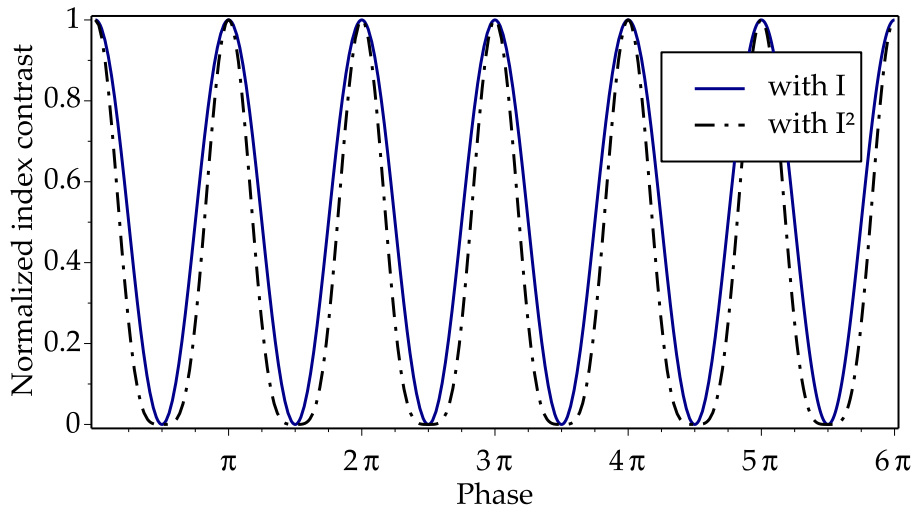

Figure 7.2: Grating structure of a micrograting written in a square-law recording material (dashed) compared to the grating structure in a linear material (solid).

To compute the diffraction of light by these gratings, a factor $\widehat{I}(\vec{r})\,/\,I_{\max}$ is inserted in the diffraction integral in Chapter 4. As in the previous chapters, the recording wavelength is 405 nm, the NA is 0.75 and the refractive index of the recording medium is 1.5. For

confocal readout of a micrograting in a square-law recording material with an index contrast of $\Delta n = 0.001$, the DE yields $3.1 \cdot 10^{-7}$, which is 8.5 times smaller than for a resolution-limited micrograting in Chapter 4. The DE is proportional to $w_0(NA)^4$.

Square-law recording media may also show a saturation effect [83, 84]. In order to estimate the effect of saturation on the DE and on the selectivity of the gratings, the same saturation function as introduced in Chapter 5 is chosen:

$$f_\alpha(\gamma(\vec{r})) = \frac{(1+\alpha)\gamma(\vec{r})}{1+\alpha\,\gamma(\vec{r})} \; . \tag{7.8}$$

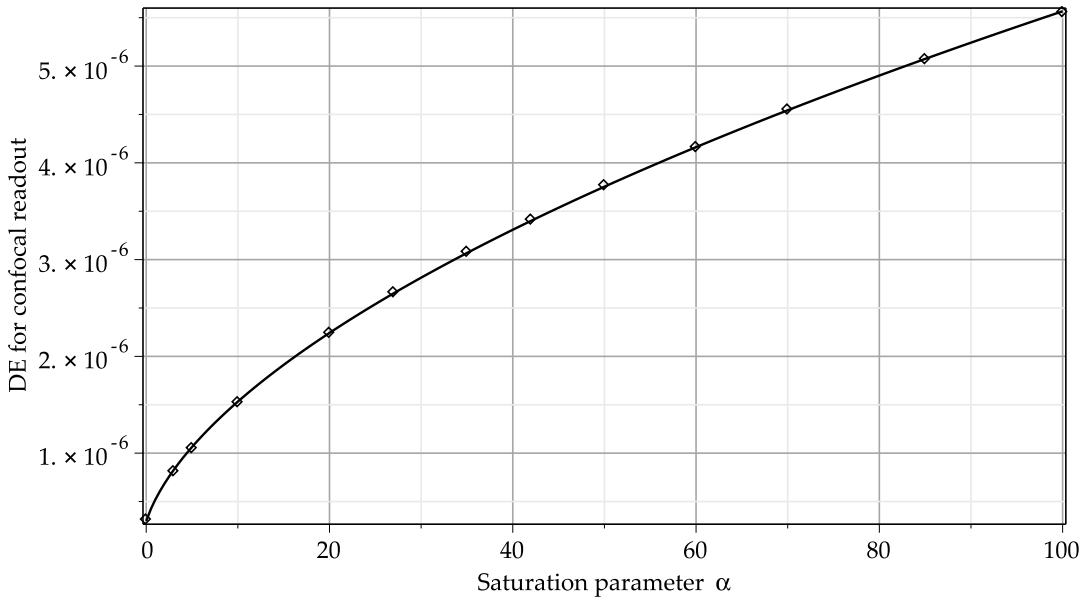

Figure 7.3: DE in terms of the saturation parameter α in a square-law recording medium with an index contrast of 0.001.

The diffraction efficiency in terms of the saturation parameter α is shown in Figure 7.3. It can be described by the empirical function

$$3.95 \cdot 10^{-7}(0.615+\alpha)^{0.573} \; . \tag{7.9}$$

In the range for α from 0 to 100, the DE is of the order of 10^{-7} to 10^{-6}. The depth (FWHM) of the microgratings is the FWHM of the longitudinal profile

$$f_\alpha\left(\frac{w_0^4}{w(z)^4}\right) \; , \tag{7.10}$$

which yields

$$z_{\mathrm{FWHM}} = 2\,z_R\,\sqrt{\sqrt{\alpha+2}-1} \; . \tag{7.11}$$

The effect of saturation on the depth of the micrograting is weaker than for saturation of a linear recording medium. The depth yields 0.33 µm for $\alpha = 0$ and 1.56 µm for $\alpha = 100$. The longitudinal selectivity can be expected to be smaller than these values.

On the basis of (7.11), the wavelength selectivity can be estimated as

$$\lambda_{\mathrm{FWHM}} = \frac{22\ \mathrm{nm}}{\sqrt{\sqrt{\alpha+2}-1}}\ , \tag{7.12}$$

which yields 7.3 nm for $\alpha = 100$.

In a square-law medium, the lateral width and the lateral selectivity of the microgratings are smaller than in a linear medium. At $\alpha = 100$, the effective width x_{eff}, which corresponds to a depletion of the DE to $1/e$, yields 0.17 µm. This together with the shorter depth reduces the overlapping of adjacent gratings and may enable smaller track pitches. However, the small DE requires a stronger index contrast.

7.2 Multilayer data storage in quadratic media

High-capacity microholographic data storage is enabled by storing layers filled with data in the whole photosensitive volume of the disc. The achievable DE and the influence of the track pitch t and the interlayer spacing s are evaluated here. The microgratings are organized in parallel data tracks, placed at the lateral positions $y = mt$, which is equivalent to a spiral track with the same spacing. When a layer is recorded at $z = 0$, the averaged exposure is

$$\sum_{m=-\infty}^{\infty} \frac{1}{t}\frac{2}{\sqrt{\pi}}\frac{w_0^3}{w^4(z)} \int_{-t/2}^{t/2}\int_{-\infty}^{\infty} \exp\left(-4\frac{x^2+(y-mt)^2}{w^2(z)}\right) \mathrm{d}x\mathrm{d}y = \frac{w_0^3\sqrt{\pi}}{2\,t\,w^2(z)}\ . \tag{7.13}$$

The diffraction efficiency of a grating in the j-th layer is

$$DE_j = \left[\prod_{\ell=1}^{j-1}\left(1-\frac{1}{2}f_\alpha\left(b_\ell\,\frac{w_0^3\sqrt{\pi}}{2\,t\,w^2(z)}\right)\right)\right]^2 DE(\alpha, b_j)\ , \tag{7.14}$$

where b_ℓ is proportional to the squared exposure energy density, with $b_\ell = 1$ as the maximum. Using (7.9), the diffraction efficiency factor $DE(\alpha, b_j)$ is

$$DE(\alpha, b_j) = 3.95\cdot 10^{-7}\cdot(0.615+\alpha)^{0.573}\, f_\alpha^2(b_j)\ . \tag{7.15}$$

The exposure schedules are derived as in Subsection 6.2.1.

Figure 7.4 shows the DE which can be achieved depending on the number of layers. Regardless of the track pitch and of the interlayer spacing, the DE is at most $5.6 \cdot 10^{-6}$. This number is limited by saturation of the material and to some part by the overlap of adjacent gratings in the same layer. As only the adjacent layers overlap, the subsequent layers are recorded with nearly equal exposure energy densities, except for the first layers which start at 5 % to 10 % lower energy densities.

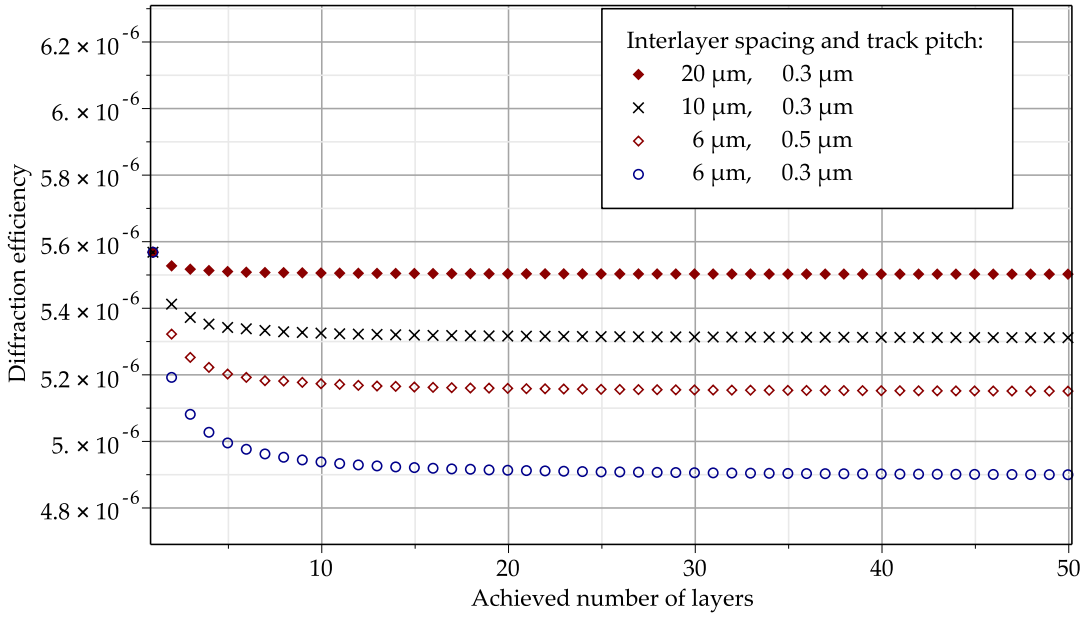

Figure 7.4: DE in terms of the number of recorded layers with maximum saturation parameter $\alpha = 100$ using different track pitches and interlayer spacings.

Figure 7.5 displays the achievable capacities and DE in a square-law medium with a thickness of 300 µm. The capacities per layer are estimated as in Chapter 6: 25 GB as a Blu-ray disc with a track pitch of 0.3 µm and 7 GB for 0.5 µm. The number of layers, which dictates the interlayer spacing, is denoted next to each point.

With more layers and a smaller track pitch, the DE decreases. A storage capacity of one TB can be achieved in 40 layers with an interlayer spacing of 7.5 µm and a track pitch of 0.3 µm. With an index contrast of 0.001, a diffraction efficiency of $5.1 \cdot 10^{-6}$ is achieved. As the DE levels off, the capacity can be scaled by enlarging the thickness of the recording medium and adding more layers. The prospects for a larger DE are explained in the next section.

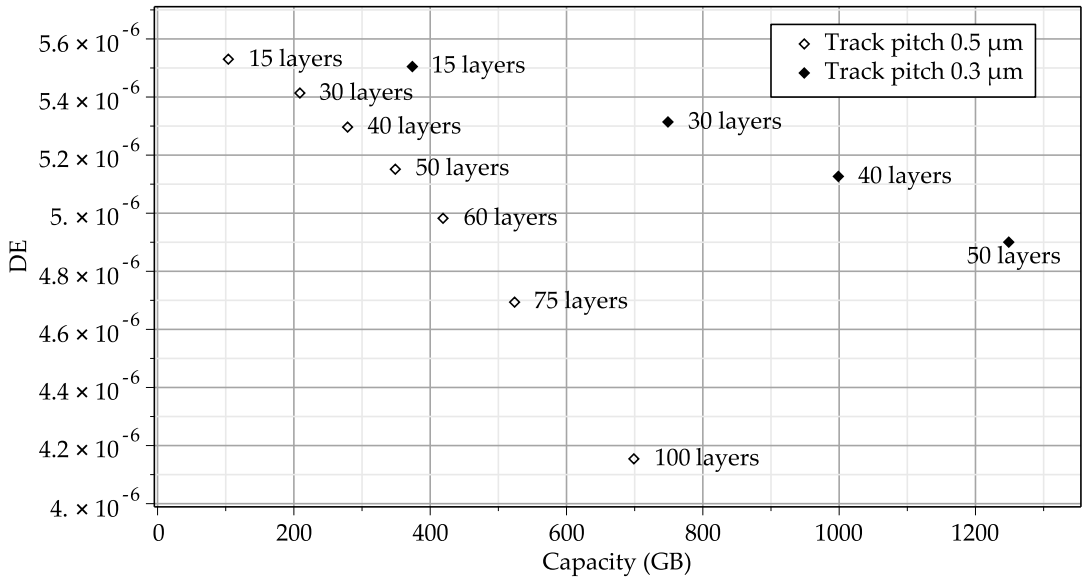

Figure 7.5: Capacity and DE in a square-law recording medium of thickness 300 µm with saturation $\alpha = 100$, $\lambda = 405$ nm, $NA = 0.75$, refractive index 1.5 and $\Delta n = 0.001$.

7.3 Recommendations for multilayer data storage

Due to the small size of micrograting in a square-law medium, even with a saturation effect, the DE should be optimized. To ensure a good signal quality, the DE should be of the order of 10^{-2} [8]. Several ways to improve the DE are described below.

Larger index contrast Δn: The DE is proportional to Δn^2. However, the index contrast of currently available recording materials is limited, for example $\Delta n = 3.3 \cdot 10^{-3}$ in [84]. Index contrasts of the order of 10^{-2} could enhance the DE, but may induce ample scattered light. Recorded layers with a strong index contrast influence the incident wavefronts during readout and may lead to signal errors.

A smaller NA yields larger microgratings with a larger DE. When the NA is changed from 0.75 to 0.5 (with the same wavelength of 405 nm), the grating depth is 2.7 times as large and yields a seven-fold DE. To compensate for the larger dimensions of the gratings, this requires a 2.7-fold interlayer spacing and may need a 1.6-fold track pitch.

Spherical aberration, induced by the thickness of the disc, changes the structure of the gratings and increases their depth. As the DE is roughly proportional to the square of the grating depth, this yields a higher DE, but it requires larger interlayer spacings.

A threshold of the recording material reduces the material consumption in the adjacent layers, which allows a smaller interlayer spacing. The effect on the DE is small as the multilayer DE can only reach the DE of a single grating.

Table 7.1 shows parameter combinations for 1 TB and the available DE for each of the layers. The first line corresponds to 40 layers in a recording layer with a thickness of 300 µm, a track pitch of 0.3 µm and $\Delta n = 0.001$. With $\Delta n = 3.3 \cdot 10^{-3}$ and a NA of 0.5, the DE is improved only to $3.9 \cdot 10^{-4}$ at the expense of a larger interlayer spacing. This low DE is expected to be near the noise level.

Δn	NA	Track pitch	Interlayer spacing and number of layers		Thickness of material	DE
0.001	0.75	0.3 µm	7.5 µm	40	300 µm	$5.1 \cdot 10^{-6}$
0.001	0.75	0.3 µm	3.0 µm	40	120 µm	$3.5 \cdot 10^{-6}$
0.0033	0.50	0.5 µm	20.3 µm	100	2.03 mm	$3.9 \cdot 10^{-4}$
0.045	0.75	0.3 µm	7.5 µm	40	300 µm	$1.0 \cdot 10^{-2}$
0.017	0.50	0.5 µm	20.3 µm	100	2.03 mm	$1.0 \cdot 10^{-2}$
0.0042	0.50 (4)	0.5 µm	81.0 µm	100	8.10 mm	$1.0 \cdot 10^{-2}$
0.0042	0.50 (4)	0.5 µm	32.4 µm	100	3.24 mm	$6.9 \cdot 10^{-3}$

Table 7.1: Parameters and achievable DE for multilayer data storage of one TeraByte in a square-law medium. The number (4) indicates a 4-fold depth of the microgratings.

Without changing the recording parameters and the interlayer spacing, an adequate DE of 10^{-2} requires a high refractive index contrast of 0.045. A realistic index contrast of $4.2 \cdot 10^{-3}$ is achieved with a NA of 0.5 and a four-fold depth of the microgratings enabled by spherical aberration. As these microgratings are larger, a track pitch of 0.5 µm and a capacity of 10 GB per layer are assumed. With an interlayer spacing of 32.4 µm, this yields a DE of $6.9 \cdot 10^{-3}$. The thickness of the storage material is 3.24 mm containing 100 layers. This is much more than the thickness of a DVD and requires a correction of the strong spherical aberration.

All these results are derived on the basis of a saturation of the recording material (7.8) with $\alpha = 100$. Without saturation, the DE loses a factor of at least 10.

Current square-law recording materials yield a low DE with multilayer microholographic data storage. A high capacity in such a disc requires an appropriate combination of the following: a stronger index contrast, a technique to suppress material noise effectively or a larger thickness of the recording material (3 mm) with spherical aberration correction. The gratings should be stored with a smaller data density per layer and a larger grating depth using a smaller NA and a constant spherical aberration.

7.4 Conclusion

This chapter was focused on the prospects of multilayer microholographic data storage in a square-law recording medium, enabled by two-photon absorption. The properties of a micrograting in such a material, including the effect of moderate saturation, were analyzed. To evaluate the prospects of two-photon media for multilayer data storage, exposure schedules for equal diffraction efficiencies were derived.

The micrograting in a square-law medium is smaller than in a linear recording medium, which leads to a smaller DE. Without saturation, the depth (FWHM) of the grating is 0.33 µm. With the saturation function of Chapter 6 and $\alpha = 100$, a grating depth of 1.56 µm, a spectral FWHM of 7.3 nm, an effective width of 0.17 µm and a DE of $5.5 \cdot 10^{-6}$ are obtained.

The gratings are recorded with a wavelength of 405 nm and a NA of 0.75. In a material with an index contrast of 0.001 and moderate saturation, the achieved DE for multilayer data storage is of the order of 10^{-6}. The DE can be improved by a larger index contrast.

However, to reach a DE of 10^{-2}, the depth of the microgratings should be increased by using a smaller NA or by constant spherical aberration. To store 40 layers, the recording layer must have a thickness of roughly three millimeters, which requires spherical aberration correction. A technique to suppress material noise effectively could relax the requirement for high DE and may allow a smaller thickness.

8 Conclusion

Microholographic data storage has the potential for storing high data capacities in a transparent disc. As further research is needed, two tasks were addressed within the scope of this thesis. The first task was to analyze the influence of saturation of the recording material on the diffraction properties of microgratings in linear and quadratic recording media. The second task was focused on multilayer microholographic data storage, the material resources and the prospects of the two material types for high data capacities. The results suggest that future research should focus on volumetric data storage in two-photon media.

For modeling the diffraction of light by volumetrically localized gratings, a method was developed. It has the advantage of being solved analytically in two dimensions, limiting the numerical effort to the longitudinal axis. Featuring good agreement with the results of the 3D integral by first-order Born approximation, it has been proven as an efficient tool for investigations on microgratings. With some approximations, the main features of the grating profiles in a saturating recording material were included. Applied to expressions involving Gaussian beams, it also facilitates modeling the diffraction on more arbitrary volumetrically localized structures.

The diffraction efficiency (DE) was investigated as a function of both lateral and longitudinal scan position, which showed good agreement with experimental results. In a linear medium with saturation, the gratings are localized with smaller dimensions compared to their real size. Gratings with a depth (FWHM) of 10 µm have an effective depth (FWHM of the DE in terms of longitudinal readout position) below 3 µm, enabled by Bragg diffraction. With an index contrast of 0.001, the DE is of the order of 10^{-3}.

To assess the potential of wavelength multiplexing, which can further enhance the capacity of the storage system, the DE of the microgratings was calculated in terms

of the dependence on the readout wavelength. Larger gratings due to saturation of the recording material have a better spectral selectivity. However, the prospects of wavelength multiplexing are limited, as any multiplexing method which involves the storage of several microgratings at the same position is limited by the resources of the recording material.

The spectral analysis also provides an insight into the diffraction effects which take place. For the resolution-limited microgratings in a linear medium, the results reveal a shift of the Bragg angle at smaller wavelengths, which is supported by the broad angular spectrum of the high-NA beam and the small grating. This effect is weaker for the larger gratings with saturation of the recording material.

The prospects of multilayer microholographic data storage in linear recording media were analyzed. To compute recording schedules for equal diffraction efficiencies in multiple layers, an efficient method was devised which is suitable for the partially overlapping gratings due to shift multiplexing. The results clearly confirm that linear recording media are not suitable for high-capacity data storage. The best trade-off is a disc with 125 GB in five layers with a track pitch of 0.3 µm, which yields a low DE of $5.5 \cdot 10^{-4}$ if the index contrast is 0.001. However, these materials might be useful for storage tasks with smaller amounts of data, such as tamper-proof labels.

Square-law media with a two-photon recording mechanism enable multilayer data storage by constraining the index change to each layer. The microgratings are smaller than in a linear recording medium, which leads to a smaller DE. With an index contrast of 0.001 and moderate saturation, the DE is of the order of 10^{-6}, which can be expected to be below the noise level of the recording material.

The low DE may not be improved solely by increasing the index contrast. Data layers with an index contrast of the order of 10^{-2}, which yields a DE of 10^{-2}, would induce ample scattering and modify the incident wavefronts, leading to detection errors. The micrograting depth has to be increased by using a smaller NA or by constant spherical aberration, which requires an unfavorably large thickness of the recording material.

9 Outlook

There is still a lot to be done before microholographic data storage may enter the market. A step forward was made by E. Dietz and S. Frohmann [7, 8] with several developments of the media tester and the disc drive. In experiments, they demonstrated the recording and readout of the strongly localized reflection gratings.

With mathematical modeling, this work provides insight into the diffraction effects in microgratings and predictions concerning the feasibility of high-capacity data storage in two-photon recording media.

Recently, Steinberg et. al. demonstrated multilayer microholographic recording in two types of two-photon media, a rewritable lithium tantalate crystal [83] and a cationic ring-opening (CROP) photopolymer with a refractive index contrast of $3.3 \cdot 10^{-3}$ [84]. The recorded transmission gratings are larger, with a width of 1.4 µm. For readout, they used heterodyne detection, which largely reduced the noise level. To enable high data capacities, further research should focus on recording smaller reflection gratings in two-photon media.

The results in this work reveal that the DE of microgratings in a square-law medium is only of the order of 10^{-6}. For linear recording materials, an adequate diffraction efficiency which can cope with the material noise is of the order of 10^{-2} [8]. The noise level of CROP media with a square-law recording mechanism is expected to be similar to that in linear materials, $10^{-5} - 10^{-4}$, if the noise is induced mainly by volume scattering and by the inhomogeneities of the material.

The weak diffraction efficiency of the strongly localized microgratings in two-photon media is the main problem which remains to be solved. Different ways to tackle this are summarized below.

Larger micrograting

To improve the low DE of micrograting written with high-NA beams in a square-law recording material, the gratings have to be enlarged. The results in this work reveal that the diffraction efficiency is sufficient with a smaller NA of 0.5 and a four-fold depth of the micrograting, which may be enabled by constant spherical aberration which is the same in every layer.

Micrograting with spherical aberration have a more complex structure and a larger effective volume. As emphasized by E. Dietz in [7], these larger gratings can be advantageous for data storage. Having more grating periods, they show a higher DE compared to gratings without aberration. For the same reason, the wavelength selectivity of these larger micrograting could be better.

Large thickness of the recording material

With these settings however, the thickness of the material must be 3 mm to store 40 layers with 25 GB per layer. Shrinkage due to polymerization and a low stability of such a disc may prohibit such a thick recording layer.

By wavelength multiplexing, the thickness of the recording layer can hardly be reduced. As the material resources are shared by the gratings in the same volume, multiplexed gratings would yield a smaller DE.

Adaptive spherical aberration correction

A recording material with a large thickness of a millimeter or more requires adaptive correction of the strong spherical aberration, which must be designed small enough to fit in an optical pickup.

Even with thinner layers, a variation of the thickness may occur both within each disc and between different discs. A change of the optical thickness may be induced by shrinkage, by global changes of the refractive index during recording or due to aging. Adaptive correction of the spherical aberration relaxes the tolerances for thickness variation.

Correction for spherical aberration plays a crucial role for the reliability of the read-out process. When the photopolymer has a different thickness, for example due to shrinkage, the corrections of the two objectives may not properly match. By Bragg

mismatch, this leads to a depletion of the DE and may induce signal errors. Similar results may occur if the aberration of the beam does not match the aberration of the grating. Active correction of the aberration during readout can compensate for these effects.

Reducing material noise

Material noise remains a crucial problem of current photopolymer materials, which limits the detection of gratings with a small DE. Lower noise levels would relax the requirement for high DE, which allows smaller gratings and a smaller thickness of the recording layer. To achieve this aim, either the material has to be designed in a way which yields lower noise levels, or a technique should be implemented which can suppress material noise effectively during detection.

When the dimensions of the microgratings can be reduced and a good signal quality is achieved, a few technical questions will remain. The data rate during readout should be improved to comply with the requirements for the scope of application. Another key question, which is essential for the mass production of optical discs, is how the recording time per disc can be reduced.

BIBLIOGRAPHY

[1] Kazuo Goda and Masaru Kitsuregawa. The history of storage systems. *Proc. IEEE* 100(Special Centennial Issue):1433–1440, 2012.

[2] Economist. Special report: Managing information. All too much – Monstrous amounts of data. Online, Feb 25 2010. At http://www.economist.com/node/15557421, accessed on 02/05/2014.

[3] Economist. Special report: Managing information. Data, data everywhere – Information has gone from scarce to superabundant. Online, Feb 25 2010. At http://www.economist.com/node/15557443, accessed on 02/05/2014.

[4] Hans B. Peek. The emergence of the compact disc. *IEEE Commun. Mag.* 48(1):10–17, 2010.

[5] H. J. Eichler, P. Kuemmel, et al. High-density disk storage by multiplexed microholograms. *IEEE J. Select. Topics Quantum Electron.* 4(5):840 –848, Sep/Oct 1998.

[6] Susanna Orlic, Jens Rass, et al. Multilayer recording in microholographic data storage. *J. Opt.* 14(7):072401, 2012.

[7] Enrico Dietz. *Dreidimensionale optische Datenspeicherung am Auflösungslimit*. Dissertation, Technische Universität Berlin, 2011.

[8] Sven Frohmann. *Einsatz fotosensitiver organischer Materialien für die mikroholografische Datenspeicherung*. Dissertation, Technische Universität Berlin, 2012.

[9] Wen-Shing Sun, Kun-Di Liu, et al. Laser expander design of highly efficient Blu-ray disc pickup head. *Opt. Express* 17(4):2235–2246, Feb 2009.

[10] Masud Mansuripur. *The Physical Principles of Magneto-optical Recording*. Cambridge University Press, Cambridge, 1995.

[11] Erwin R Meinders. *Optical data storage: phase-change media and recording*, volume 4 of *Philips Research Book Series*. Springer, 2006.

[12] Kees Schep, Bert Stek, et al. Format description and evaluation of the 22.5 GB digital-video-recording disc. *Jpn. J. Appl. Phys.* 40(3S):1813, 2001.

[13] Isao Ichimura, Fumisada Maeda, et al. Optical disk recording using a GaN blue-violet laser diode. *Jpn. J. Appl. Phys.* 39(2S):937, 2000.

[14] Takeharu Asano, Motonubu Takeya, et al. Over 100-mW blue-violet laser diodes for Blu-ray disc system. *Proc. SPIE* 5365:297–305, 2004.

[15] Ryuichi Katayama and Yuichi Komatsu. Blue/DVD/CD compatible optical head. *Appl. Opt.* 47(22):4045–4054, Aug 2008.

[16] Pierre H. Woerlee, Wim Koppers, et al. Format of an 8.5-GB double-layer DVD recordable disc. *Proc. SPIE* 5380:15–20, 2004.

[17] Fung-Hsu Wu, Han-Ping D. Shieh, et al. Performance of a write-once multilayer optical disk that uses transparent recording material with an optical switching layer. *Appl. Opt.* 43(29):5498–5502, Oct 2004.

[18] Hiroyasu Inoue, Kouji Mishima, et al. Inorganic write-once disc for high speed recording. *Jpn. J. Appl. Phys.* 42(2S):1059, 2003.

[19] Koji Mishima, Daisuke Yoshitoku, et al. 150 GB 6-layer write once disc for blu-ray disc system. *Proc. SPIE* 6282:62820I–62820I–11, 2007.

[20] Hiroshi Shingai, Tatsuya Kato, et al. Triple-layer rewritable disc with Sb-based phase-change material. *Jpn. J. Appl. Phys.* 49(8S2):08KG02, 2010.

[21] Sony Corp., Panasonic Corp. Archival Disc standard formulated for professional-use next-generation optical discs. Online, Mar 10 2014. http://www.sony.net/SonyInfo/News/Press/201403/14-0310E/, accessed on 12/03/2014.

[22] Mark M. Wang and Sadik C. Esener. Three-dimensional optical data storage in a fluorescent dye-doped photopolymer. *Appl. Opt.* 39(11):1826–1834, Apr 2000.

[23] Xiangping Li, James W. M. Chon, et al. Rewritable polarization-encoded multilayer data storage in 2,5-dimethyl-4-(p-nitrophenylazo)anisole doped polymer. *Opt. Lett.* 32(3):277–279, Feb 2007.

[24] Peter Zijlstra, James W. M. Chon, and Min Gu. Five-dimensional optical record-

ing mediated by surface plasmons in gold nanorods. *Nature* 459(7245):410–413, May 2009.

[25] Masud Mansuripur, Armis R. Zakharian, et al. Plasmonic nano-structures for optical data storage. *Opt. Express* 17(16):14001–14014, Aug 2009.

[26] Jari Lindberg. Mathematical concepts of optical superresolution. *J. Opt.* 14(8):083001, 2012.

[27] Chubing Peng. Superresolution near-field readout in phase-change optical disk data storage. *Appl. Opt.* 40(23):3922–3931, Aug 2001.

[28] Jan Grochmalicki and Roy Pike. Superresolution for digital versatile discs (DVD's). *Appl. Opt.* 39(34):6341–6349, Dec 2000.

[29] Xiangping Li, Yaoyu Cao, and Min Gu. Superresolution-focal-volume induced 3.0 Tbytes/disk capacity by focusing a radially polarized beam. *Opt. Lett.* 36(13):2510–2512, Jul 2011.

[30] Ed Walker, Alexander Dvornikov, et al. Toward Terabyte two-photon 3D disk. *Opt. Express* 15(19):12264–12276, Sep 2007.

[31] Ed Walker, Alexander Dvornikov, et al. Terabyte recorded in two-photon 3D disk. *Appl. Opt.* 47(22):4133–4139, Aug 2008.

[32] Susanna Orlic, Steffen Ulm, and Hans J. Eichler. 3D bit-oriented optical storage in photopolymers. *J. Opt. A: Pure Appl. Opt.* 3(1):72, 2001.

[33] Robert R. McLeod, Andrew J. Daiber, et al. Microholographic multilayer optical disk data storage. *Appl. Opt.* 44(16):3197–3207, Jun 2005.

[34] Kimihiro Saito and Seiji Kobayashi. Analysis of micro-reflector 3D optical disc recording. *Proc. SPIE* 6282:628213, 2007.

[35] Susanna Orlic, Enrico Dietz, et al. Resolution-limited optical recording in 3D. *Opt. Express* 19(17):16096–16105, Aug 2011.

[36] Susanna Orlic, Enrico Dietz, et al. Optical investigation of photopolymer systems for microholographic storage. *J. Opt. A: Pure Appl. Opt.* 11(2):024014, 2009.

[37] Michael R Gleeson and John T Sheridan. A review of the modelling of free-

radical photopolymerization in the formation of holographic gratings. *J. Opt. A: Pure Appl. Opt.* 11(2):024008, 2009.

[38] John V. Kelly, Feidhlim T. O'Neill, et al. Holographic photopolymer materials: nonlocal polymerization-driven diffusion under nonideal kinetic conditions. *J. Opt. Soc. Am. B* 22(2):407–416, Feb 2005.

[39] Rosa Fuentes, Elena Fernández, et al. Study of reflection gratings recorded in polyvinyl alcohol/acrylamide-based photopolymer. *Appl. Opt.* 48(34):6553–6557, Dec 2009.

[40] Jinxin Guo, Michael R Gleeson, and John T Sheridan. A review of the optimisation of photopolymer materials for holographic data storage. *Physics Research International* vol. 2012:Article ID 803439, May 2012.

[41] Cristian Neipp, Sergi Gallego, et al. First-harmonic diffusion-based model applied to a polyvinyl-alcohol–acrylamide-based photopolymer. *J. Opt. Soc. Am. B* 20(10):2052–2060, Oct 2003.

[42] Izabela Naydenova, Raghavendra Jallapuram, et al. Investigation of the diffusion processes in a self-processing acrylamide-based photopolymer system. *Appl. Opt.* 43(14):2900–2905, May 2004.

[43] Chunhe Zhao, Jian Liu, et al. Shrinkage-corrected volume holograms based on photopolymeric phase media for surface-normal optical interconnects. *Appl. Phys. Lett.* 71(11):1464–1466, 1997.

[44] David A. Waldman, Christopher J. Butler, and Daniel H. Raguin. CROP holographic storage media for optical data storage greater than 100 bits/μm^2. *Proc. SPIE* 5216:10–25, 2003.

[45] Ryuichi Katayama and Shin Tominaga. Proposal for rewritable microholographic recording using polarization-sensitive materials. *Jpn. J. Appl. Phys.* 51(8S2):08JD04, 2012.

[46] P. Várhegyi, Á. Kerekes, et al. Saturation effect in azobenzene polymers used for polarization holography. *Appl. Phys. B: Lasers Opt.* 76(4):397–402, 2003.

[47] R. R. A. Syms. *Practical volume holography*. Oxford engineering science series. Clarendon Press, 1990.

[48] Herwig Kogelnik. Coupled wave theory for thick hologram gratings. *The Bell system technical journal* 48(9):2909, 1969.

[49] T. K. Gaylord and M. G. Moharam. Analysis and applications of optical diffraction by gratings. *Proc. IEEE* 73(5):894 – 937, May 1985.

[50] Christian Müller. *Herstellung und Analyse Photonischer Raumgitter für diffraktiv-optische Abbildungen*. Dissertation, Technische Universität Berlin, 2010.

[51] Christiaan Huygens. *Traité de la lumière - avec un Discours de la cause de la pesanteur*. Leyden: Pieter van der Aa, Freuburg i.B., 1690.

[52] Susanna Orlic-Elschner. *Microholographic volume gratings for optical data storage*. Dissertation, Technische Universität Berlin, 2003.

[53] Balázs Gombkötő, Pál Koppa, et al. Computer simulation of reflective volume grating holographic data storage. *J. Opt. Soc. Am. A* 24(7):2075–2081, Jul 2007.

[54] Allen Taflove. *Computational Electrodynamics: The Finite-Difference Time-Domain Method*. The Artech House antenna library. Artech House Inc., 1995.

[55] Kane Yee. Numerical solution of initial boundary value problems involving Maxwell's equations in isotropic media. *IEEE Trans. Antennas Propagat.* 14(3):302–307, 1966.

[56] Frank Ihlenburg and Ivo Babuška. Dispersion analysis and error estimation of Galerkin finite element methods for the Helmholtz equation. *Int. J. Numer. Meth. Eng.* 38(22):3745–3774, 1995.

[57] Hiroyuki Ichikawa and Toshihiko Baba. Efficiency enhancement in a light-emitting diode with a two-dimensional surface grating photonic crystal. *Appl. Phys. Lett.* 84(4):457–459, 2004.

[58] Ardavan F. Oskooi, David Roundy, et al. Meep: A flexible free-software package for electromagnetic simulations by the FDTD method. *Computer Physics Communications* 181(3):687 – 702, 2010.

[59] Jo-Yu Wu and R. Lee. The advantages of triangular and tetrahedral edge elements for electromagnetic modeling with the finite-element method. *IEEE Trans. Antennas Propagat.* 45(9):1431–1437, Sep 1997.

[60] Colin J. R. Sheppard and Saiedeh Saghafi. Beam modes beyond the paraxial approximation: A scalar treatment. *Phys. Rev. A* 57(4):2971–2979, Apr 1998.

[61] H. Laabs. Propagation of Hermite-Gaussian beams beyond the paraxial approximation. *Opt. Commun.* 147(1-3):1 – 4, 1998.

[62] Colin J. R. Sheppard. High-aperture beams. *J. Opt. Soc. Am. A* 18(7):1579–1587, Jul 2001.

[63] Govind P. Agrawal and Deva N. Pattanayak. Gaussian beam propagation beyond the paraxial approximation. *J. Opt. Soc. Am.* 69(4):575–578, Apr 1979.

[64] Marc Couture and Pierre-A. Belanger. From Gaussian beam to complex-source-point spherical wave. *Phys. Rev. A* 24:355–359, Jul 1981.

[65] M. Mansuripur. Distribution of light at and near the focus of high-numerical-aperture objectives. *J. Opt. Soc. Am. A* 3(12):2086–2093, Dec 1986.

[66] James E. Harvey. Fourier treatment of near-field scalar diffraction theory. *Am. J. Phys.* 47(11):974–980, 1979.

[67] Joseph W. Goodman. *Introduction To Fourier Optics*. McGraw-Hill, 2nd edition, 1996.

[68] Zsolt Nagy, Pál Koppa, et al. Modeling of multilayer microholographic data storage. *Appl. Opt.* 46(5):753–761, Feb 2007.

[69] Arthur S. van de Nes, J. J. M. Braat, and S. F. Pereira. High-density optical data storage. *Rep. Prog. Phys.* 69(8):2323, 2006.

[70] Julius Adams Stratton and L. J. Chu. Diffraction theory of electromagnetic waves. *Phys. Rev.* 56:99–107, Jul 1939.

[71] Hans Severin. Zur Theorie der Beugung elektromagnetischer Wellen. *Zeitschrift f. Physik A Hadrons and Nuclei* 129:426–439, 1951.

[72] V. I. Tsoy and Leonid A. Melnikov. The use of Kirchhoff approach for the cal-

culation of the near field amplitudes of electromagnetic field. *Opt. Commun.* 256(1-3):1 – 9, 2005.

[73] John David Jackson. *Klassische Elektrodynamik*. Walter de Gruyter, Berlin, 4. Auflage 2006.

[74] R. T. Ingwall and D. A. Waldman. Photopolymer systems. In Hans J. Coufal, Demetri Psaltis, and Glenn T. Sincerbox, editors, *Holographic Data Storage (Springer Series in Optical Sciences)*, pages 171–198. Springer, 1 edition, 2000.

[75] L. Dhar, M. G. Schnoes, et al. Photopolymers for digital holographic data storage. In Hans J. Coufal, Demetri Psaltis, and Glenn T. Sincerbox, editors, *Holographic Data Storage (Springer Series in Optical Sciences)*, pages 199–208. Springer, 1 edition, 2000.

[76] Fai H. Mok, Geoffrey W. Burr, and Demetri Psaltis. System metric for holographic memory systems. *Opt. Lett.* 21(12):896–898, Jun 1996.

[77] Daniela Grothe and Susanna Orlic. Modeling the diffraction efficiency of holographic microgratings. *J. Opt.* 15(5):052401, 2013.

[78] Peter Atkins and Julio de Paula. *Physikalische Chemie*. Wiley-VCH, 4. edition, 4. Aufl. 2008.

[79] J. R. Lawrence, F. T. O'Neill, and John T. Sheridan. Adjusted intensity nonlocal diffusion model of photopolymer grating formation. *J. Opt. Soc. Am. B* 19(4):621–629, Apr 2002.

[80] J. T. Sheridan and J. R. Lawrence. Nonlocal-response diffusion model of holographic recording in photopolymer. *J. Opt. Soc. Am. A* 17(6):1108–1114, 2000.

[81] Sabino Piazzolla and B. Keith Jenkins. Holographic grating formation in photopolymers. *Opt. Lett.* 21(14):1075–1077, Jul 1996.

[82] M. Akiba, E. Goto-Takahashi, et al. Two-photon sensitized recording materials for multilayer optical disk. *Proc. SPIE* 7730:773018, 2010.

[83] Ilya Sh. Steinberg, Yury Shepetkin, and Andrey Belikov. Multilayer microholographic optical data storage with two-photon recording. *Jpn. J. Appl. Phys.* 52(9S2):09LD05, 2013.

[84] Ilya Sh. Steinberg, E. V. Vasilyev, and A. Yu. Belikov. Multilayer two-photon recording of microholograms in cationic ring-opening polymerization material. *J. Opt.* 15(10):105403, 2013.

[85] Balázs Gombkötő, Zsolt Nagy, et al. Modeling high density microholographic data storage: Using linear, quadratic, thresholding and hard clipping material characteristics. *Opt. Commun.* 281(17):4261 – 4267, 2008.

[86] Victor Ostroverkhov, Brian L. Lawrence, et al. Micro-holographic storage and threshold holographic recording materials. *Jpn. J. Appl. Phys.* 48(3S1):03A035, 2009.

[87] Claire Gu, Yuan Xu, et al. Applications of photorefractive materials in information storage, processing and communication. *Optical Materials* 23(1–2):219–227, 2003. Proceedings of the 8th International Conference on Electronic Materials, IUMRS-ICEM 2002.

[88] Demetri Psaltis, David Brady, and Kelvin Wagner. Adaptive optical networks using photorefractive crystals. *Appl. Opt.* 27(9):1752–1759, May 1988.

[89] George Barbastathis, Michael Levene, and Demetri Psaltis. Shift multiplexing with spherical reference waves. *Appl. Opt.* 35(14):2403–2417, May 1996.

[90] Xiaosu Ma, Qingsheng He, et al. Exposure-schedule study of uniform diffraction efficiency for DSSM holographic storage. *Opt. Express* 12(6):984–989, Mar 2004.

[91] Allen Pu, Kevin Curtis, and Demetri Psaltis. Exposure schedule for multiplexing holograms in photopolymer films. *Opt. Eng.* 35(10):2824–2829, 1996.

[92] Qianli Zhai, Shiquan Tao, et al. Investigation on mechanism of multiple holographic recording with uniform diffraction efficiency in photopolymers. *Opt. Express* 17(13):10871–10880, Jun 2009.

[93] Elena Fernández, Manuel Ortuño, et al. Comparison of peristrophic multiplexing and a combination of angular and peristrophic holographic multiplexing in a thick PVA/acrylamide photopolymer for data storage. *Appl. Opt.* 46(22):5368–5373, Aug 2007.

[94] Mikhail Drobizhev, Aliaksandr Karotki, et al. Dendrimer molecules with record large two-photon absorption cross section. *Opt. Lett.* 26(14):1081–1083, Jul 2001.

[95] Kwang-Sup Lee, editor. *Polymers for Photonics Applications II: Nonlinear Optical, Photorefractive and Two-Photon Absorption Polymers*, volume 161 of *Advances in Polymer Science*. Springer Berlin, 2003. ISBN 3-540-43157-8.

[96] D. von der Linde, A. M. Glass, and K. F. Rodgers. Multiphoton photorefractive processes for optical storage in $LiNbO_3$. *Appl. Phys. Lett.* 25(3):155–157, 1974.

[97] S. M. Kirkpatrick, J. W. Baur, et al. Holographic recording using two-photon-induced photopolymerization. *Appl. Phys. A: Mater. Sci. Process.* 69(4):461–464, 1999.

[98] Saulius Juodkazis, Vygantas Mizeikis, et al. Two-photon lithography of nanorods in SU-8 photoresist. *Nanotechnology* 16(6):846, 2005.

[99] Mangirdas Malinauskas, Paulius Danilevičius, and Saulius Juodkazis. Three-dimensional micro-/nano-structuring via direct write polymerization with pico-second laser pulses. *Opt. Express* 19(6):5602–5610, Mar 2011.

[100] Joachim Fischer, Jonathan B. Mueller, et al. Three-dimensional multi-photon direct laser writing with variable repetition rate. *Opt. Express* 21(22):26244–26260, Nov 2013.

[101] Michael Thiel, Joachim Fischer, et al. Direct laser writing of three-dimensional submicron structures using a continuous-wave laser at 532 nm. *Appl. Phys. Lett.* 97(22):221102–221102–3, Nov 2010.

[102] Cheol-Ki Min, Do-Hyung Kim, et al. Micro holographic recording characteristic with defocused micrograting. *IEEE Trans. Magn.* 47(3):581–584, 2011.

ACKNOWLEDGEMENT

Writing this thesis would have been impossible without perseverance and support by a few people. First of all I am most grateful to my supervisor Prof. Dr. Heinz-Wilhelm Hübers for his patient guidance and invaluable support which guided me through the most strenuous times of these five years.

I would also like to thank Prof. Dr. Pál Koppa for being a member of the defence committee, and Prof. Dr. M. Dähne for chairing the defence.

Further I would like to thank my previous advisor, Prof. Dr. Susanna Orlic for the opportunity to work on microholographic data storage, which has indeed interested me since when I attended her lectures during my graduate studies.

I also wish to thank my colleagues at the Institute of Optics and Atomic Physics of TU Berlin, in particular the former group Optical Technologies for continuous support and fruitful discussions. In particular, my thanks go to Sven Frohmann and Enrico Dietz for their valuable assistance during my research and feedback while I was writing up my manuscript. I am very thankful for our numerous insightful discussions.

The majority of this research was supported by a fellowship of the Helmholtz Research School on Security Technologies organized by TU Berlin and DLR. Membership in this research group, which was launched in 2011, gave me the opportunity to participate in discussions about a wide variety of scientific projects and to experience the highly interdisciplinary spirit. I greatly benefit from having taken part in the training courses at different places and lectures organized by the HRS and Helmholtz Association.

Besides I am grateful for the unreserved support of my parents during my academic studies. Last but not least, I am thankful to my former fellow student, colleague and friend Tina for encouragement, proofreading of my first paper and our enjoyable breaks from work during the stressful times of writing this thesis.